PART III.

INTER-DEPARTMENTAL RESEARCH ACTIVITIES – SELECTED HIGHLIGHTS

Ductile Mg Alloys by Combining *ab initio* and Experimental Methods

S. Sandlöbes [1, 3], M. Friák [2,4], Z. Pei [2], L. Zhu [2], S. Zaefferer [1], J. Neugebauer [2], D. Raabe [1]

[1] Department of Microstructure Physics and Alloy Design (MA)
[2] Department of Computational Materials Design (CM)
[3] now at: RWTH Aachen University
[4] now at: Institute of Physics of Materials, Academy of Sciences of the Czech Republic, Brno, Czech Republic

Magnesium based alloys are attractive for structural applications owing to their low mass density, good castability and efficient recyclability [1, 2]. However, wider application of sheet Mg is hindered by its poor room temperature formability, which is caused by pronounced basal slip and a strong basal-type texture [1, 2]. According to this, the von Mises' criterion for five independent deformation modes to satisfy an arbitrary shape change cannot be met. In hcp crystals strain along the crystal c-axis can only be accommodated by the activation of non-basal slip and deformation twinning, fulfilling the von Mises' criterion requires the activation of non-basal dislocation slip. We showed that single-phase solid-solution Mg-Y alloys exhibit an increased room-temperature ductility by about 5 times, while maintaining a comparable strength and a well-balanced work hardening [1].

We showed by joint transmission electron microscopy (TEM) measurements and *ab initio* calculations that the ductility increase in Mg-Y alloys is caused by an increased activity of <c+a> dislocation slip [2]. This facilitated activation of out-of-basal-plane shear modes through the addition of Y to Mg is correlated to a significantly decreased I_1 intrinsic stacking fault energy (I_1 SFE) [2]. Here, the I_1 SFE is decreasing with increasing Y concentration. We propose that this reduction of the I_1 SFE can be used as a guiding parameter (among others) connected with the ductility increase in the Mg-Y system acting as follows: The enhanced ductility is caused by a high activity of pyramidal <c+a> dislocations as slip modes out of the basal plane. The nucleation of <c+a> dislocations is the critical step in providing out-of-basal-plane shear. This is associated with the SFI_1: the sessile SFI_1, whose energy decreases with Y alloying, is bound by a pyramidal partial dislocation. This dislocation arrangement enables the formation of dislocation structures on pyramidal planes. In line with the nucleation source configuration studied by Yoo et al. [3] we suggest that the SFI_1 acts as heterogeneous nucleation source for pyramidal <c+a> dislocations. Consequently, the observed (TEM) and calculated (*ab initio*) reduced I_1 SFE through the addition of Y could cause the formation of stable SFI_1 in Mg-Y alloys and hence, provide sources for <c+a> dislocations. The reduced SFE leads then to a higher probability of formation of SFI_1 nucleation sources and therefore higher ductility.

We now used the I_1 SFE of Mg-X solid solutions more systematically as a guiding parameter for the design of a general class of ductile Mg alloys (Fig.1). Based on *ab initio* predictions of these I_1 SFE, promising alloys, i.e. those characterized by a reduced I_1 SFE, were produced, homogenized, rolled, mechanically tested and characterized regarding their microstructure, deformation mechanisms and I_1 intrinsic stacking fault energy and we experimentally confirmed that alloys with theoretically predicted decreased I_1 SFE indeed possess significantly enhanced room temperature ductility and experimentally observed increased <c+a> dislocation slip and decreased I_1 intrinsic stacking fault energies [4] (Fig. 2).

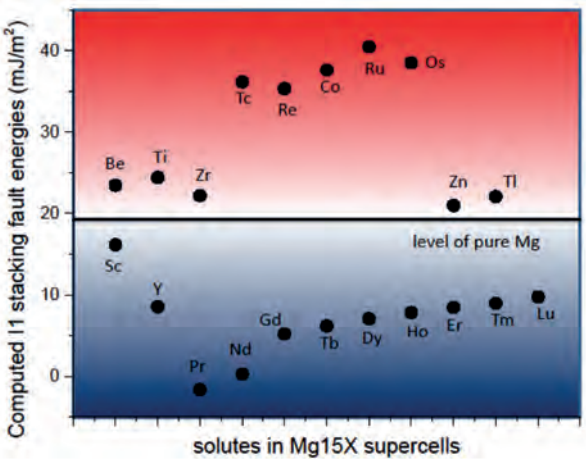

Fig. 1: *Ab initio predicted values of I_1 SFE in binary Mg-X alloys.*

To allow a fast solute assessment without lengthy explicit *ab initio* calculations, we analyzed the correlations and anti-correlation between the I_1 stacking fault energy and intrinsic materials parameters. Our analysis reveals that the atomic volume of pure solutes, their electronegativity and bulk modulus are related to the I_1 SFE. To compare the impact of solutes on the I_1 SFE with that of yttrium we introduced a numerical quantity, the 'Yttrium Similarity Index' which is based on these interrelations and gives the change of the I_1 SFE in Mg alloys with respect to Mg-Y [5]. When considering only binary Mg alloys, we hardly found any alternative solutes providing similar I_1 SFE reduction as that due to rare-earth (RE) additions. Therefore, we extended the 'Yttrium Similarity Index' to ternary Mg

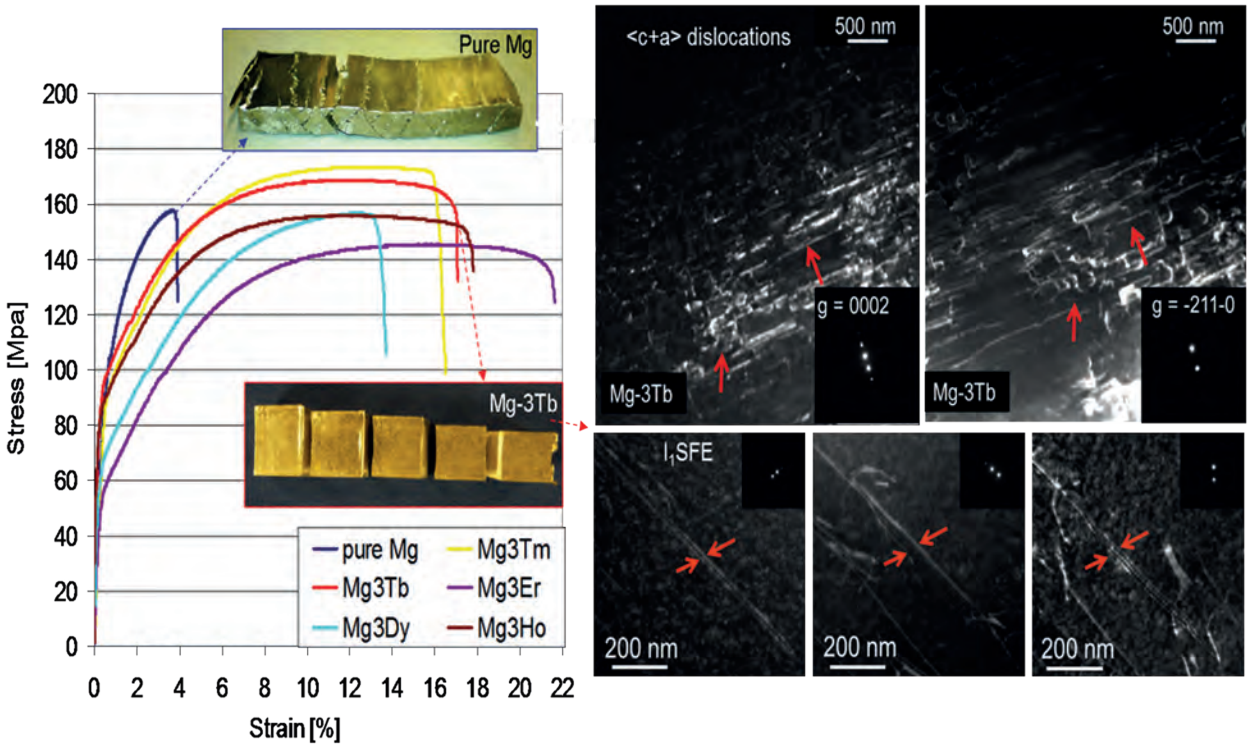

Fig. 2: *Tensile stress-strain (eng. strain) of the newly designed Mg alloys in as-homogenized conditions in comparison to pure Mg. The optical photographs show the alloys after cold rolling to different thickness reductions. The dark-field TEM micrographs show increased activity of <c+a> dislocations (upper micrographs) and reduced I_1 SFE in the new alloys.*

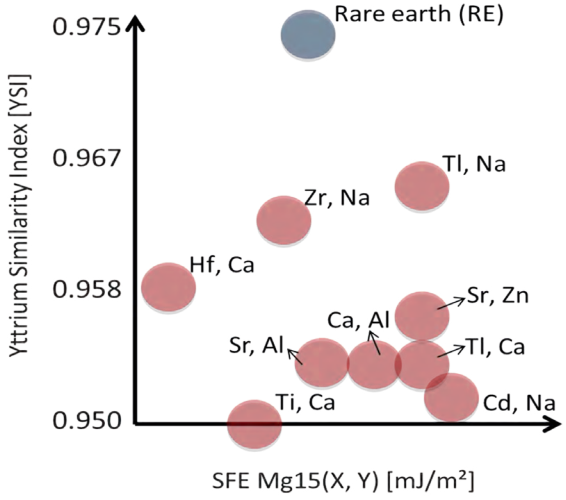

Fig. 3: *Yttrium Similarity Index (YSI) and ab initio calculated stacking fault energy (SFE) for $Mg_{15}(X, Y)$ (X, Y – alloying elements) of promising ternary alloys; for comparison the YSI and SFE for rare earth elements are also shown.*

alloys (Fig. 3). Quantum-mechanical calculations have been subsequently performed for 11 solute pairs with YSIs higher than 0.95 and they were all found to reduce I_1SFE in excellent agreement with the prediction based on the 'Yttrium Similarity Index' [5]. Our future alloy design strategy is based on the synthesis and characterization of these new ternary *ab initio* guided alloys.

References

1. Sandlöbes, S., Zaefferer, S., Schestakow, I., Yi, S., Gonzales-Martinez, R.: Acta Mater (2011) 59, 429.
2. Sandlöbes, S., Friak, M., Dick, A., Zaefferer, S., Yi, S., Letzig, D., Pei, Z., Zhu, L.-F., Neugebauer, J., Raabe, D.: Acta Mater (2012) 60, 3011.
3. Yoo, M.H., Agnew, S.R., Morris, J.R., Ho, K.M.: Mater Sci Eng (2001) A 310-321, 87.
4. Sandlöbes S., Pei Z., Friak M., Zhu L.F., Wang F., Zaefferer S., Raabe D., Neugebauer J.: Acta Mater (2014) 70, 92.
5. Pei Z., Friak M., Sandlöbes S., Nazarov R., Svendsen B., Raabe D., Neugebauer J.: New J Phys 17 (2015) 093009.

Design of Strong and Tough Metallic Glasses: Beyond Poisson's Ratio

M. Köhler [1], B. N. Jaya [2], V. Schnabel [3], C. Kirchlechner [2], D. Music [3], G. Dehm [2], D. Raabe [1], J. M. Schneider [3]

[1] Department of Microstructure Physics and Alloy Design (MA)
[2] Department of Structure and Nano-/Micromechanics of Materials (SN)
[3] RWTH Aachen University, Lehrstuhl für Werkstoffchemie, Materials Chemistry

Metallic glasses (MGs) are becoming increasingly attractive due to their outstanding mechanical and soft-magnetic properties. Co-based MGs, e.g., exhibit a fracture strength above 5 GPa and an elastic modulus of more than 260 GPa [1]. Hence, these materials attract high interest.

Although MGs have been studied for the last decades, they have been mostly developed by using empirical glass-forming rules [1], suggesting a critical Poisson's ratio above which all metallic glasses exhibit pronounced toughness [2, 3]. However, several exceptions to this rule were recently observed [4, 5].

Reaching beyond this approach we established a fundamental criterion, based on chemical bonding, to design fracture resistant MGs. Through correlative *ab-initio* molecular dynamics (MD) simulations based on density functional theory and micro-scale fracture testing, conducted *in-situ* in a scanning electron microscope on magnetron sputtered metallic glass thin films, we are now able to explain the deviations from the concept of Poisson's ratio using ν to predict the brittle-ductile transition in MGs [3]. For that purpose we have simulated, synthesized and tested 5 different compositions (2 binary, 1 ternary, 2 multi-component MGs).

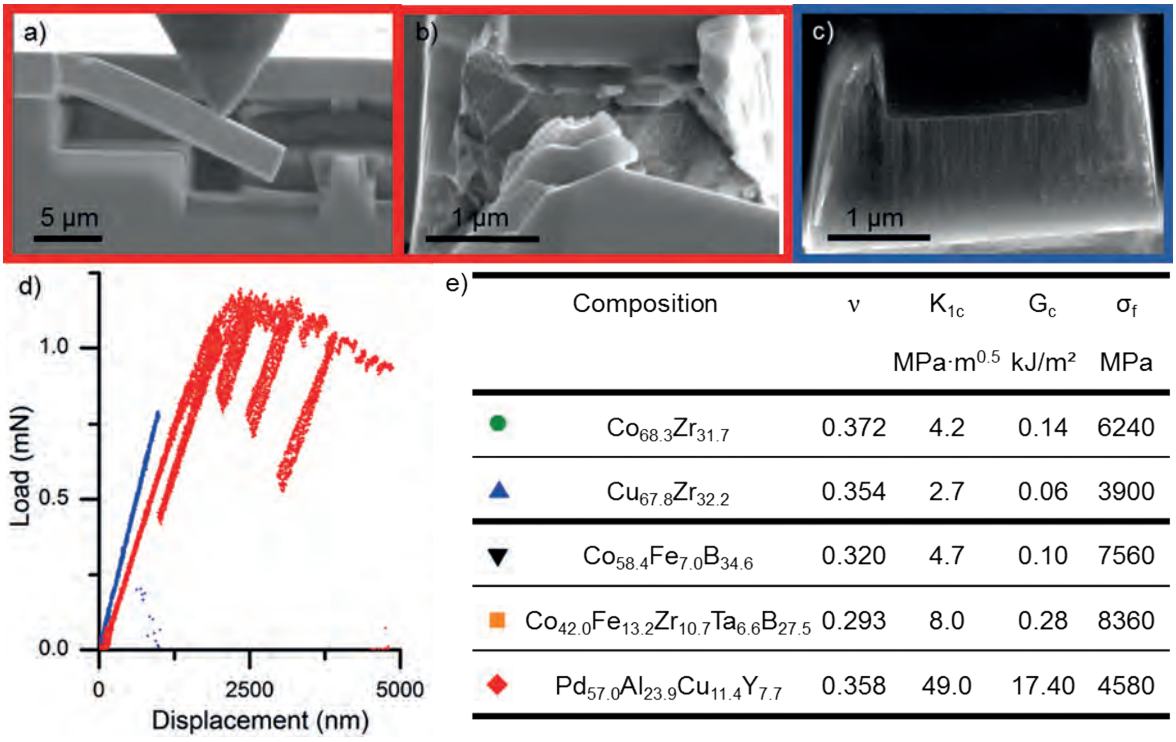

e)

Composition	ν	K_{1c} MPa·m$^{0.5}$	G_c kJ/m²	σ_f MPa
● $Co_{68.3}Zr_{31.7}$	0.372	4.2	0.14	6240
▲ $Cu_{67.8}Zr_{32.2}$	0.354	2.7	0.06	3900
▼ $Co_{58.4}Fe_{7.0}B_{34.6}$	0.320	4.7	0.10	7560
■ $Co_{42.0}Fe_{13.2}Zr_{10.7}Ta_{6.6}B_{27.5}$	0.293	8.0	0.28	8360
◆ $Pd_{57.0}Al_{23.9}Cu_{11.4}Y_{7.7}$	0.358	49.0	17.40	4580

Fig. 1: *[6] In-situ micro-cantilever fracture experiments. The fracture strength and toughness of the metallic glass thin films are measured by employing both un-notched and pre-notched specimens. a) Representative scanning electron image of an in situ micro-cantilever deflection experiment performed on a $Pd_{57.0}Al_{23.9}Cu_{11.4}Y_{7.7}$ glass. b) and c) show high magnification images of the crack trajectory and fracture surface of the tough $Pd_{57.0}Al_{23.9}Cu_{11.4}Y_{7.7}$ and the brittle $Cu_{67.8}Zr_{32.2}$ metallic glass, respectively. d) Load-displacement graphs for the brittle $Cu_{67.8}Zr_{32.2}$ in blue and the tough $Pd_{57.0}Al_{23.9}Cu_{11.4}Y_{7.7}$ in red. The dissipated energy before fracture (area under the curve) for the highly damage tolerant $Pd_{57.0}Al_{23.9}Cu_{11.4}Y_{7.7}$ glass is much higher compared to the brittle $Cu_{67.8}Zr_{32.2}$ glass. e) Summary of the ab initio calculated Poisson's ratio (ν), and the measured quantities fracture toughness (K_{1c}), fracture energy (G_c) and fracture strength (σ_f) of the glasses studied within this work. Fig.1 summarizes these results for the five glass compositions tested. Further microstructural characterization has been undertaken, including transmission electron microscopy and atom probe tomography (APT) to establish the homogeneity and confirm the amorphous nature of these samples. The combination of theoretical (ab initio MD) and experimental (mechanical and microstructural characterization) reveal that the fraction of bonds stemming from deep core, hybridized states compared to the overall bonding defines damage tolerance in glasses.*

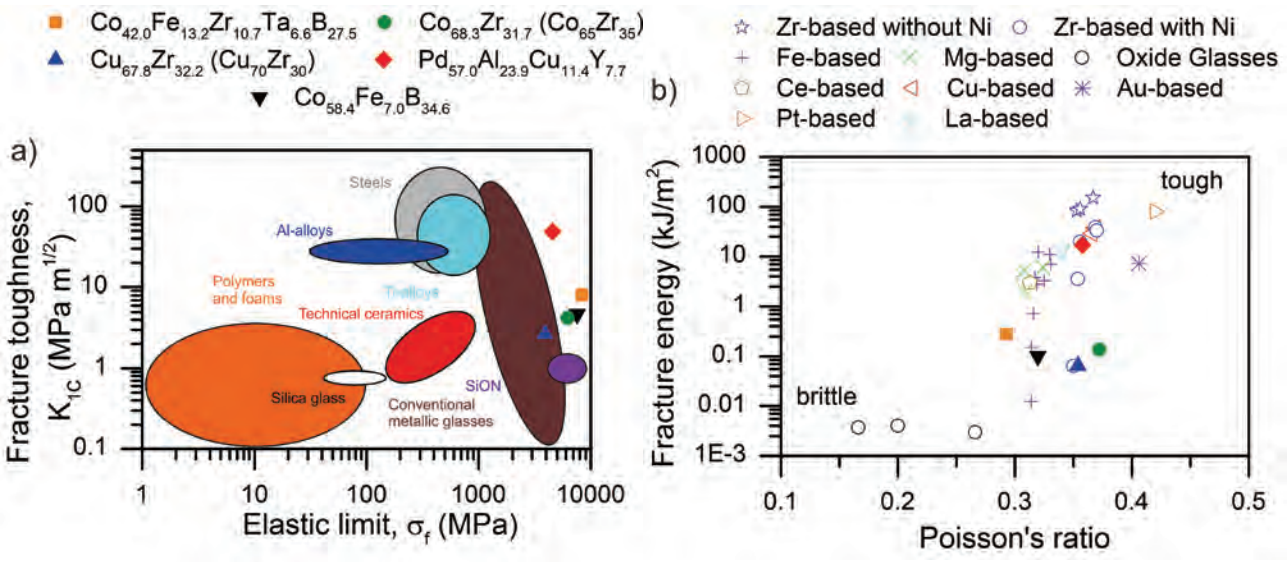

Fig. 2: *[6] Experimental validation reveals extraordinary damage tolerance for the metallic glasses studied in this work. a) The fracture strength of the glasses studied in this work is close to the ideal strength of the material. The $Pd_{57.0}Al_{23.9}Cu_{11.4}Y_{7.7}$ thin film metallic glass is identified to exhibit high damage tolerance. b) Poisson's ratio cannot gauge the chemical origin of the rapid evolution from brittle to tough behaviour. Literature data for the Mg-based, Ce-based and La-based [7, 8], Fe-based [9], oxide glasses [2, 10], Zr-based [4, 11], Cu-based [12, 13], Pt-based [14] and Au-based [7] glasses are presented. Fig. 2 compares the mechanical behaviour of the glasses that we developed with other known metallic glasses in an Ashby-type map. By investigating the bonding states of the different MGs via electronic density-of-states analysis we reveal the different bonding behaviour. The tough Pd-based glass e.g. shows low hybridization (Pd-Al) in contrast to the brittle CuZr glass which shows a strong hybridization while having a similar poisson's ratio. Therefore, bond hybridization is identified as a suited indictor for damage tolerance of MGs. Our approach allows for searching novel damage tolerant glasses by screening the electronic structure of yet new chemical compositions.*

References

1. Inoue, A. et al.: Acta Materialia (2014) 52(6).
2. Lewandowski, J.J., et al.: Philosophical Magazine Letters (2015) 85(2).
3. Greaves, G.N. et al.: Nat Mater (2011) 10(11).
4. He, Q. et al.: Acta Materialia (2011) 59(1).
5. Kumar, G. et al.: Scripta Mater. 652011.
6. Schnabel, V. et al.: manuscript *in preparation* (2015).
7. Madge, S.V. et al.: Acta Mater 602012.
8. Xi, X.K. et al.: Phys Rev Lett (2005) 94(12).
9. Lewandowski, J.J. et al.: Appl Phys Lett 922008.
10. Mecholsky, J.J. et al.: Journal of the American Ceramic Society (1974), 57(10).
11. Raghavan, R. et al.: Acta Mater 572009.
12. Wesseling, P. et al.: Scripta Materialia (2004) 51(2) .
13. Jia, P. et al.: Scripta Materialia (2009) 61(2).
14. Schroers, J. et al.: Phys Rev Lett 932004.

Initial Wear: Engineering down to the Atomic Scale

Z. Peng [1], P. Choi [1], M. Rohwerder [2], A. Vogel [2], D. Raabe [1]
F. Bernhardt [3], M. Friedrichs [3], O. Dambon [3], F. Klocke [3]

[1]Department of Microstructure Physics and Alloy Design (MA)
[2]Department of Interface Chemistry and Surface Engineering (GO)
[3]Fraunhofer-Institut für Produktionstechnologie IPT

With the quickly growing demand for high quality optical lenses glass molding (PGM) is a pivotal manufacturing method. This modern technology enables effective, replicative and large-scale fabrication of complex shape optics such as aspherical or diffractive lenses and lens arrays (Fig. 1) without any grinding and polishing steps.

As shown in Fig. 1, during the PGM process, glass blanks are placed in the mold of a pressing tool and are heated under vacuum or N_2 protective atmosphere up to the glass forming temperature, which normally ranges from 400 to 700°C. Subsequently, high press forces (2-20kN) are applied for several minutes until the mold form is homogeneously filled with glass. After controlled cooling, the final products can be detached from the mold. Since the molds experience not only thermo-mechanical stresses but are also subjected to a severe thermochemical environment, detrimental oxidation and corrosion processes finally lead to severe problems such as glass sticking. This phenomenon usually occurs after numerous cycles, limiting the lifetime of the molds, and is a decisive factor for economical industrial production of high-precision glass molds [1, 2].

The aims of the project Initial Wear are to investigate the fundamental mold degradation mechanisms, in particular in their initial stages. Degradation is studied using (sub-) nanometer scale characterization methods to propose a model, based on which the service lifetime of the molds can be predicted and even prolonged.

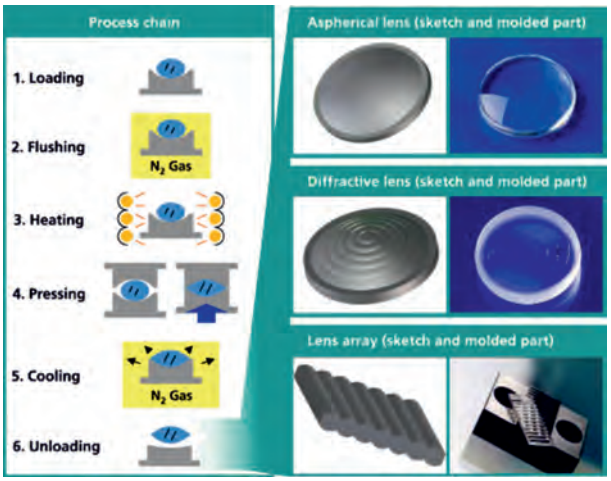

Fig. 1: *Outline of the precision glass molding process and the pictures of the representative products (image taken from IPT).*

In this research, the studied mold material is ultrafine grained (average grain size is around 200 nm) WC/Co hard mental with a sputter-deposited $Pt_{0.3}Ir_{0.7}$ coating, which is reported to be one of a most promising material system for PGM application [3]. High

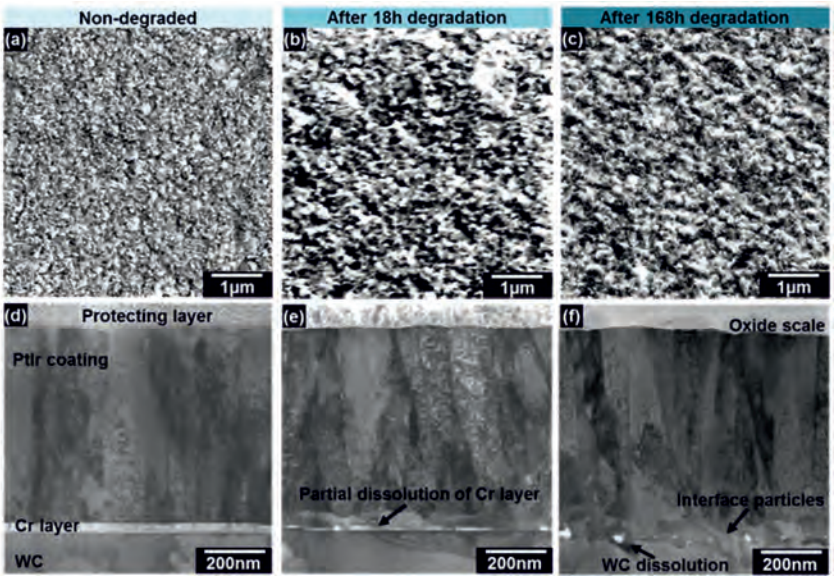

Fig. 2: *SEM images taken from the specimen surface (a-c) and TEM images taken from the specimens' cross section (d-e). (a) and (d) for the non-degraded specimen, (b) and (e) for the 18 h degraded specimen and (c) and (f) for the 168 h degraded specimen.*

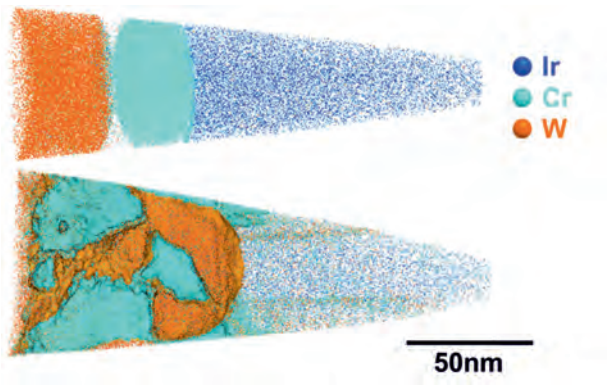

Fig. 3: APT elemental maps for the non-degraded specimen (upper) and the 168 h degraded specimen (lower).

adhesive strength between the top coating, which mainly serves to avoid sticking of glass to the hard metal, and the hard metal is necessary to avoid coating delamination, therefore an adhesive Cr interlayer is normally deposited [4].

Four main parameters influence the mold degradation processes, namely: atmosphere, temperature, mechanical stress and glass composition. The effects of atmosphere and elevated temperature are investigated because these two factors are common to all the PGM production techniques and seem to be the main factors controlling mold degradation. Therefore, specimens were firstly degraded for different exposure times under a well-controlled condition (temperature: 630°C, atmosphere: N_2/2.5%H_2 gas mixture with oxygen partial pressure of $1.23*10^{-23}$ bar), where the conditions are typical of real PGM processes. After degradation, different methods were used to characterize the specimens. Scanning electron microscopy (SEM) was applied to examine the surface morphology and damages; transmission electron microscopy (TEM) was employed to reveal the specimen microstructure and atom probe tomography (APT), which is a powerful tool for the characterization of thin-film materials [5, 6, 7] as well as nanometer-thick oxide scales [8], was utilized to acquire the 3D chemical compositions of different regions of the specimens with near-atomic resolution.

Fig. 2 shows SEM images of the specimen surface and TEM images of the specimen cross section. After 18 h degradation, the Cr adhesive layer is mostly intact but already partially dissolved. Moreover, after 168 h degradation, the original Cr layer is replaced by a chain of nanometer-sized particles and localized dissolution of WC hard metal results in a rough interface. Besides, an oxide scale of about 100 nm in thickness can be found, which leads to the change of the surface topology.

APT results are shown in Fig. 3 and Fig. 4. Interdiffusion between the PtIr coating, Cr adhesive layer and WC substrate can be observed, which assist the formation of the Cr rich (26at.% Cr, 55at.% Ir and 19at.% Pt) and W rich (25at.% W, 60at.% Ir and 15at.% Pt) interface particles. At the same time W atoms and Cr atoms diffuse upward along the grain boundaries and triple junctions of the PtIr coating to its surface where they are subsequently oxidized. However, no oxidation was observed in the bulk, raising questions about how exactly the WC is degraded.

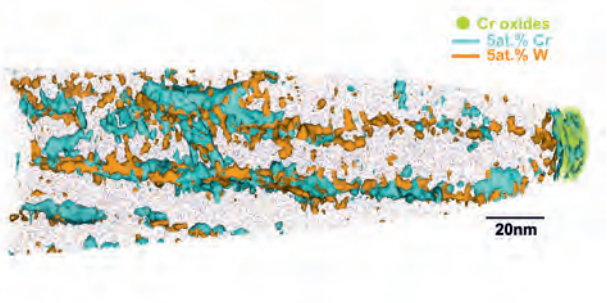

Fig. 4: *APT elemental map of the 168 h oxidized specimen.*

The experimental results achieved up to now clearly reveal degradation induced by atmosphere and elevated temperature. Further studies will focus on the effects of mechanical and chemical loads on surface degradation mechanisms.

References

1. F. Klocke et. al.: Opt Eng (2012) 51, 073401.
2. F. Bernhardt et. al.: Proc SPIE (2013) 88841V.
3. F. Klocke et. al.:, 7th Int Conf “The” Coatings Manuf. Eng (2008) 1-3.
4. F. Klocke et. al.: Surf Coatings Technol (2011) 206, 1867.
5. P. Choi et al.: Ultramicroscopy (2011) 111, 518.
6. I. Povstugar et al.: Acta Mater (2013) 61, 7534.
7. D. Tytko et al.: Acta Mater (2015) 85, 32.
8. J. H. Kim et al.: Corrosion Science (2015) 96, 52.

Towards Atomistically-Guided High Entropy Alloy Design

C.C. Tasan [1], D. Ma [1], K.G. Pradeep [1], Z. Li, Y. Deng [1], H.Springer [1], D. Raabe [1], B. Grabowski [2], F. Körmann [2], J. Neugebauer [2]

[1]Department of Microstructure Physics and Alloy Design (MA)
[2]Department of Computational Materials Design (CM)

In the past decade, the high entropy alloy (HEA) concept has attracted extensive research attention. This new alloy design strategy aims at the maximization of the entropy of mixing with the purpose of producing massive solid solution, single phase microstructures. The heavy lattice distortion and the thereby introduced sluggish diffusion are proposed to jointly contribute to high thermal stability and excellent mechanical properties. However, among various HEAs that have been designed according to this concept, most show brittle, multi-phase microstructures, and thus fail to prove the principle of the original concept described above. These unsuccessful design efforts raise concerns about the future applicability of HEAs. At the MPIE, various research projects have been initiated in the Adaptive Structural Materials group on this newly emerging field, taking off from the only alloy system that develops a single fcc solid solution upon conventional casting: the FeMnNiCoCr system. The main focus is on: (i) replacing currently adopted phenomenological criteria with physically-based alloy design guidelines based on density-functional-theory (DFT) *ab initio* simulations; (ii) designing novel, high performance HEAs that have the potential to replace alloys currently in service. Here a key focus is to revert to non-equiatomic alloy compositions to greatly expand the compositional ranges in search for potential future alloys (Fig. 1) [1].

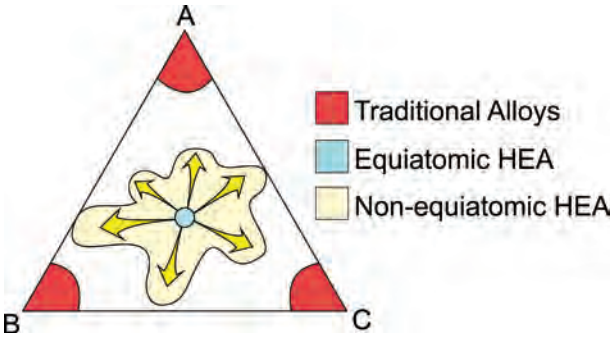

Fig. 1: *A schematic comparison of traditional alloys with one base element and minor alloying additions, high entropy alloys with equiatomic compositions of all alloying elements, and non-equiatomic - yet still massively alloyed - high entropy alloys, on the isothermal cross section of a ternary phase diagram [1].*

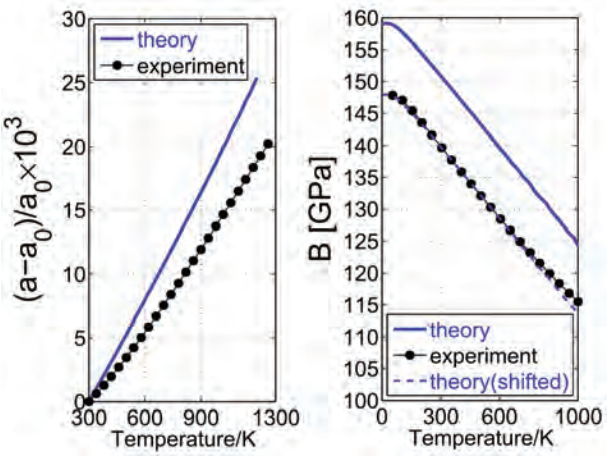

Fig. 2: *Calculated (solid blue lines)* ***(a)*** *thermal expansion and* ***(b)*** *isothermal bulk modulus as a function of temperature compared to experiment (black solid circles). The calculated thermal expansion and bulk modulus correspond to the fcc DLM phase and include all free energy contributions, i.e., electronic, vibrational, and magnetic. The dashed blue line in (b) is obtained by a constant shift of the calculated bulk modulus (blue solid line) to match the experimental bulk modulus extrapo*lated to T = 0 K. Figure taken from [2] with permission.

The description of entropic contributions from *ab initio* for multi-component magnetic alloys, such as e.g., FeMnNiCoCr, is a challenging task especially regarding finite temperature descriptions and increasing computational costs of supercell calculations. To cope with these challenges we have implemented and extended an integrated approach that is based on the exact-muffin-tin-orbitals approach to DFT in conjunction with the Debye model (for the vibrational degrees-of-freedom), the coherent potential approximation (for chemical disorder), the disordered local moment approach (for spin disorder) , and with a mean field approximation (for magnetic excitations). We have utilized this integrated *ab initio* approach to investigate in detail the phase stabilities of the hcp, fcc, and bcc phases in various magnetic states in the FeMnNiCoCr HEA [2]. The strength of the approach is demonstrated in Fig. 2 where we compare the computed thermal expansion and the bulk modulus (blue lines) of the thermodynamically most stable

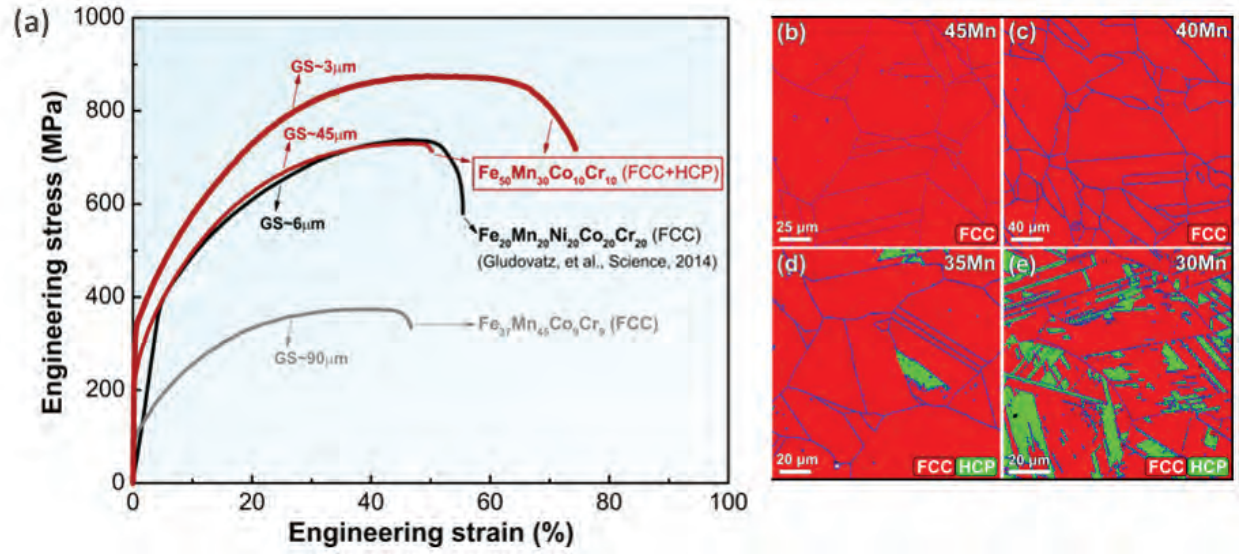

Fig. 3: (a) *Comparison of the mechanical behaviour of the TRIP-HEA and two single phase HEAs;* **(b-e)** *EBSD phase maps of* $Fe_{80-x}Mn_xCo_{10}Cr_{10}$ *(x = 45, 40, 35 and 30) HEAs demonstrating the increase in hcp% with decreasing Mn.*

phase, paramagnetic fcc, with experimental data (black dots). The developed toolbox enables confident investigations of quantities that are not easily accessible by experiment. We, e.g., recently demonstrated that entropy contributions other than the configurational one (vibrational, electronic, magnetic) are not negligible as previously assumed [2]. Furthermore, having these results available for the different phases (e.g. fcc and hcp), allows us to calculate the stacking fault energy (SFE) (using the ANNNI model) which is a critical quantity for plasticity and thus an important input to our experimental efforts.

Having access to theoretically determined SFE's as a function of composition, especially in such complicated alloy systems, is a strong support to our metallurgical alloy design process. In fact, our current experimental efforts clearly demonstrate that by optimizing SFE, properties much superior to presently proposed HEAs can be achieved. Fig. 3a shows one such clear example. The transformation induced plasticity (TRIP)-HEA $Fe_{50}Mn_{30}Co_{10}Cr_{10}$ developed in our group outperforms the equiatomic FeMnNiCoCr alloy in quasi-static tension test at room temperature. Similarly, we have observed that twinning induced plasticity (TWIP)-HEA $Fe_{40}Mn_{40}Co_{10}Cr_{10}$ has comparable mechanical properties to the FeMnNiCoCr alloy, despite the decreased alloying [4]. The accompanying microstructure characterization (Fig. 3b-e) reveals the critical role of Mn here in this four-component system, in both controlling the fraction of thermally-induced hcp martensite, and also the transition from dislocation plasticity to mechanically induced twinning and/or martensitic transformation assisted plasticity.

References

1. K.G. Pradeep, C.C. Tasan, M.J. Yao et al.: Mat Sci Eng A (2014) 81, 386-400.
2. D. Ma, B. Grabowski et al.: Acta Mat (2015) 100, 90–97.
3. Laplanche et al.: J. Alloy. Compd (2015) 623 348; Intermetallics 58 (2015) 62.
4. Y. Deng, C.C. Tasan, K.G. Pradeep et al.: Acta Mat (2015) 94, 124-133.

Atomistic Understanding of the Off-Stoichiometry of κ-Carbides in Density Reduced Steels

M.J. Yao [1], P. Dey [2], P. Choi [1,3], M. Herbig [1], T. Hickel [2], M. Hafez-Haghighat [1], J. Seol [1,4], I. Gutierrez-Urrutia [1,5], R. Marceau [1,6], S. Sandlöbes [1,7], E. Welsch [1], H. Springer [1], J. Neugebauer [2], D. Raabe [1]

[1] Department of Microstructure Physics and Alloy Design (MA)
[2] Department of Computational Materials (CM)
[3] now at: Korea Advanced Institute of Science and Technology (KAIST), South Korea
[4] now at: National Institute for Nanomaterial Technology, POSTECH, South Korea
[5] now at: National Institute for Materials Science (NIMS), Japan
[6] now at: Deakin University, Institute for Frontier Materials, Australia
[7] now at: Institute for Physical Metallurgy and Metal Physics (IMM), Rheinisch-Westfälische Technische Hochschule Aachen (RWTH)

Fe-Mn-Al-C steels show excellent combination of strength, formability and low density rendering these materials attractive for light-weight vehicle applications [1-5]. The precipitation of nano-sized κ-carbides significantly strengthens these steels while preserving good ductility, owing to their excellent strain hardening [2, 3]. Though deformation mechanisms like glide plane softening, shear-band-induced plasticity (SIP) and microband-induced plasticity (MBIP) have been proposed [1, 4, 5], the interaction between dislocations and κ-carbides are still not well understood. The stress contribution from shearing of ordered particles is closely related to the antiphase boundary energy (APB) along the slip plane [6] and thereby to the stoichiometry and site-occupancy of the κ-carbides. Although it is known that κ-carbides tend to have off-stoichiometric composition, this matter has, owing to experimental challenges, hardly been experimentally quantified. Therefore, there is a lack of reliability of thermodynamic databases and a lack of understanding of the reasons for the off-stoichiometry. Here, we employ atom probe tomography (APT) to accurately determine chemical compositions and subsequently density functional theory (DFT) to predict the corresponding elemental site-occupancy in κ-carbides.

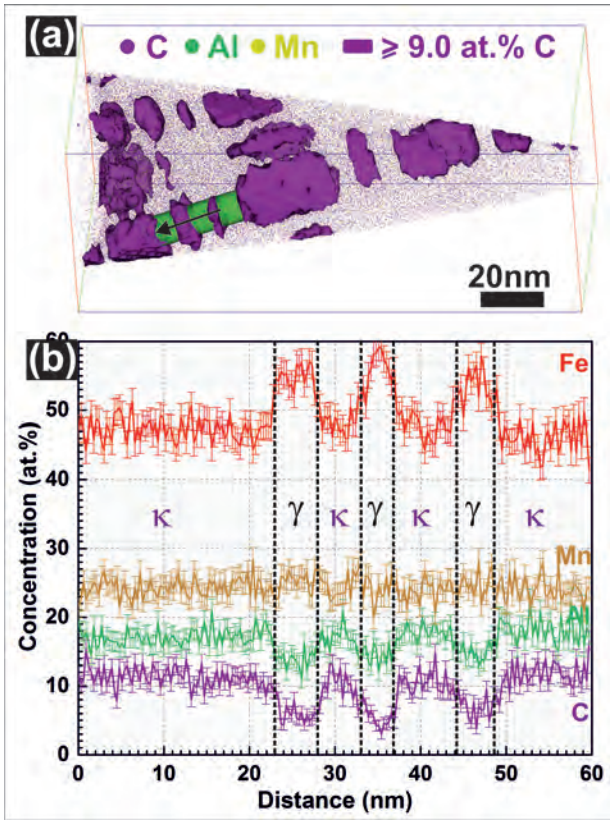

Fig. 1: *(a) 3D APT map showing κ-carbides, which are visualized by a 9 at.% C iso-concentration surface. (b) Elemental partitioning between κ-precipitates and γ-matrix along the cylindrical region of interest highlighted in green in (a).*

An austenitic Fe-29.8Mn-7.7Al-1.3C (wt%) steel is aged at 600°C for 24 hours to cause precipitation of coherent κ-carbides. Using a local electrode atom probe (LEAP) 3000X HR, the three-dimensional (3D) morphology of the nano-sized κ-carbides is revealed (Fig.1a). Cuboidal and plate-like κ-carbides are arranged in the form of stacks along three orthogonal directions which are elastically soft <001> crystallographic directions according to TEM observations [3]. There are two kinds of γ channels in different widths, broad ones of 10 - 40 nm in between particle stacks and narrow ones of 2 - 5 nm within particle stacks. Due to projection effects, particles of cubic shape in common TEM observations might actually have a much smaller size in the third dimension, i.e. plate-like shape. Al and C atoms clearly partition into the κ-carbides from the γ-matrix; no compositional difference is noticed between bigger cuboidal and smaller plate-like ones (Fig.1b). Their average chemical compositions are determined by careful mass spectrum analysis (Table 1). Instead of the ideal $L'1_2$ stoichiometry $(Fe, Mn)_3AlC$, the measured composition of $Fe_{2.0}Mn_{1.1}Al_{0.9}C_{0.6}$ indicates depletion both in interstitial carbon and in substitutional Al, implying the probable presence of C vacancies as well as Al vacancies or antisites on the Al-sublattice.

To understand the experimentally determined off-stoichiometric κ-carbide compositions, DFT calculations are performed which determine the

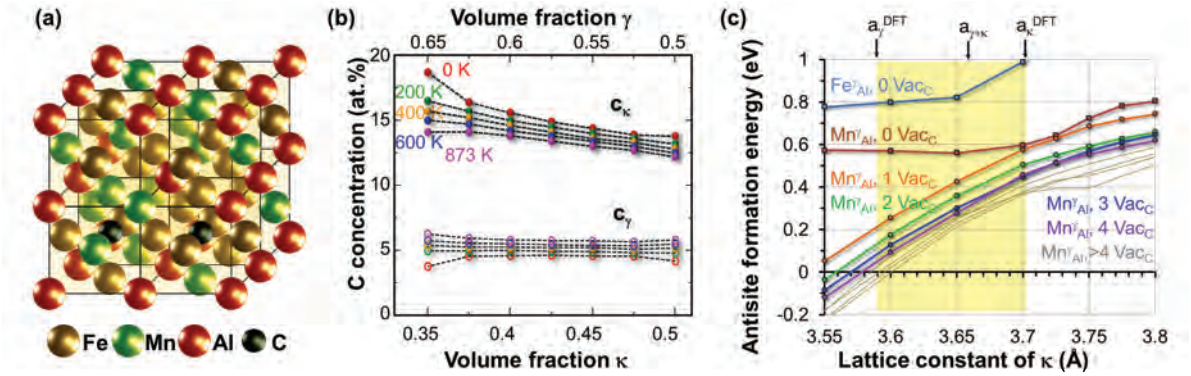

Fig. 2: *(a) 2x2x2 supercell adopted in DFT calculations with the κ-precipitate composition measured by APT - $Fe_{16}Mn_9Al_7C_5$ ($Fe_{2.0}Mn_{1.125}Al_{0.875}C_{0.625}$). (b) Carbon concentrations in κ-carbides and the γ-matrix as a function of their volume fraction at different temperatures including the experimental annealing temperature of 600°C (873K). (c) Mn antisite formation energy as a function of the lattice constant for different numbers of carbon vacancies.*

energetic stability of these different possible defects. Thermodynamic concepts were developed and applied to fully consider the experimental constraints in terms of local composition (Fig.2a). Importantly, there is a remarkable effect of volumetric strain on C vacancy formation energy – the more the κ-carbides are compressed, the more the C vacancies are energetically favored. Thus, the measured depletion of C in κ-carbides is a consequence of compressive coherency stresses exerted by the γ-matrix. As a consequence, we predict a decrease of the C content in κ-carbide with the κ/γ volume fraction, since this ratio determines the elastic misfit energy (Fig.2b). Due to configurational entropy the driving force on C to leave κ-carbide becomes even stronger at finite temperatures, as can be seen in particular for the experimental annealing temperature of 600˚C (873K) in Fig.2b.

However, the sole effect of elastic strain cannot explain the Al off-stoichiometry since the vacancy formation at an Al site is energetically unfavored even under volumetric compression. Further, the Al depletion caused by the formation of Mn^{γ}_{Al} antisites (Mn atoms from the γ matrix replace Al atoms in κ) in an otherwise perfect κ phase arising from this effect is three orders of magnitude lower than the experimentally measured one. However, when combining the effects of strain and C vacancies within DFT calculations a drastic effect on the stabilization of Mn^{γ}_{Al} antisites is observed that is in the right order of magnitude to explain the experimental values (Fig.2c). The preference for the formation of Mn^{γ}_{Al} antisite in the vicinity of C vacancies can be explained by the strong binding energy between Al and C under volumetric constraint. It gives rise to a high retention of Al to the κ-carbide, but the reduction of the carbon concentration makes the presence of Al in the κ-carbide less favored.

Based on the combination of APT and DFT investigations – i.e. the joint effort of two departments – it was, thus, possible to understand the off-stoichiometric composition and corresponding elemental site-occupancy of κ-carbides in an austenitic Fe-Mn-Al-C steel: In such a κ/γ system with coherent κ-carbides embedded in γ-matrix, the alloy tends to minimize the elastic strain energy and stabilize the two-phase microstructure by having C vacancies and Mn^{γ}_{Al} antisites (Fig.2a).

References

1. G. Frommeyer, U. Bruex: Steel Res Int (2006) 77, 627.
2. H. Springer, D. Raabe: Acta Mater (2012), 60, 4950.
3. I. Gutierrez-Urrutia, D. Raabe: Scripta Mater (2013) 68, 343.
4. K.-T. Park: Scripta Mater (2013) 68, 375.
5. D. Raabe, H. Springer, I. Gutierrez-Urrutia, F. Roters, M. Bausch, J.-B. Seol, M. Koyama, P.-P. Choi, K.Tsuzaki: JOM (2014) 66, 1845.
6. A.J. Ardell,J.C. Huang: Philos Mag Lett (1988) 58, 189.

Coarsening Kinetics of Lamellar Microstructures of Fe-Al *in situ* Composites – Experiments and Simulations

X. Li [1], F. Stein [1], F. Bottler [2], R. Spatschek [3], A. Scherf [4], M. Heilmaier [4]

[1] Department of Structure and Nano-/ Micromechanics of Materials (SN)
[2] Department of Microstructure Physics and Alloy Design (MA)
[3] Department of Computational Materials Design (CM)
[4] KIT - Institute for Applied Materials, Karlsruhe

Fe-Al alloys in the composition range of about 55 to 65 at.% Al undergo a rapid eutectoid phase transition at 1095 °C resulting in an *in situ* composite material with a fine-scaled lamellar microstructure with average lamellar spacing λ of about 200 nm in as-cast material [1] (Fig. 1). During this instantaneous solid-state reaction, the high-temperature phase Fe_5Al_8 with a cubic, γ brass-type structure decomposes into a mixture of the crystallographically closely related phase B2 FeAl and the triclinic phase $FeAl_2$ [2,3]. Very similar fine-scaled lamellar microstructures consisting of two intermetallic phases are well-known from Ti-Al-based alloys, where they lead to a combination of well-balanced properties in terms of creep, ductility and strength.

The coarsening behaviour of the fine microstructures was investigated in dependence on time and temperature by detailed experimental work and compared to results of phase field simulations. On the one hand, the knowledge about the coarsening kinetics is of particular importance to explore the potential of such lamellar FeAl + $FeAl_2$ alloys as candidates for high-temperature applications. On the other hand, the extended, nearly perfect lamellar microstructures offer an excellent possibility to study the kinetics of coarsening of lamellar structures in general and compare the observations to existing theoretical models.

An Fe-Al alloy containing 60.9 at.% Al, which corresponds to a fully-lamellar microstructure, was synthesized by induction melting and pieces were heat-treated at 600, 700, 800, and 1000 °C for various times ranging from 10 min up to 5000 h. Heat treatments were performed in an Ar inert atmosphere and all samples were finally quenched to room

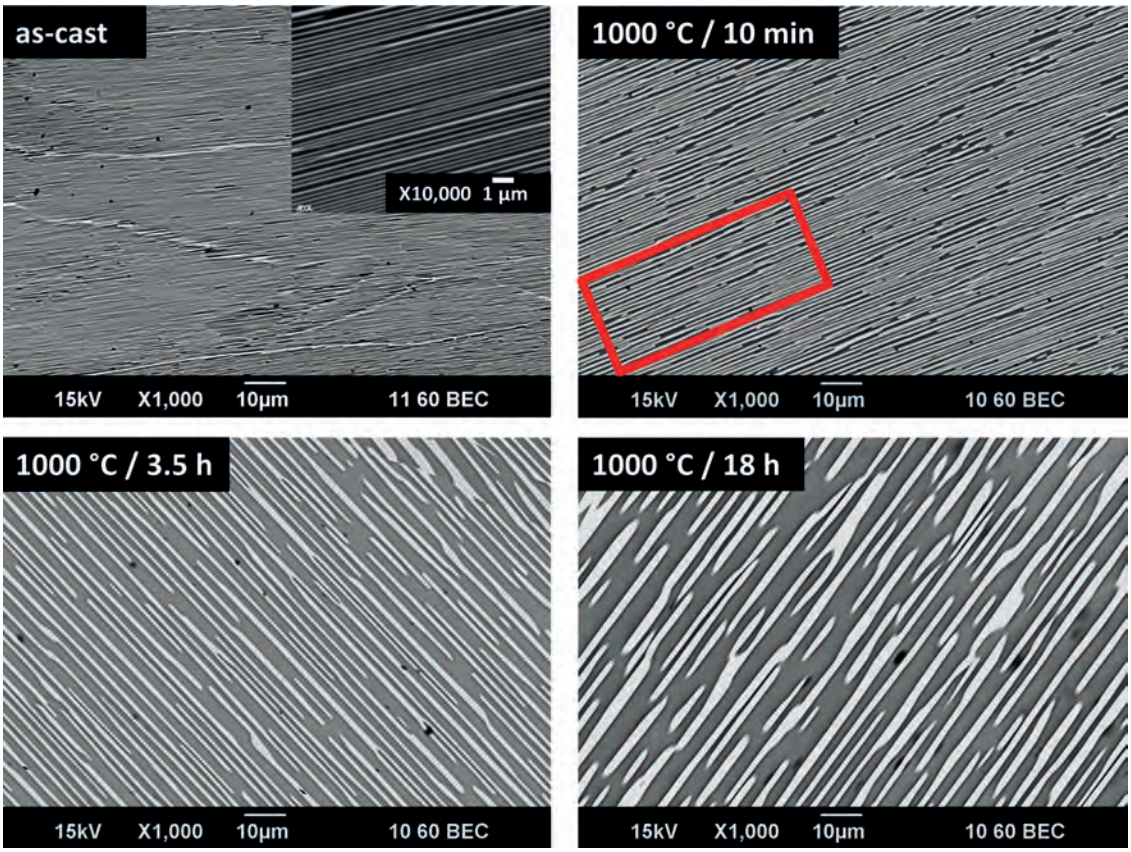

Fig. 1: *Coarsening of the lamellar FeAl + $FeAl_2$ microstructure of an Fe-60.9 at.% Al alloy after different times at 1000 °C (scanning electron microscope pictures obtained in back-scattered electron mode). The red region shows the domain that is used for the phase field simulations as input.*

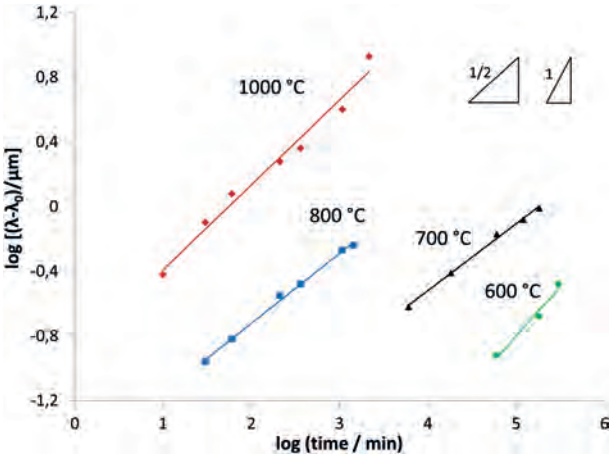

Fig. 2: *Double-logarithmic plot of the increase of the lamellar distance as a function of time.*

temperature. The true lamellar distances were determined by a special procedure taking into account the 3D nature of the microstructure. In a first step, an extended lamellar area on the surface of a sample was oriented with the lamellae extending parallel to the *x* or *y* direction, and in the next step, the surface was vertically cut perpendicular to the lamellae orientation by focused ion beam. To observe the new surface, the sample was tilted and the distance of the lamellae as well as the angle between the lamellae and the edge between original and new surface were measured. From these values and the known tilting angle, the true lamellar distance can be calculated by simple geometrical considerations. In this way, at least ten values were determined per sample. Each data point in Fig. 2, which shows the increase of the lamellar distances as a function of time for different temperatures, corresponds to the average value of such a procedure.

As an example, Fig. 1 shows the development of the microstructure after different heat treatment times at 1000 °C. At this high temperature, coarsening as expected is very quick and after times longer than 36 h, the lamellae have already spheroidized so strongly that it is no longer possible to get a reliable value for the lamellar spacing. At lower temperatures, the coarsening kinetics is very much slower; e.g. after 5000 h holding at 600 °C, the lamellar distances are still smaller than after only 10 min at 1000 °C. As is visible from Fig. 2, the time dependence of the increase of the lamellar distance can be well described by simple power functions with exponents of 0.6(1), 0.41(1), 0.42(1), and 0.51(5) for 600, 700, 800, and 1000 °C, respectively.

Theoretical models for the coarsening of lamellar systems have been developed by Graham and Kraft [4] and Cline [5], which predict different scaling laws for the coarsening. The Graham-Kraft model leads to a scaling of the lamellar spacing according to $\lambda \sim t$, whereas Cline predicts a slower scaling with time t according to $\lambda \sim t^{1/2}$. The present experimental investigations indicate that the Cline model leads to an appropriate description,(Fig. 2).

To further shed light on the different analytical descriptions, we have developed a diffusion-limited alloy phase field model to predict the coarsening kinetics also numerically. The basic ingredient of both above theories [4,5] is the shrinkage kinetics of lamella terminations driven by surface energy minimization. The anticipated scaling of the shrinkage velocity $v \sim 1/\lambda^2$ is verified by the phase field simulations, whereas a Cahn-Hilliard model leads to more sluggish kinetics. This outcome is the basis for two-dimensional phase field simulations with experimental microstructures as initial condition (Fig. 3). The coarsening of the lamellae can clearly be seen, in analogy to the experimental results in Fig. 1.

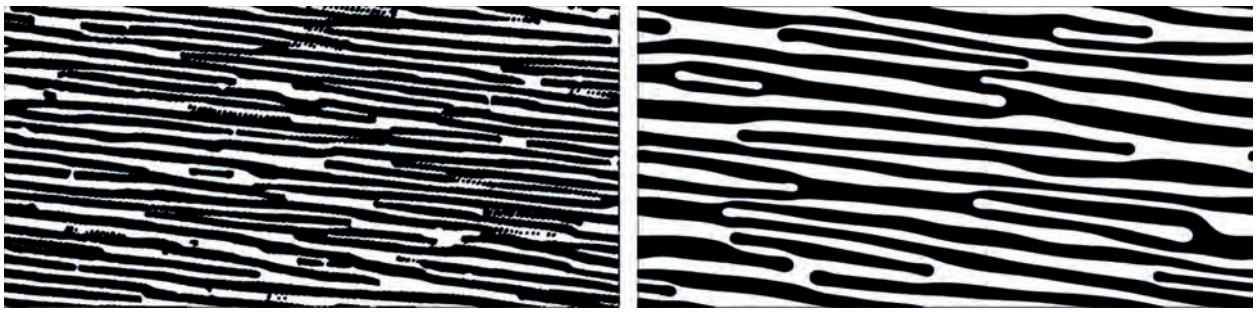

Fig. 3: *Two-dimensional phase field simulation of lamella coarsening, using the red section in Fig. 1 as initial condition (left). The right panel shows a snapshot of the coarsening process.*

References

1. Li, X.; Palm, M.; Scherf, A.; Janda, D.; Heilmaier, M.; Stein, F.: MRS Proc. 1760 (2015) mrsf14-1760-yy1704.
2. Stein, F.; Vogel, S.C.; Eumann, M.; Palm, M.:Intermetallics 18 (2010) 150.
3. Vogel, S.C.; Stein, F.; Palm, M.: Appl.Phys.A 99 (2010) 607.
4. Graham, L.D.; Kraft, R.W.: Trans. Metal. Soc. AIME 236 (1966) 94.
5. Cline, H.E.: Acta Metall. 19 (1971) 481.

Atomic Structure and Properties of Silicon Grain Boundaries

A. Stoffers [1], B. Ziebarth [5,6], J. Barthel [7,8], O. Cojocaru-Mirédin [1], C. Liebscher [2], R. Raghavan [2], B. N. Jaya [2], G. Dehm [2], J. Neugebauer [3], C. Scheu [4], C. Elsässer[5], D. Raabe [1]

[1]Department of Microstructure Physics and Alloy Design (MA)
[2]Department of Structure and Nano-/Micromechanics of Materials (SN)
[3]Department of Computational Materials Design (CM)
[4]Independent Research Group Nanoanalytics and Interfaces (NG)
[5]Fraunhofer Institut für Werkstoffmechanik IWM, Freiburg, Germany
[6]Karlsruher Institut für Technologie, Institut für Angewandte Materialien (IAM-CMS), Karlsruhe, Germany
[7]Central Facility for Electron Microscopy, RWTH Aachen University, Aachen, Germany
[8]Ernst Ruska-Centre for Microscopy and Spectroscopy with Electrons, Forschungszentrum Jülich GmbH, Jülich, Germany

Grain boundaries (GBs) in materials have substantial influences on device properties, for instance on mechanical stability or electronic minority carrier lifetime in multicrystalline silicon (mc-Si) solar cells. This applies especially to asymmetric, less ordered or faceted interface portions. Here, we present the complex atomic interface structure of asymmetric and faceted tilt grain boundaries in silicon, observed by high resolution scanning transmission electron microscopy (HR-STEM) and explained by atomistic modeling and computer simulation. As an outlook, newest results of a faceted Σ3 GB analyzed by HR-STEM and atom probe tomography (APT) are presented as well as first results of microscale fracture tests.

Hardware aberration corrected HR-STEM enables us to distinguish individual atomic column positions having projected distances around an Ångstrom or below [1,2]. Contrary to the well-known symmetric Σ9(122) structure in Si, the atomic structure of the observed asymmetric Σ9 (111)|(115) segment shows strong distortions, but nevertheless it repeats periodically with almost perfect accuracy over a range of several 100 nm. At the interface we identify 10 Si dumbbells, which cannot be assigned to one of the two grains, as they have a completely different orientation. Furthermore, there are four apparently single-atomic columns per period. The distorted dumbbells are oriented such that they resemble the structure of several short stacking faults or "nano-Σ3 twin boundaries", consisting of only 4 to 8 atoms.

Starting from the experimental HR-STEM images, a preliminary atomistic model of the asymmetric GB was created by placing Si atoms at the intensity-peak positions. Free surfaces to a vacuum volume were introduced in the structure model to terminate the two grains in the relaxation calculations. The orthorhombic super-cell with periodic boundary conditions contains a slab of 360 Si atoms and extends over 19.95 Å along the interface, over 56.96 Å perpendicular to the interface, and over 7.679 Å along the viewing direction.

Classical atomistic molecular-statics simulations using empirical interatomic potentials, namely Tersoff [3], Stillinger-Weber [4] and EDIP [5] potentials, have been used to relax the interface structure and to calculate the GB energy. The relaxed structure shows qualitatively a good match between experiment and calculation. It turns out that the atoms in the apparently single-atomic columns are three-fold coordinated in the non-relaxed configuration, but can reconstruct to four-fold coordination by pairwise displacements along the [110] direction. Within the used super-cell eight possible reconstruction patterns exist. To study the thermodynamic stability of the GB and its dependence on the various reconstruction patterns of the single atomic columns, GB energies have been calculated. It is known that empirical potentials yield correct GB structures but overestimate interface energies [6-8]. In order to elucidate this deficit, interface energies for a set of different

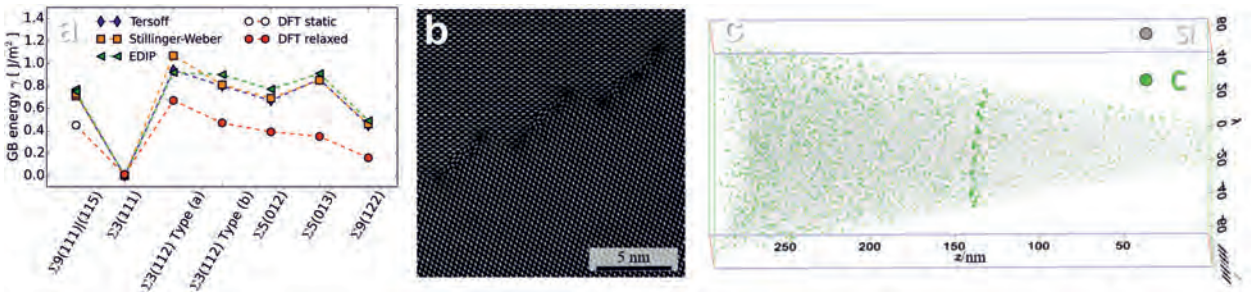

Fig. 1: *(a) Calculated GB energies for various GBs. DFT values are taken from [9]. The DFT value of the GB energy for the asymmetric Σ9(111)|(115) has been obtained from a static calculation using the relaxed structure as obtained by empirical potentials. The Σ3(112) GB types termed as (a) and (b) correspond to the symmetric and asymmetric Σ3(112) GBs, respectively in [9]. (b) Experimental HR-STEM image of faceted Σ3(112) GB. (c) Projection of 3D APT data (LEAP 5000) from the very same GB showing C segregation along lines at the GB position.*

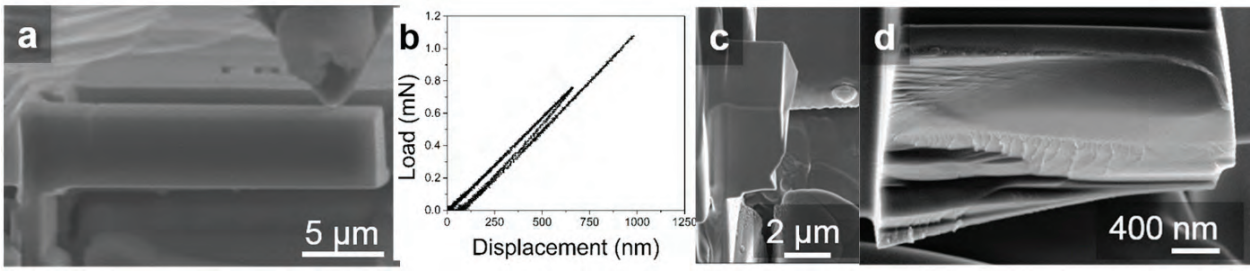

Fig. 2: *Miniaturized bending beam for fracture testing of grain boundaries in Si: (a) in situ SEM image of loading configuration (b) Load - displacement curve (load – unload cycle) obtained from in situ SEM bending, (c) side and (d) front – view images of fractured interface.*

GBs have been calculated and related to *ab-initio* density functional theory (DFT) results which have been previously obtained [9]. The energy of the observed structure is found to be in the range of the highly symmetric low-Σ GBs, Fig. 1(a). This explains its stability over a large spatial region of more than 100 nm. The relaxation of the GB structure into a sequence of short Σ3 nano-TB segments could be one reason for the surprisingly low energy values for this complex GB structure.

For further atomistic simulations and a complete understanding of the GB physics, it would be of highest interest to know the GB chemistry with highest accuracy. To face this problem, we combined the sample preparation of HR-STEM thin foils with the sample preparation of APT tips by focused ion beam (FIB). This enables us now to analyze the structure of a GB by HR-STEM and the chemistry of the same GB by APT. A first result is shown in Fig. 1, where (b) shows the facets of a Σ3(112) GB and (c) shows C segregation along lines at the GB position in the 3D APT data. This suggests a preferential segregation of the C impurities at special GB features. The additional chemical information can be implemented into the simulations in the future and will lead to a more thorough understanding of GBs in general.

Si as a brittle material permits to perform miniaturized fracture experiments as we have recently proved with different small scale fracture experiments all fulfilling linear elastic fracture mechanics [10]. Currently, we try to determine with notched bending beams the interfacial fracture toughness values of the grain boundaries described above, Fig. 2. The values will be compared to the work of separation obtained by DFT calculations and the fracture paths characterized by electron microscopy and AFM studies.

In conclusion we studied the atomic structure of asymmetric and faceted GBs in mc-Si by HR-STEM. In case of the Σ9(111)|(115) interface an energetically favorable substructure is found explaining the surprisingly low GB energy found in the molecular statics calculations. Correlation of HR-STEM and APT data allows access to the exact GB chemistry and will improve the atomistic simulations in the future.

References

1. N. Dellby, O. L. Krivanek, P. D. Nellist, P. E. Batson, and A. R. Lupini: J Electron Microsc (2001) 50, 177.
2. O. Krivanek, P. Nellist, N. Dellby, M. Murfitt, and Z. Szilagyi: Ultramicroscopy (2003) 96, 229.
3. J. Tersoff: Physical Review B (1988) 38, 9902.
4. F. H. Stillinger and T. A. Weber: Physical review B (1985) 31, 5262.
5. J. F. Justo, M. Z. Bazant, E. Kaxiras, V. Bulatov, and S. Yip: Physical review B (1998) 58, 2539.
6. P. Keblinski, D. Wolf, S. Phillpot, and H. Gleiter: Journal of materials research (1998) 13, 2077.
7. V. Y. Lazebnykh and A. S. Mysovsky: arXiv preprint arXiv:1308.3802 (2013).
8. S. Von Alfthan, P. Haynes, K. Kaski, and A. Sutton: Physical review letters (2006) 96, 055505.
9. B. Ziebarth, M. Mrovec, C. Elsässer, and P. Gumbsch: Physical Review B (2015) 91, 035309.
10. B. N. Jaya, C. Kirchlechner, and G. Dehm: Journal of Materials Research (2015) 30, 686.

Integrated Experimental-Numerical Analysis of Stress and Strain Partitioning in Multi-Phase Alloys

C.C. Tasan, M. Diehl, D. Yan, F. Roters, D. Raabe

Department of Microstructure Physics and Alloy Design (MA)

Advanced alloys typically have microstructures composed of multiple phases. Through thermo-mechanical control of the crystallography, composition, morphology and relative fractions of these structural units, a wide property spectrum can be accessed. It is however a challenging task to design optimal microstructures that would satisfy the property combination specifications for a given application. In the case of automotive steels, for example, a coupled increase in both strength and toughness is sought for simultaneous improvements in weight reduction and crashworthiness. Yet, micro-mechanically verified microstructure design guidelines that would allow achieving this goal, are at present not available. To this end, an experimental-numerical methodology has been developed at the MPIE that enables high resolution tracking of deformation induced microstructure, micro-strain and micro-stress fields, through *in-situ* scanning electron microscope (SEM) deformation experiments and accompanying crystal plasticity simulations (Fig. 1) [1].

Both, experiments and simulations, start with electron backscatter diffraction (EBSD). In the former, to allow simultaneous micro-strain and microstructure mapping, a recently developed digital imaging correlation (DIC) technique is employed that provides strain maps without inhibiting microstructure mapping by EBSD, electron channelling contrast imaging (ECCI) and scanning electron (SE) imaging measurements. The simulation route uses the EBSD map to create a crystallographically informed numerical model with phase properties obtained from inverse crystal plasticity finite element method (CPFEM) simulations of nanoindentation experiments. Using a recently developed spectral solver suitable for heterogeneous materials with high mechanical phase contrast and nonlinear stress–strain response, full-field CP simulations are carried out (Fig. 1).

The approach has so far been applied to martensitic steels, bainitic steels and martensitic-ferritic steels [2,3]. As shown in Fig. 2 for the latter, the overall approach provides a unique overview of

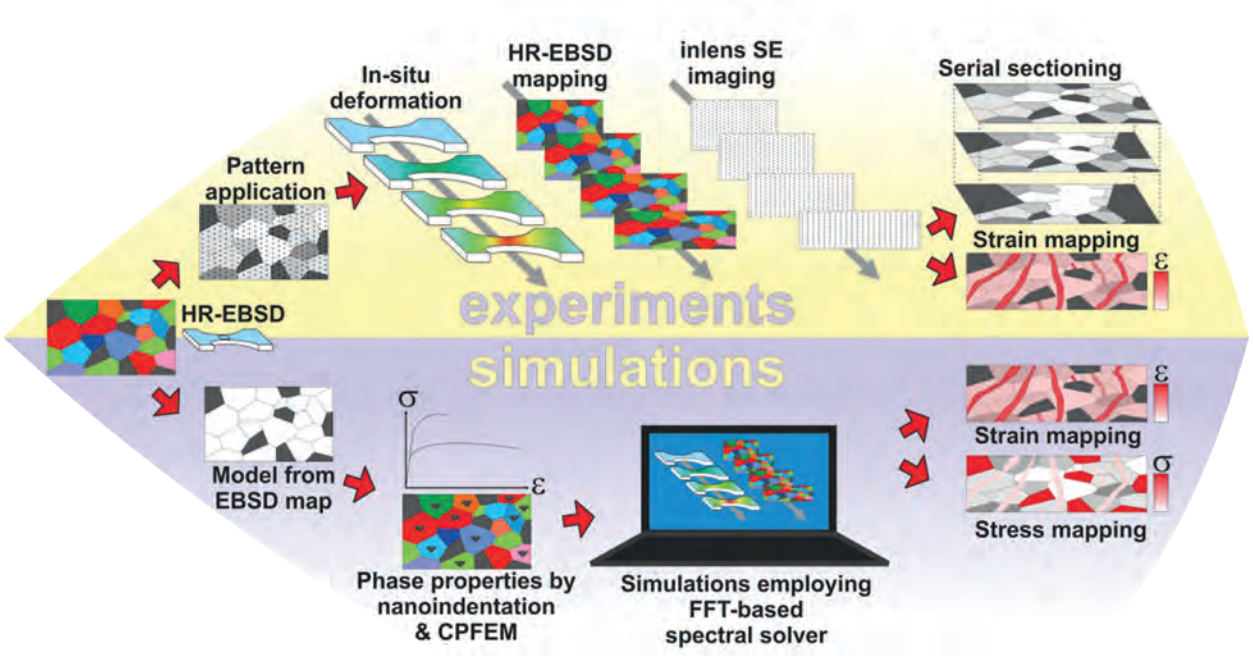

Fig. 1: *The integrated approach involves experiments and simulations both proceeding from the same EBSD-mapped microstructure data set, providing the local strain and stress distribution maps as well as the microstructure changes [1].*

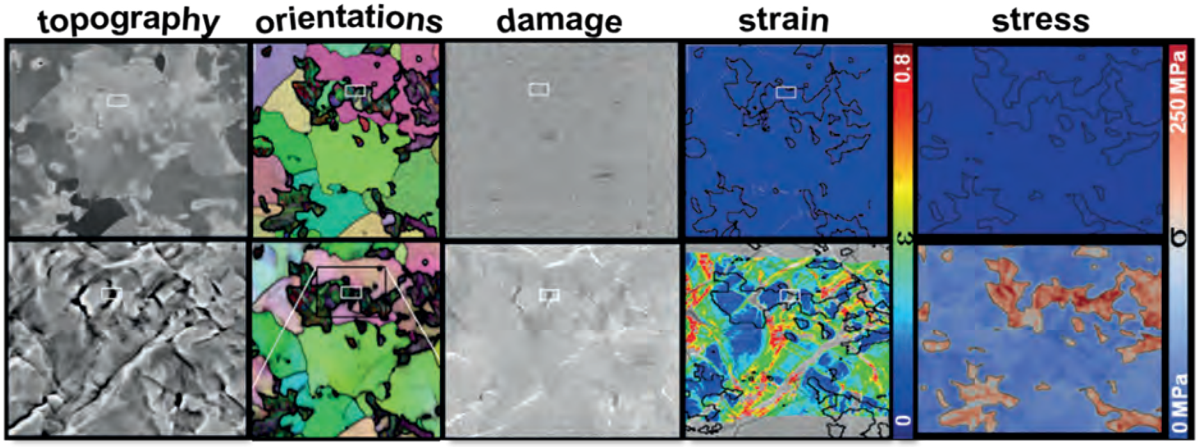

Fig. 2: *The results of dual phase steel: SE imaging reveals topography, EBSD reveals orientation changes, inlens SE images reveal damage incidents, DIC reveals local strains, and CP simulations reveal the local stresses [2, 3].*

all the inter-linked micro-processes taking place during deformation: topography formation, crystallographic rotations, damage nucleation, strain and stress localization, etc. The realm of data produced thus reveals various key insights on how novel alloys can be developed for targeted mechanical response [3].

References

1. C.C. Tasan, M. Diehl, D. Yan et al.: Acta Mat (2014) 81, 386-400.
2. C.C. Tasan, J.P.M. Hoefnagels, M. Diehl et al.: Int J Plasticity (2014) 63, 198-210.
3. D. Yan, C.C. Tasan, D. Raabe: Acta Mat (2015) 96, 399-409.

Broadband Reflecting Microfibers with Tailored Structures Inspired by Desert Ants

H. Fabritius [1], X. Wu [1], A. Erbe [2]

[1]Department of Microstructure Physics and Alloy Design (MA)
[2]Department of Interface Chemistry and Surface Engineering (GO)

Over millions of years, living organisms have evolved and optimized complex, three-dimensional structures on length scales suitable to interact with and manipulate solar light, thus achieving effects that are essential for their survival, like signaling, camouflage or warning [1]. Despite consisting of low refractive index materials, they show highly adapted and efficient photonic properties that have attracted the attention of scientists aiming at the design and development of new optical materials [2, 3]. So far, the majority of such studies have concentrated on structures exhibiting periodical order [4, 6]. However, an increasing number of recent studies shows that nature also evolved photonic structures featuring various degrees of disorder [7], which display well defined optical properties that could not be achieved with periodically ordered structures consisting of the same materials.

In terms of adaptation to specific habitats, deserts are particularly challenging for insects due to the extreme variations in temperature and the extreme insolation during day-time. Nevertheless, ants (Insecta, Hymenoptera, Formicidae) like the Saharan silver ant Cataglyphis bombycina (Fig. 1a) have successfully adapted by evolving long legs to keep the body away from the hot sand, visual orientation based on the position of the sun instead of pheromone orientation and the ability to produce sophisticated heat shock proteins that ensure the function of their metabolism at very high body temperatures [8]. The body of these ants is densely covered with setae (Fig. 1a) that give them a metallic silver-like sheen (Fig. 1b). This indicates that the optical properties of the setae are adapted to shield the animals from sunlight through broadband reflection, thus preventing additional heating up. The fact that setae are fibres makes them a very interesting photonic system that is suitable as a biological blueprint for the development of novel synthetic organic fibres with tailored reflective properties.

Structural characterization of the setae shows the elongated, needle like shape of the setae (Fig. 1b) which are uniformly about 80µm long and have a thickness of about 3.5 µm. Their cross section has the shape of an isosceles triangle. Both lateral surfaces of each setae are decorated with a quasi-ordered pattern of longitudinal microribs with a spacing varying between 180 and 220 nm (Fig. 1c). The underside of the setae is flat and unstructured (Fig. 1c, insert). Every setae is pervaded by an irregularly shaped central canal (Fig. 1d). Fractured setae reveal a solid interior consisting of densely packed filaments that appear to be co-oriented with their long axis (Fig. 1e). In the larger bundles of setae observed in densely covered cuticle areas, the setae are randomly stacked and are connected in the contact areas by a soft, waxy material (Fig. 1g). Measurements of the overall reflectance of exoskeleton parts covered with setae using Fourier transform infrared (FTIR) spectroscopy show broadband reflection resulting from homogeneous reflection and scattering of all wavelengths with an efficiency of up to 40% (Fig. 2a). Transmittance spectra of isolated setae placed on glass slides (Fig. 2b) show

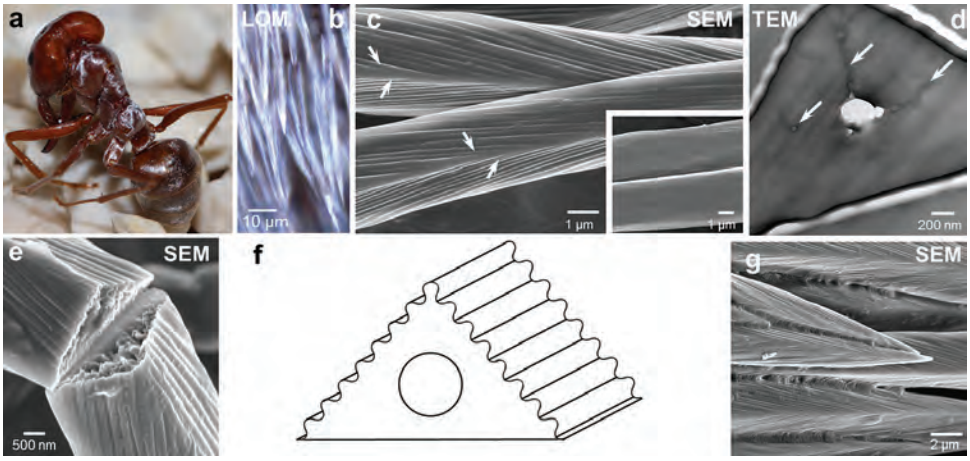

Fig. 1: *(a) Habitus of Cataglyphis bombycina workers. (b) Light micrograph of bundles of setae. (c) Electron micrograph of individual setae showing their triangular shape and the microribs (arrows) covering the side surfaces. The insert shows the smooth unstructured underside of the setae. (d) Transmission electron micrograph showing the central canal. (e) Cross-fractured setae revealing the disordered internal structure. (f) Schematic depiction of the setae architecture. (g) Cluster of setae where the contact areas are fused by a waxy substance.*

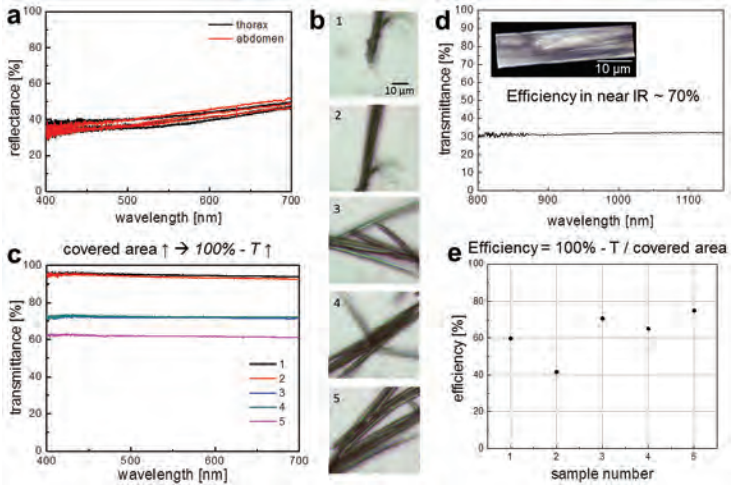

Fig. 2: *(a) Reflectance spectra recorded on different parts of the body of Cataglyphis bombycina. (b) Areas of glass slides covered with setae used for the transmittance experiments. (c) Transmittance spectra recorded for the samples in (b). (d) Transmittance spectrum of setae (insert) in near IR. (e) Shielding efficiency of the setae as ratio covered area / 100% - T.*

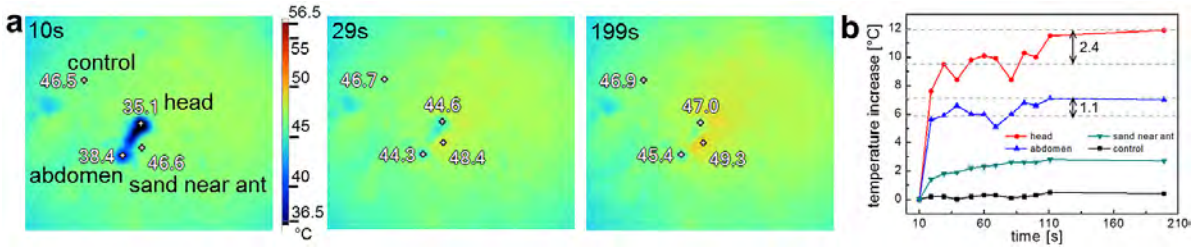

Fig. 3: *(a) Thermographic images recorded at 10s, 29s and 199s after placement of the ant, the numbers are temperature values [°C]. (b) Diagram of the temperature increase with exposure time monitored for head and abdomen of the ant and the sand substrate. The arrows between dashed lines indicate the temperature increase of head and abdomen between 29 s and 199 s exposure time.*

that if the covered area increases, the transmittance decreases (Fig. 2c). The calculated efficiency of shielding light for the setae can be as high as 75% for the visible (Fig. 2e) and 70% for the near infrared (IR) wavelength ranges (Fig. 2d).

This shows that the setae are very efficient in shielding from solar radiation. The thermoregulatory function of the setae is confirmed by thermographic analysis of the ant body in a setup simulating their native environmental conditions (Fig. 3a). The results show that the temperature of the abdomen, which is densely covered with setae, increases slower than the temperature of the head where only few setae are present (Fig. 3b).

The overall goal of this interdisciplinary collaboration between the MPIE and Paderborn University is to establish design rules for artificial organic textile fibers with highly efficient broadband reflection properties that are generated by an irregular architecture and tailored structural disorder on the micro- and nanoscopic length scale. Further structural, compositional and optical characterization combined with a theoretical study of their function will yield complete sets of data that can be used to fabricate polymer-based biomimetic high-reflectivity fibers using techniques like direct laser writing in collaboration with Prof. von Freymann, University of Kaiserslautern and Prof. Zollfrank, Technische Universität München.

References

1. Doucet, S.M., Meadows, M.G.: J. R. Soc. Interface (2009) 6, 115-132.
2. Potyrailo, R. A.; Ghiradella, H, Vertiatchikh, A., Dovidenko, K., Cournoyer, J. R., Olson, E.: Nature Photonics (2007) 1,123–128.
3. Hallam, B., Hiorns, A. G., Vukusic, P.: Applied Optics (2009) 48, 3243-3249.
4. Wu, X., Erbe, A., Raabe, D., Fabritius, H.: Adv. Funct. Mater (2013) 23, 3615-3620.
5. Vukusic, P., Sambles,J. R.: Nature (2003) 424, 852-855.
6. Kinoshita, S.: Structural Colours in the Realm of Nature. World Scientific (2008).
7. Wiersma, D.S.: Nature Photonics (2013) 7, 188-196.
8. Lenoir, A., Aron, S., Cerda, X., Hefetz A.: Israel Journal of Entomology (2009) 39, 1-32.

Magnetism at the Domain Walls of an Epitaxial Oxide Thin Film

S. Venkatesan [1], S. Farokhipoor [2], C. Magén [3,4], J. Íñiguez [5], C.J.M. Daumont [2], D. Rubi [2], E. Snoeck [6], M. Mostovoy [2], C. de Graaf [2,7], A. Müller [8], M. Döblinger [9], B. Noheda [2], C. Scheu [8]

[1]Department of Structure and Nano-/ Micromechanics of Materials (SN)
[2]Zernike Institute for Advanced Materials, University of Groningen, The Netherlands
[3]Laboratorio de Microscopías Avanzadas (LMA), Instituto de Nanociencia de Aragón (INA) - ARAID, and Departamento de Física de la Materia Condensada, Universidad de Zaragoza, Spain
[4]Transpyrenean Advanced Laboratory for Electron Microscopy (TALEM), CEMES-INA, CNRS-Universitat de Zaragoza, Spain
[5]Institut de Ciència de Materials de Barcelona (ICMAB-CSIC), Bellaterra, Spain
[6]CEMES-CNRS, Toulouse, France
[7]Universitat Rovira i Virgili, Tarragona and Institució Catalana de Recerca i Estudis Avançats (ICREA), Barcelona, Spain
[8]Independent Research Group Nanoanalytics and Interfaces (NG)
[9]Department of Chemistry and Center for Nanoscience, LMU, Munich, Germany

The coupling between magnetic and ferroelectric order parameters in magnetoelectric multiferroics has drawn considerable research interest due to their potential application as multifunctional devices [1]. Among perovskite manganite based multiferroics, orthorhombic $TbMnO_3$ (TMO) is a prominent candidate because of its large magnetoelectric coupling and since its ferroelectric state is directly coupled to the magnetic structure. In bulk orthorhombic TMO below 28 K, the magnetic interactions between nearest neighbours and next-nearest neighbours stabilize a cycloidal spin structure of the Mn sublattice. The magnetic cycloid breaks inversion symmetry and induces a macroscopic electrical polarization (via the inverse Dzyaloshinskii-Moriya interaction). Thus, TMO is a multiferroic material with a strong magnetoelectric coupling. Additionally, TMO exhibits a sinusoidal antiferromagnetic state which exists between 28 K and the Neel temperature at 42 K [2,3].

Epitaxially stabilized thin films offer the possibility of utilizing the misfit strain to have additional degrees of freedom for tuning the properties that are different from the bulk. The misfit strain allows the system to have different symmetries and nanometer sized regions that exhibit new functionality, e.g. epitaxial TMO films grown on $SrTiO_3$ (STO) substrates exhibit net magnetic moments. The proposed origin for the

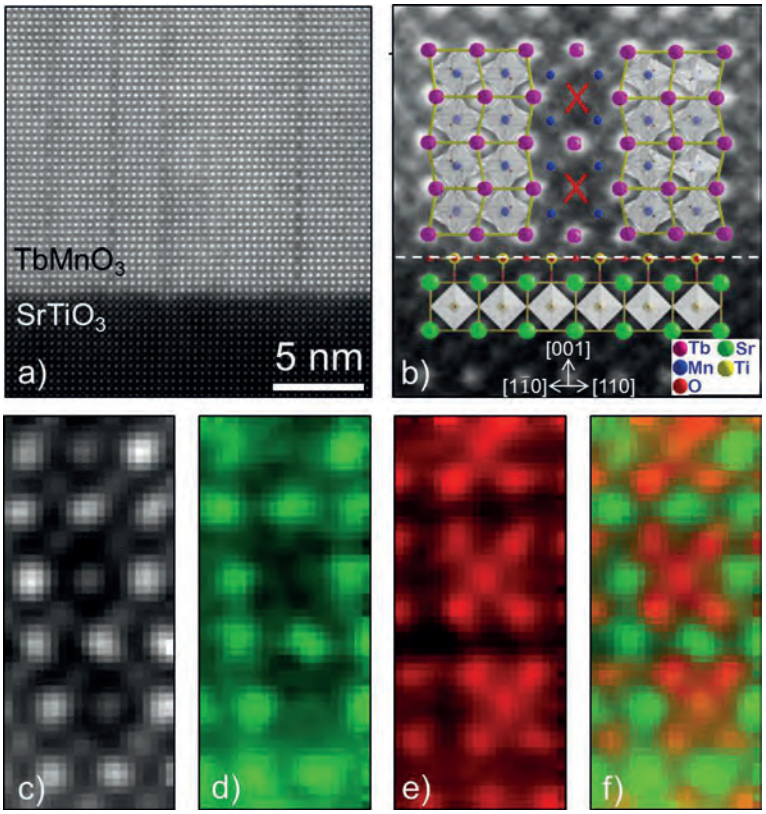

Fig. 1: *a) Atomic resolution HAADF-STEM image showing the interface of $TbMnO_3$ on $SrTiO_3$ substrate. Domain walls are seen as a vertical line in the $TbMnO_3$ thin film. b) Crystallographic structure and orientation relationship is overlaid on the domain wall for better visualization. The position "X" in the image is where the additional Mn atom is detected. c) HAADF signal collected simultaneously during the spectrum image acquisition of the domain wall. d) and e) Integrated intensities of the Tb $M_{4,5}$ and Mn $L_{2,3}$ edges from the spectrum image. f) Overlay image of d) and e) showing the clear presence of an additional Mn atom replacing Tb. Image adapted from [6].*

net magnetic moments in this system has been attributed to epitaxial strain-induced unit cell deformation, leading to the changes in their magnetic interaction. However, the epitaxial strain at the substrate - film interface alone does not reveal the reason behind the observed phenomena [4]. With the help of atomically resolved high angle annular dark field scanning transmission electron microscopy (HAADF-STEM) and electron energy loss spectroscopy (EELS), in addition to the different crystallographic domain [5] we have found a one atomic layer thin domain wall with distinct chemical signature. Investigating this domain wall with a state-of-the-art transmission electron microscope resolved the origin of the ferromagnetic phase in TMO [6]. The high strain concentrated at the domain wall modifies the structure and composition along the domain wall. The domain wall consists of an additional Mn atom in the position of the Tb atom. The canting of the Mn spin is responsible for the observed net magnetic moments. The long range spiral spin ordering along the domain structure is disturbed by the presence of the domain wall. The density of the domain wall can be tuned upon the thickness allowing up to 25 percent of the total volume. We have also established a relationship between the density of domain wall, film thickness and net magnetization in the film. The detailed magnetic studies, density functional theory and embedded cluster calculation performed by our collaborators explain the contribution of the domain wall towards the net magnetization observed in these films. Further, we also believe that this kind of novel structures that are normally absence in bulk can be synthesized in thin films by making use of epitaxial misfit strains. This new class of thin 2-dimensional sheets with unique functional properties opens the door for novel applications in nanoelectronics [6].

References

1. Hur, N.; Park, S.; Sharma, P.A.; Ahn, J.S.; Guha, S.; Cheong, S.-W.: Nature 429 (2004) 392.
2. Kimura, T.; Goto, T.; Shintani, H.; Ishizaka, K.; Arima, T.; Tokura, Y.: Nature 426 (2003) 55.
3. Daumont, C.J.M.; Mannix, D.; Venkatesan, S.; Catalan, G.; Rubi, D.; Kooi, B.J.; De Hosson, J.T.M.; Noheda, B.: J. Phys. Condens. Matter 21 (2009) 182001.
4. Venkatesan, S.; Daumont, C.J.M.; Kooi, B.J.; Noheda, B.; De Hosson, J.T.M.: Phys. Rev. B. 80 (2009) 214111.
5. Venkatesan, S.; Döblinger, M.; Daumont, C.; Kooi, B.; Noheda, B.; De Hosson, J.T.M.; Scheu, C.: Appl. Phys. Lett. 99 (2011) 222902.
6. Farokhipoor, S.; Magén, C.; Venkatesan, S.; Íñiguez, J.; Daumont, C.J.M.; Rubi, D.; Snoeck, E.; Mostovoy, M.; de Graaf, C.; Müller, A.; Döblinger, M.; Scheu, C.; Noheda, B.: Nature 515 (2014) 379.

Interplay between Defects and Reactive Surfaces

M. Todorova [1], C. Freysoldt [1], S. Wippermann [2]

[1] Department of Computational Materials Design (CM)
[2] Department of Interface Chemistry and Surface Engineering (GO)

An accurate description of solid/liquid interfaces and the elementary processes occurring on them is a prerequisite to understanding their reactivity, which is the key to most electro-chemical and colloidal processes of practical importance. It encompasses (but is not limited to) knowledge about interface structures, their stability, growth and evolvement, which directly couples to defects and their impact, e.g., on reactions.

One illustrative example is the formation of oxide films on metal surfaces, which can dramatically increase the corrosion resistance of materials and are of utmost importance when we consider the tremendously important role metals play in our society. A key quantity to understand the growth/dissolution of protective oxide films is the knowledge which defects are present in the oxide in appreciable concentrations and a given electrochemical environment. Utilising the vast knowledge about charged point defects in semiconductors [1] and our recently developed approach that unifies concepts in semiconductor physics and electrochemistry [2] we gained surprising new insights into the Zn/ZnO/H_2O system [3].

Extending the concept of Pourbaix diagrams, which show the most stable bulk and defect (ions in water and other solvents) phases as a function of pH and overpotential, we proposed a scheme to construct defect phase diagrams which span the relevant range of configurational space as defined by the accessible potentials for the chemical species and the electrons [3]. These new diagrams (Fig.1) yield the dominant defect for any thermodynamically allowed combination of oxygen chemical potential and overpotential, and, being formally equivalent to a Pourbaix diagram, are also easily combined with the well-established electrochemical stability region of water (region between the two dashed black lines in Fig.1). The application of the approach to the seemingly extremely well studied oxide ZnO revealed a number of surprises, the most striking result being that charge neutral defects become dominant under electrochemically relevant conditions. Because such defects behave qualitatively different compared to charged ones, such an observation directly impacts strategies aiming to enhance corrosion resistance, by making a passivation layer more intrinsic.

The proposed efficient and physically transparent way of identifying the relevant defects in a passivation layer under realistic electrochemical conditions can help to develop systematic approaches to search for alloys with improved corrosion resistance. In order to model an interface in detail, however, it is necessary to take into account that defects right at the interface may exhibit modified or even unique properties. Even though the actual structure of the interface is often not known well experimentally, *ab initio* simulations of idealized surface and interface structures help to identify the key features of real interfaces. An important aspect is the electric behaviour of the interface. For instance, the appearance of interface states in the band gap of a semiconductor or insulator will pin the Fermi level at the interface to this state. Electrically active interface defects may play a similar role.

Ab initio calculations can identify the atomistic origin of such defect states by investigating candidate structures in different charge states. The interface is

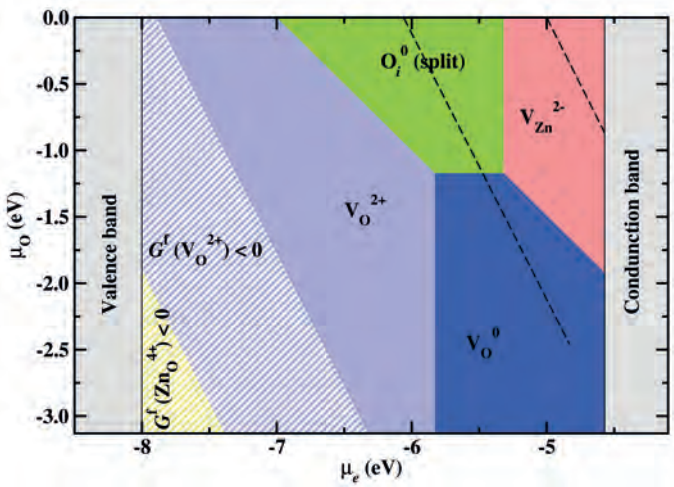

Fig. 1: *Defect stability phase diagram for the Zn/ZnO/H_2O system visualizing dominant defects and conditions for which water is electrochemically stable (region between the dashed black lines).*

typically modelled as a supercell containing several layers on both sides of the interface, and assuming periodic boundary conditions in all three dimensions. Such ordered structures do not directly yield the energetics of randomly distributed, independent defects of interest, notably in charged states where long-range Coulomb potentials and the necessity to introduce a compensating background result in significant variations between different supercells. To correct for these "artefacts", we recently developed a correction scheme along the lines of the sxdefectalign correction scheme for bulk defects [4]. Solving the Poisson equation for the isolated and periodic case with a spatially varying dielectric constant makes it possible to extrapolate the energies of the isolated case already from rather small systems (Fig. 2).

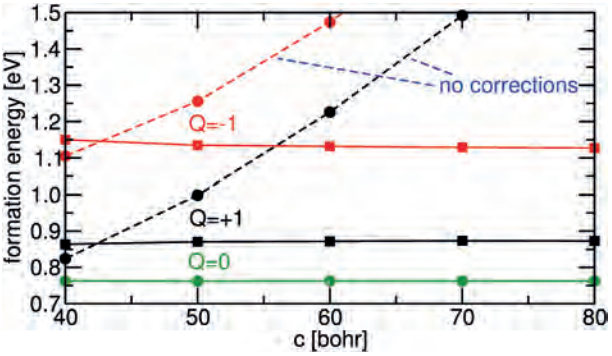

Fig. 2: *Improved convergence of the defect properties with supercell size for a dangling-bond defect at the H-covered Si(111) surface for different vacuum thicknesses and a 2x2 surface cell. Dashed lines connect values as obtained from density functional theory (DFT) calculations, solid lines include electrostatic corrections.*

An example for an application, in which interfacial defects are particularly important are nanoparticles (NPs) embedded in a host matrix, in the context of light emission and solar energy conversion. The resulting electronic and optical properties of such composites are mainly dominated by interfaces. However, very little is known structurally about these composites. In experiment, probing such nano-interfaces with atomic resolution, especially buried ones between the NPs and the surrounding matrix, is extremely challenging.

In the independent NanoMatFutur group „Semiconducting nanocomposites with tailored optical and electronic properties", funded by the German Federal Ministry for Education and Research (BMBF), we investigated NPs with core structures made from exotic Si and Ge allotropes. These are of particular interest with respect to multi-exciton generation (MEG), where one incoming photon creates multiple electron-hole pairs. Calculating MEG rates from first principles, we demonstrated the metastable BC8 phase of Si to feature band gaps that are much more suitable for solar energy conversion and significantly higher MEG rates compared to diamond-like Si NPs [5]. BC8 NPs can now be synthesized and stabilized kinetically in colloidal solutions. Employing massively parallel *ab initio* molecular dynamics we prepared models of matrix embedded Si NPs (cf. Fig. 3). Our calculations predict that low defect densities and favourable band alignments at the NP-matrix interface, obtained from many body perturbation theory, can indeed be achieved [6].

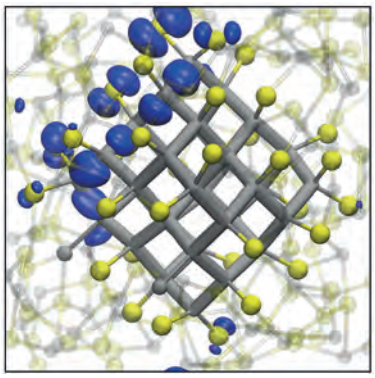

Fig. 3: *Si_{35} NP with sulfur shell embedded in a-ZnS. The HOMO state, illustrated by blue iso surfaces, is localized to the sulfur shell [6].*

To interpret experiments and model the NP-matrix interface in detail, we investigate the various NP surface orientations present at the interface by *ab initio* thermodynamics. The employed wet chemical synthesis techniques require taking the solid-liquid interface at the NP surface and the presence of charged species into account. In particular defects in different charge states are expected to have a strong impact on the composites' electronic and optical properties.

References

1. C. Freysoldt, B. Grabowski, T. Hickel, J. Neugebauer, G. Kresse, A. Janotti, and C. G. Van de Walle: Rev. Mod. Phys (2014) 86, 1.
2. M. Todorova and J. Neugebauer: Phys Rev Appl (2014) 1, 014001.
3. M. Todorova and J. Neugebauer: Faraday Discuss. (2015) 180, 97.
4. C. Freysoldt, C. G. van de Walle, J. Neugebauer: Phys Rev Lett (2009) 102, 016402.
5. S. Wippermann, M. Vörös, D. Rocca, A. Gali, G. Zimanyi, G. Galli: Phys Rev Lett (2013) 110, 046804.
6. S. Wippermann, M. Vöros, A. Gali, F. Gygi, G. Zimanyi, G. Galli: Phys Rev Lett (2014) 112, 106801.

Hydrogen Detection in Ni-Nb Model Alloy

Z. Tarzimoghadam [1], M. Rohwerder [2], P. Dey [3], D. Ponge [1], D. Raabe [1]

[1]Department of Microstructure Physics and Alloy Design (MA)
[2]Department of Interface Chemistry and Surface Engineering (GO)
[3]Department of Computational Materials Design (CM)

Due to its excellent corrosion resistance, the Ni-based Alloy 718 is often used in applications, where it is exposed to hydrogen, such as sour gas environments in oilfields. Since the danger of hydrogen embrittlement (HE) under these conditions seems to correlate with the mechanical properties, the accepted strength classes in the applications are limited. Our research supports the hypothesis that it is the microstructure that determines the sensitivity to HE. In particular, it has been shown [1] that the δ-Ni_3Nb phase plays a significant role in altering HE sensitivity of alloy 718. Furthermore, H-induced vacancies have recently been reported to support HE. With our experimental and theoretical investigations we achieve a better understanding of the real mechanisms behind these assumptions.

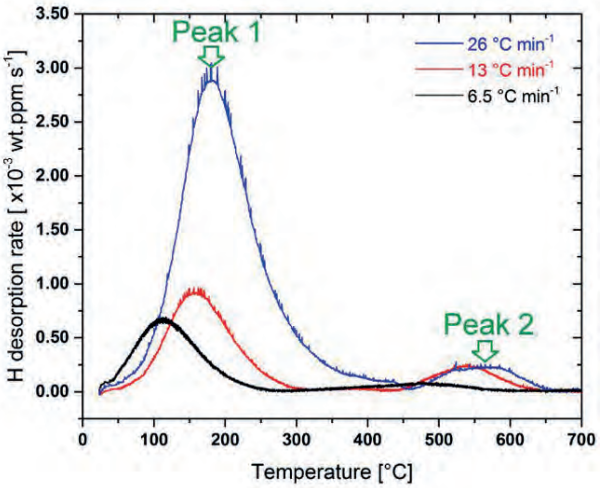

Fig. 1: *Hydrogen thermal desorption spectra of Ni-22wt.-%Nb alloy at different heating rates.*

Major achievements have been made in identifying the hydrogen trapping states and visualizing the hydrogen distribution in the microstructure, which are of primary importance for a concurrent discussion of the H-assisted failure mechanism. Our novel approach correlates measurements using Thermal Desorption Spectroscopy (TDS), Ag decoration technique [2], Scanning Kelvin Probe Force Microscopy (SKPFM) with Pd detection layer [3], and Secondary Ion mass Spectrometry (SIMS). A binary Ni-22wt%Nb model alloy was used to narrow down the parameters of the complicated microstructure in alloy 718 and to elucidate the H distribution and desorption behaviour of the δ-Ni_3Nb intermetallic phase with respect to the γ-matrix.

The relevance of the δ-Ni_3Nb phase was first identified by TDS measurements, where H desorption peak (peak 2) corresponding to an activation energy of 51 kJ mol^{-1} was detected in addition to the typical peak for the γ-matrix (peak 1, 22 kJ mol^{-1}).

The picture looks differently, if locally resolved methods to detect diffusible hydrogen are used: The Ag decoration technique, for example, which uses the special activity of atomic H on a metal surface to reduce Ag ions into elemental Ag, revealed no noticeable desorption of diffusible H from the δ-Ni_3Nb phase (Fig. 2). This result was also confirmed by SIMS, a highly sensitive surface technique. Measuring the deuterium distribution in the model alloy, a higher content in the γ-matrix, correlated with higher H solubility was observed (Fig. 3). Finally, even the more sophisticated SKPFM measurements (Fig. 4), which use a Pd detection layer to resolve the kinetics of H desorption behaviour from the microstructural constituents with high spatial resolution, show a dominating release of H from the γ-matrix until around 100 h.

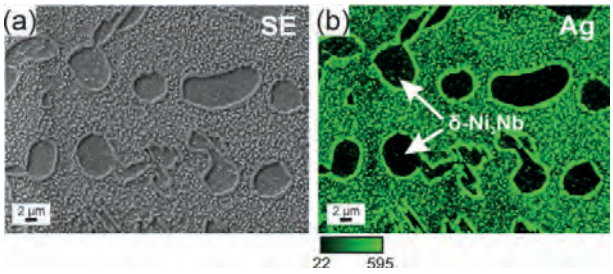

Fig. 2: *Specimen charged with H: (a) SE image of the Ag decorated surface, showing silver particle precipitation on the γ-matrix, indicating the hydrogen flux, (b) Ag EDX map.*

These results are consistent with our *ab initio* calculations, which resulted in a solution enthalpy for H that is 0.5 meV (=50 kJ/mol) higher in the δ-Ni_3Nb phase than in the γ-matrix. The desorption activation energies that were identified by TDS for δ-Ni_3Nb can therefore not correspond to the perfect precipitate phase. According to our calculations, vacancies in the δ phase form one candidate for a deeper trapping site for hydrogen, resulting in a slower release

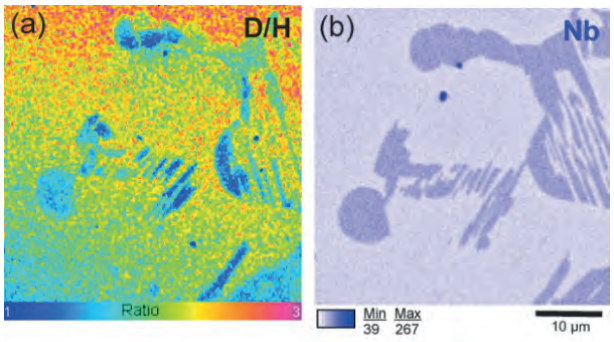

Fig. 3: *(a) Secondary ion map ($^2D^-/^1H^-$). The field of view is 40 µm. (b) Nb EDX map of the scanned area, showing the δ-Ni_3Nb phase as Nb-rich areas.*

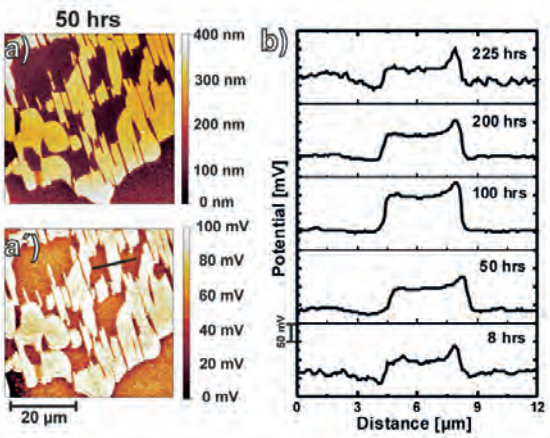

Fig. 4: *SKPFM data obtained for Ni-22wt%Nb: (a) Topography map 50 h after H charging, dark region with lower topography represents the γ-matrix, (a´) potential change on the surface after 50 h, (b) line profiles of surface potential along the black line shown in (a´) over time. Lower potentials correspond to higher H activity.*

in the SKPFM measurements. The increase of their concentration due to the interaction with multiple H atoms has been investigated in the precipitate as well as the γ-matrix phase [4], in order to understand a H-enhanced strain-induced vacancy (HESIV) formation. We reveal that gradients in the chemical potential can provide a driving mechanism for the combination of these vacancies and the formation of nanovoids as recently observed by BSE imaging and further analysed by interrupted tensile testing.

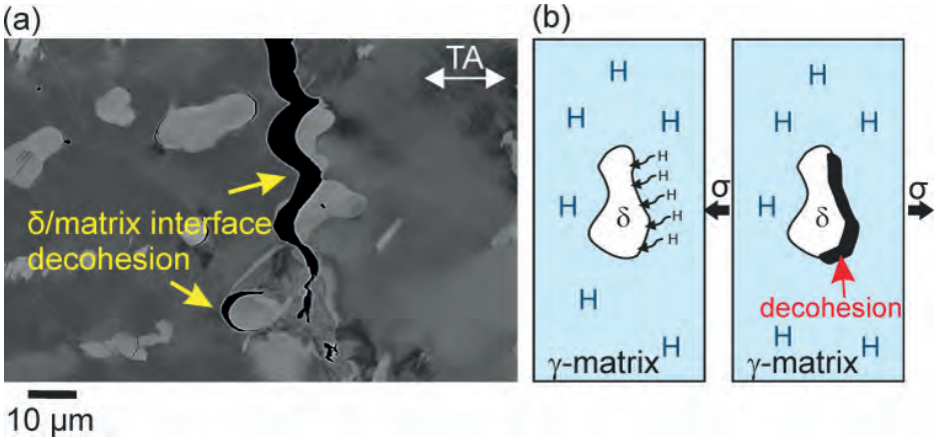

Fig. 5: *Deformation microstructure with H pre-charging: (a) BSE image showing the crack propagation along the δ/matrix interface (TA: tensile axis). (b) Schematic demonstrating the H accumulation and consequent decohesion at δ/matrix interface under an applied stress* σ.

The interface between δ-Ni_3Nb phase and the γ-matrix provides another region of significantly increased trapping and activation energies and is therefore subject to ongoing experimental and theoretical investigations. The accumulation of H at the δ/matrix interfaces under applied loads can lead to the reduction of bonding strength and concurrent decohesion on straining, giving rise to the H-enhanced decohesion (HEDE) mechanism. Indeed, our mechanical testing revealed that such a δ/matrix interface decohesion takes place in the investigated Ni-alloys (Fig. 5a).

References

1. Liu L., Tanaka K., Hirose A., Kobayashi K.F.: Sci Tech Adv Mater (2002) 3, 335.
2. Schober T., Dieker C.: Metallurgical Transactions A (1983) 14A, 2440.
3. Evers S., Senöz C., Rohwerder M.: Sci Tech Adv Mater (2013) 14, 014201.
4. Nazarov R, Hickel T, Neugebauer J.: Physical Review B (2014) 89.

Insight into the Growth of Iron Sulfide Layers in Saturated H_2S Saline Solutions

G. Genchev [1], M. Ilhan [2], K. Cox [1], A. Sarfraz [1], T. H. Tran [1], C. Bosch [3], M. Spiegel [3], H. Springer [4], M. Todorova [2], A. Erbe [1]

[1]Department of Interface Chemistry and Surface Engineering (GO)
[2]Department of Computational Materials Design (CM)
[3]Salzgitter Mannesmann Forschung GmbH, Duisburg, Germany
[4]Department of Microstructure Physics and Alloy Design (MA)

Corrosion of iron in H_2S containing solutions is a common problem in oil production and is generally referred to as sour corrosion. Aqueous H_2S solutions promote corrosion of steels, but the exact nature and mechanisms of corrosion strongly depend on the reaction conditions. While the process has been widely investigated for pure iron and carbon steels, there is still a lack of understanding of the reaction path and electronic structure of the corrosion products [1].

For a systematic investigation of corrosion mechanisms, metal was polarized above the corrosion potential in a H_2S-saturated electrolyte to enhance the anodic reactions [2]. Anodic polarisation on iron in de-aerated H_2S saturated acetic saline solutions leads to the growth of an oxide-rich corrosion product with the tetragonal FeS modification mackinawite as the only crystalline component. The mackinawite grows in the (001) direction perpendicular to the base material surface (Fig. 1).

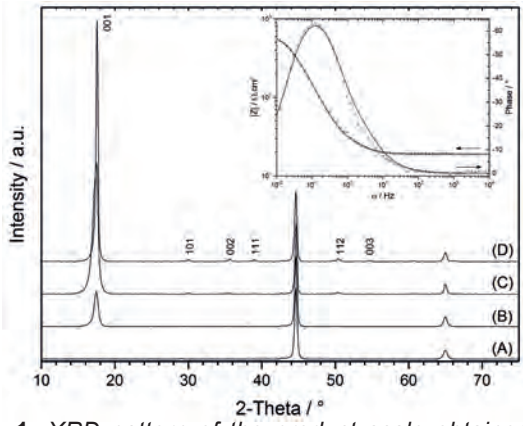

Fig. 1: *XRD pattern of the product scale obtained by anodic polarization of iron for (A) 0 min, (B) 30 min, (C) 120 min, and (D) 240 min. The corrosion product contains the mineral mackinawite without any further detectable crystalline impurities. The reflections at 44.5° and 65° arise from the iron base material. Inset: Bode plot derived from EIS measurement for an iron sample after anodic polarization experiment.*

Optical transmission measurements in the mid and far infrared (IR) have been used to obtain more detailed information about the electronic structure of the electrochemically synthesized FeS. The high absorbance without visible features from vibrational modes throughout the investigated spectral range (4000 - 50 cm-1; 495.9 – 6.2 meV) is characteristic for a strong absorption from electronic transitions. The investigated corrosion products hence do not possess a band gap above the thermal energy at room temperature and are therefore metallic, semi-metallic, or semiconducting with a very low band gap. This result is in agreement with electrochemical behaviour observed: the anodic branch of the linear polarization experiments does not show formation of a protective layer, and charge-transfer resistance determined by electrochemical impedance spectroscopy (EIS) is low (Fig. 1, inset).

X-ray photoelectron spectroscopy sputter depth profiling was used to analyse corrosion products. The results point to the formation of a duplex layer, with an oxide-rich inner part and an oxide-poor outer layer. The formation of the oxide-rich inner layer close to the iron surface can be explained by a large concentration of Fe_{2+} near the interface during dissolution, and the consequent super-saturation of oxide and sulphide. Analysis of cross sections prepared by ion milling indicates that adhesion between the inner oxide-rich and outer oxide-poor layer is poor. Diffraction shows that the distance between mackinawite layers is slightly lower for mackinawite formed during the later stages of the polarization experiments, suggesting that this difference contributes to strain leading to deadhesion. Such a result extends the previous interpretation stating that adhesion between the inner mackinawite layer and outer parts consisting of other sulfide phases is poor. As x-ray diffraction (XRD) shows no crystalline oxide-containing compound (Fig. 1), amorphous fractions, or strongly disordered regions, must be present in the corrosion products.

Amorphous regions are expected to contribute to Raman spectra, however, due to the lack of availability of a normal mode analysis for mackinawite, the interpretation of the recorded spectra is still challenging. More detailed investigations using Raman spectroscopy showed the sensitivity of the formed corrosion products. A transformation of the sulfide compounds (mackinawite) to oxide phases (hematite) has been observed when conducting the experiments ex situ. To avoid the contact of the sample with air oxygen and monitor the corrosion products in their state of formation, *in situ* experiments were executed. The resulted Raman spectra contain only two strong lines at 286 cm^{-1} and 202 cm^{-1}, indicating the formation of mackinawite [3, 4].

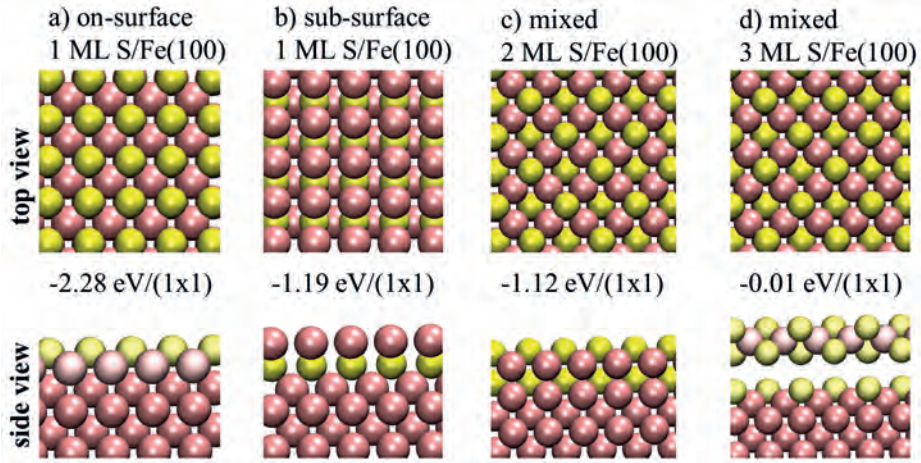

Fig. 2: *Adhesion of low coverage S adsorption phases on the Fe(100) surface. (a) on-surface adsorption of 1 ML S, (b) sub-surface adsorption of 1 ML S, (c) mixed adsorption geometry at 2 ML S forming a S/Fe/S tri-layer, (d) mixed adsorption geometry at 3 ML S, reminiscent of the S/Fe/S stacking in the (100) direction of mackinawite. S=yellow spheres, Fe=red spheres.*

Accompanying theoretical studies focused on the initial states of Fe sulfidation by investigating the adsorption behaviour of S, O and H on the Fe(100) surface by means of density functional theory calculations. These studies revealed for each of the adsorbates a strong preference for adsorption in hollow surface sties. During the ensuing competition H is pushed below the surface, as a consequence of the stronger binding of O and S to Fe. This observation is of interest in the context of H-embrittlement, as it suggests a possible reason for the H presence in Fe bulk. Since hydrogen presents no hindrance to the adsorption of S on the Fe(100) surface, increasing amounts of S attach to Fe in the vicinity of the surface. At 2 ML (at 1 ML, monolayer, the number of adsorbate atoms equals the number of substrate atoms in a layer) sulphur enters the sub-surface region forming a S/Fe/S tri-layer structure, reminiscent of the S/Fe/S planes forming along the (100) direction of mackinawite. This tri-layer adheres strongly to the Fe-substrate [-1.12 eV/(1×1) cell, Area(1×1) = 8.08 Å^2], but adding only one further layer of S significantly reduces the tri-layer's adhesion strength to the substrate. The calculated -0.01 eV/(1×1) cell for the S/Fe/S tri-layer adhesion within the severely laterally strained mackinawite [oriented in the (100) direction] forming on the surface, suggest that flakes of the newly formed corrosion product would easily fall, thus not forming a protective layer and exposing the Fe surface to further corrosion. Poor adhesion is observed experimentally – the FeS indeed does not adhere to the base materials surface well. This lack of adhesion may open the possibility for the formation of oxide-rich corrosion products.

Experimentally, oxide-containing corrosion products were also found under conditions of free corrosion. In contrast to the formation of frequently insulating oxides, a metallic corrosion product does not slow down electron transfer reactions essentially, hence does not protect the base material in the same fashion as an insulating corrosion product. Thorough understanding of corrosion processes in H_2S-containing media hence requires the analysis of the electrochemical properties of the mackinawite-containing corrosion product. An interesting perspective is the investigation of the corrosion of iron-based alloys, where suitable alloy elements may or may not lead to protecting corrosion products.

References

1. Genchev, G.; Erbe, A.: Sour gas corrosion – corrosion of steels and other metallic materials in aqueous environments containing H2S. *Submitted* to: Online Reference Database Chemistry, Molecular Sciences and Chemical Engineering, Klaus Wandelt (Editor), Elsevier, Waltham, USA
2. Genchev, G.; Cox, K.; Tran, T.H.; Sarfraz, A.; Bosch, C.; Spiegel, M.; Erbe, A.: Corros. Sci. 98 (2015) 725.
3. Hansson, E.B.; Odziemkowski, M.S.; Gillham, R.W.: Corros. Sci. 48 (2006) 3767.
4. Bourdoiseau, J.A.; Jeannin, M.; Sabot, R.; Rémazeilles, C.; Refait, P.: Corros. Sci. 50 (2008) 3247.

From Microbially Induced Corrosion to Bioelectrical Energy Conversion

P. Beese-Vasbender

Department of Interface Chemistry and Surface Engineering (GO)

Everyone knows rust on iron surfaces, caused by the reaction of atmospheric oxygen with iron that greatly reduces the service life of industrial material. Since rust is oxygen dependent, corrosion of iron would in principle be prevented by the absence of atmospheric oxygen. However, serious cases of damage to pipeline systems in the oil and gas industry frequently show up in oxygen-free soils and marine sediments, with devastating economic and ecological consequences. Hence, corrosion of iron infrastructure in anoxic environments commonly is ascribed to the metabolic activity of microorganisms, primarily sulfate-reducing bacteria and methanogenic archaea that influence electrochemical processes on the metallic surface, causing comparatively high corrosion rates of up to 0.7 mm per year [5, 6]. The

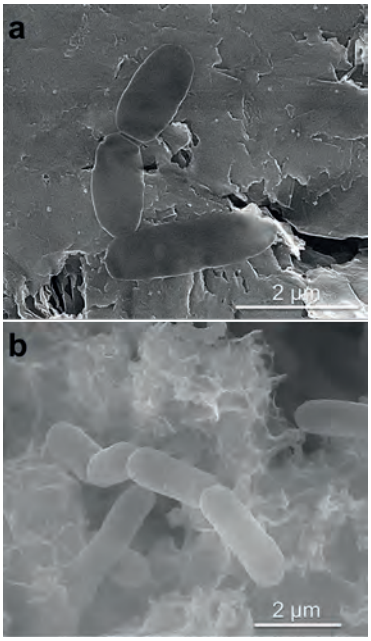

Fig. 1: *Environmental scanning electron micrographs of single cells of Desulfopila corrodens strain IS4. The advantage of graphite cathodes for electrochemical analysis can be seen in the comparison between cells of D. corrodens strain IS4 (a) directly attached to the surface of a graphite cathode and (b) cells attached to a sulfidic corrosion layer on top of an iron specimen.*

decomposition of iron by microorganisms is a major problem, much larger than one might think at first.

In a manner similar to atmospheric oxygen the corrosive microorganisms attack the iron, by using the energy contained in the iron as an energy source for their metabolism, leading to considerable damage of iron infrastructure [6, 7]. However, the basic mechanism by which the microorganisms consume the iron is not fully elucidated. Therefore, electron transfer processes at the electrode/microorganism interface of specialized sulfate-reducing bacteria and methanogenic archaea that are able to take up electrons directly from elemental iron, were characterized in a recent study [2]. In order to provide clear insights into electron transfer processes, electrochemical analysis of the highly corrosive microorganisms was performed in modified bioreactors with a three electrode setup operated with artificial seawater under anoxic conditions and complemented by chemical analysis and scanning electron microscopy (SEM) observations. Especially, direct coupling of precise electrochemical measurements in microbial cultures with chemical analysis like gas chromatography, clearly demonstrated the conversion of electrical energy into microbial end products within the modified bioreactor

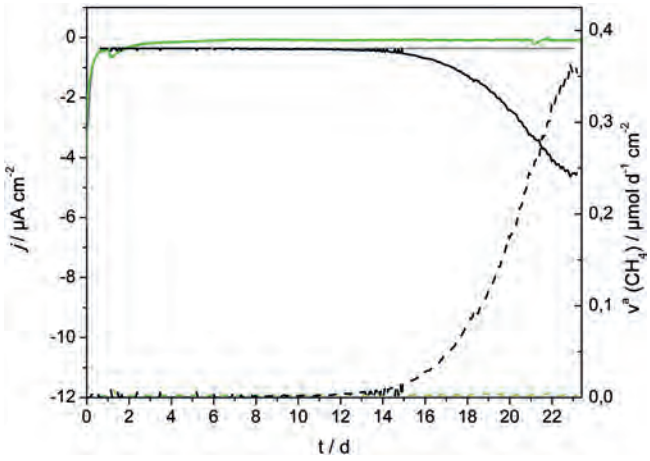

Fig. 2a: *Coupled potentiostatic measurements comparing current densities (solid line) and methane production rates (dashed line) in a sterile control (grey), a control culture (green) and a culture of strain IM1 (black), showing an efficiency of the bio-electrocatalytic process of nearly 80%.*

setup. Moreover, electrochemical monitoring of corrosion rates under those anoxic laboratory conditions for the first time proved that the rather novel electrochemical frequency modulation (EFM) method has a great potential for monitoring microbial corrosion due to the identification of localized corrosion, thereby assessing the accurateness of the obtained corrosion rates [1]. However, the extraordinary electron uptake mechanism of Desulfopila corrodens strain IS4 and the Methanobacterium-like archaeon strain IM_1 at the electrode/microorganism interface is not limited solely to taking up energy from iron surfaces, serving as the sole electron donor for microbial metabolism. Remarkably, the specialized microorganisms also grew on other conductive materials, such as graphite and germanium crystals, when exposed to appropri-

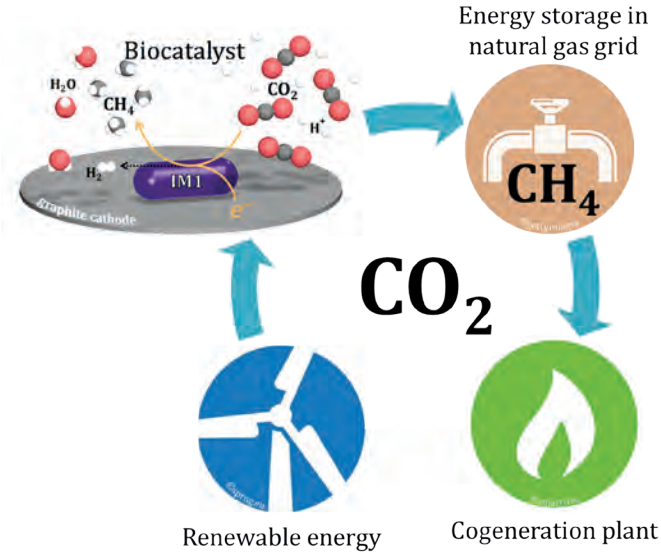

Fig. 2b: *Illustration of bioelectrical energy conversion of renewable energy. A lithoautotrophic archaeon selectively reduces carbon dioxide to methane on a graphite cathode, which can be stored in natural gas grids and reused in cogeneration plants on demand.*

ate power [3, 4]. Those materials for the first time enabled precise electrochemical and infrared spectroelectrochemical analysis of the electron transfer in pure cultures of corrosive microorganisms. Direct electron transfer in the absence of artificial electron mediators was achieved at a potential of -0.4 V vs. SHE. While for strain IM1 the redox active components associated with the outer cell surface are yet unknown, outer membrane c type cytochromes were identified to be involved in a direct electron uptake from reduced surfaces in strain IS4. Thus, strategies can be developed to inhibit the direct entry of electrons into the energy cycle of the microorganisms, preventing e.g. leakage of pipelines.

Moreover, electron uptake from electrodes by specialized microorganisms also is of great importance for an energy conversion process, in which the microorganisms, acting as so-called biocatalysts, convert electrical energy into chemical energy that either can be stored or used as a precursor in chemical production. The great advantage of biocatalysts is the high efficiency in energy conversion and an extraordinary selectivity for distinct conversion reactions, which often is not achieved by conventional catalysts. Coupled electrochemical measurements, especially in cultures of strain IM1, perfectly illustrated its production of methane by the reduction of carbon dioxide, which reached a coulombic efficiency of nearly 80 % at much lower voltages than observed with standard copper catalysts used in the chemical industry [3]. In addition, no other gaseous by-products are produced by those methanogenic archaea, whereby a complicated purification of the emitted biogas becomes unnecessary. Thus, an excess of renewable energy could efficiently be converted at peak times of electricity production into methane through bio electrocatalysis and be stored in an already existing natural gas network without the need of additional storage technologies. In a cogeneration plant the stored energy in the form of methane can thus be used on demand and thereby provides a first solution to the problem of fluctuating electricity production, using renewable energy technologies.

It is noteworthy that investigations of electron transfer processes at the electrode/microorganism interface thus have shown to be not only relevant for elucidating the destructive mechanism of microbial corrosion, but have also shown that this particular mechanism can be exploited for an efficient bioelectrical energy conversion, which is an impressive example of the complexity of bacterial activity and the diversity of bioelectrochemistry.

References

1. Beese, P., Venzlaff, H., Srinivasan, J., Garrelfs, J., Stratmann, M., Mayrhofer, K.J.J.: Electrochimica Acta (2013) 105, 239-247.
2. Beese-Vasbender, P.F.: From Microbially Induced Corrosion to Bioelectrical Energy Conversion - Electrochemical Characterization of Sulfate-Reducing Bacteria and Methanogenic Archaea. Ruhr Universität Bochum (2015).
3. Beese-Vasbender, P.F., Grote, J.-P., Garrelfs, J., Stratmann, M., Mayrhofer, K.J.J.: Bioelectrochemistry (2015)a 102, 50-55.
4. Beese-Vasbender, P.F., Nayak, S., Erbe, A., Stratmann, M., Mayrhofer, K.J.J.: Electrochimica Acta (2015)b 167, 321–329.
5. Enning, D., Garrelfs, J.:Appl. Environ. Microbiol. (2013) 80, 1226–1236.
6. Enning, D., Venzlaff, H., Garrelfs, J., Dinh, H.T., Meyer, V., Mayrhofer, K., Hassel, A.W., Stratmann, M., Widdel, F.: Environ. Microbiol. (2012) 14, 1772-1787.
7. Venzlaff, H., Enning, D., Srinivasan, J., Mayrhofer, K.J.J., Hassel, A.W., Widdel, F., Stratmann, M.: Corros. Sci. (2013) 66, 88-96.

Fracture Mechanics and Mechanisms at Small Length Scales

B.N. Jaya, R. Soler, C. Kirchlechner, S. Brinckmann, G. Dehm

Department of Structure and Nano-/Micromechanics of Materials (SN)

Micro-scale fracture testing has become an indispensable tool to track the fracture responses of miniaturized materials and devices as well as internal microstructure components with high local resolution [1]. In addition to individual phases in materials, grain boundaries and interfaces between dissimilar materials are in our research focus for downscaling and developing fracture methods with the aim to propose strategies to improve the fracture properties based on sound quantitative fracture data. Our objective is to use site-specific specimen preparation routes like the focused ion beam (FIB) or lithography techniques to machine fracture test specimen and load them using state of the art *in-situ* instrumentation inside the electron microscope to achieve nano-scale load-displacement resolutions and simultaneously visualization of crack propagation. Due to the restrictions imposed by small-specimen sizes vis à vis the microstructural heterogeneity involved, it is hard to find a universal technique applicable for all brittle systems at small-length scales.

The fracture test geometries are either modified versions of bulk fracture test methods or novel techniques [1]. In the absence of ASTM like standards, these are seen to result in a large scatter in KIC as a function of various extrinsic artifacts. In order to quantify the effect of several external factors like loading mode, ion beam damage and notch radius, high purity single crystalline Si without any microstructural complexity was chosen as the model system. We chose four micro-scale test geometries: single cantilever bending, clamped beam bending, double cantilever bending and pillar splitting on FIB-micromachined and FIB-notched specimens on a single wafer of (100) Si and tested them *in-situ* inside the scanning electron microscope (SEM) using a nano-indenter system (Fig 1). The average KIC was measured to be 0.80 $MPam^{1/2}$ with less than 15% variation across the different methods, which is also very close to the macro-scale known fracture toughness of Si [2]. Each test geometry offers certain distinct advantages and limitations [2] and the geometry most optimized for the system concerned is chosen to study the microstructure-fracture property correlation in other systems.

Having confirmed the reliability of the testing method, micro-cantilever bending was used to probe the fracture behaviour of ultra-high strength, heavily cold drawn 0.98 wt % C pearlitic steel wires showing limited ductility and cleavage fracture [3]. These are two-phase lamellar, nanocrystalline nano-composites of α-Fe and θ-Fe_3C used in bridge cables, piano strings and tire cords. Intrinsic length scales of 10-100 nm, and wire diameters of 40 to 150 µm necessitate micro-scale fracture experiments. Fracture tests carried out for drawing strains of 3, 4 and 5 revealed a sharp drop in KIC from 25 to 9 $MPam^{1/2}$ with increasing strain (Fig 2a), with values quite close to macro-scale tests of severely plastically deformed samples [4]. These drawing strains are of interest because they represent a transition regime, where the structure breaks down from a lamellar two-phase material to a nanocrystalline columnar structure of a tetragonal distorted α-Fe with the cementite decomposing and the excess C forced into solid solution of the distorted α-Fe and enriched at the grain boundaries [3]. Preliminary post-mortem analysis of the fracture process shows a mixture of trans-granular and inter-columnar boundary fracture (Fig 2b-c).

A bigger and more practical challenge is to gain insights into adhesion and interface fracture in multilayer thin film systems like those used in protective coatings or microelectronic devices. The role of interface strength within a matrix of brittle

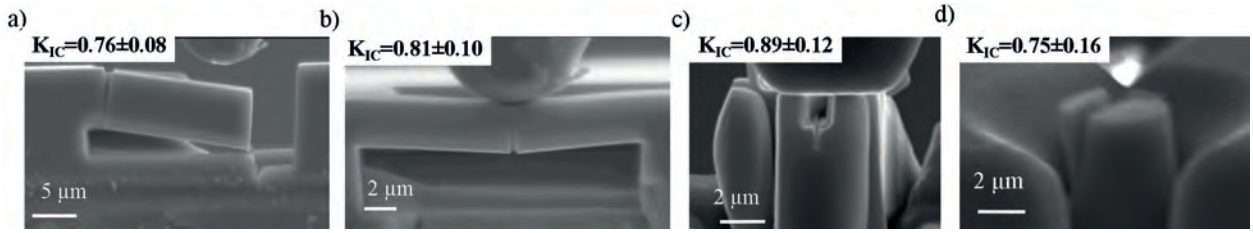

Fig. 1: *a)-d) Four micro-scale fracture geometries tested on Si (100) showing linear elastic deformation till final failure and the corresponding fracture toughness values.*

a)

Drawing strain (ε)	K_{IC} (MPam$^{1/2}$)	Type of fracture
3.2	25.7 (lower limit)	Elastic-plastic, stable
4.2	10.7±1.7	Linear elastic, slight deviation
5.2	9.0±1.5	Linear elastic, slight deviation

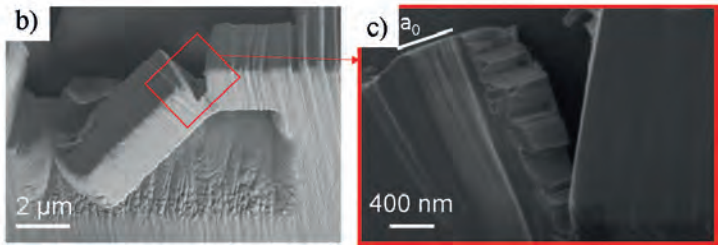

Fig. 2: *a) KIC from micro-cantilever fracture tests of cold drawn pearlitic steel wires as a function of drawing strain; b)-c) shows higher magnification images of the crack path and fracture surface.*

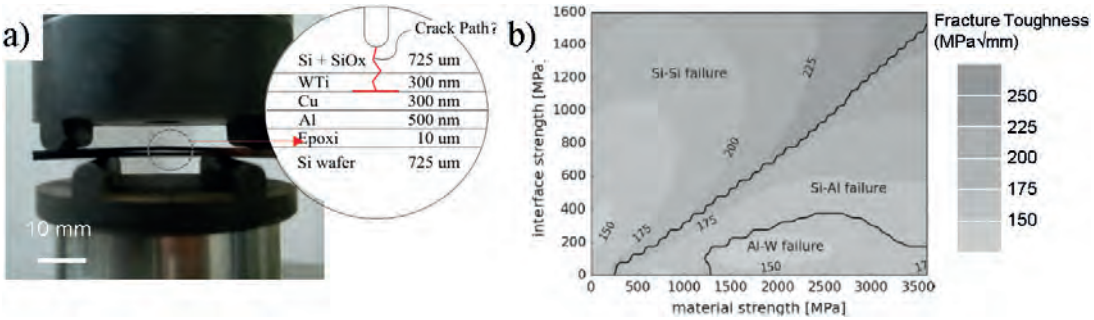

Fig. 3: *a) Four point bend fracture experiment on a MOSFET device containing multi-phase heterophase Si/SiOx/WTi/Cu/AlSiCu/Epoxy/Si interface; b) Interfacial fracture toughness map as a function of matrix and interface strengths.*

and ductile films of varying thickness (Si/SiOx/WTi/Cu/AlSiCu/Epoxy/Si) with multiple hetero-phase interfaces was examined using four point bending [5] in combination with finite element method (FEM) to evaluate the interfacial fracture energy and probability of failure (Fig 3). Results from FEM show that an optimal combination of a sufficiently weak interface architecture in a high strength matrix is beneficial for fracture toughness (Fig 3b) since it promotes crack kinking and branching and enhanced tortuosity [6]. Although common in natural materials like shell and wood, these predictions run counter-intuitive to the more common manufactured structures. FEM analysis is able to provide insights into the experimental observations in such complex scenarios, enabling lifetime predictions for multilayered systems. Currently, we are extending interface fracture experiments to a transmission electron microscope (TEM) level [7] building on our previous expertise for interface fracture testing performed at the micron-scale [8].

References

1. Jaya, B.N.; Jayaram, V.: J. Met. (2015) (available online).
2. Jaya, B.N.; Kirchlechner, C.; Dehm, G.: J. Mater. Res. 30 (2015) 686.
3. Li, Y.J.; Choi, P.; Goto, S.; Borchers, C.; Raabe, D.; Kirchheim, R.: Acta Mater. 60 (2012) 4005.
4. Hohenwarter, A.; Taylor, A.; Stock, R.; Pippan, R.: Metall. Mater. Trans. A 42 (2011) 1609.
5. Völker, B.; Venkatesan, S.; Heinz, W.; Matoy, K.; Roth, R.; Batke, J.M.; Cordill, M.J.; Dehm, G.: J. Mater. Res. 30 (2015) 1090.
6. Brinckmann, S.; Völker, B.; Dehm, G.: Int. J. Fracture. 190 (2014) 167.
7. Völker, B.; Heinz, W.; Roth, R.; Batke, J.M.; Cordill, M.J.; Dehm, G.: Surf. Coat. Technol. 270 (2015) 1.
8. Matoy, K.; Detzel, T.; Müller, M.; Motz, C.; Dehm, G.: Surf. Coat. Technol. 204 (2009) 878.

Origin of Anharmonicity in fcc Materials

A. Glensk, B. Grabowski, T. Hickel, J. Neugebauer

Department of Computational Materials Design (CM)

The quasiharmonic approximation is nowadays the workhorse for performing thermodynamic assessments at finite temperatures using *ab initio* methods. Going beyond the harmonic picture by including the full set of relevant high temperature excitations turns out to be a daunting task. In particular, anharmonic contributions due to phonon-phonon interactions are a challenge for first principles. They cannot be considered on a daily basis due to significant computational demands: In comparison to the quasiharmonic contribution, the computational workload usually increases by more than three orders of magnitude. For this reason, studies including anharmonic contributions are rare and it is generally unknown if and to what extent they influence thermodynamic material properties. This is unfortunate, since practically relevant physical quantities as e.g., phonon life times, thermal conductivity etc. are completely controlled by anharmonicity and can only be calculated by methods which fully capture these interactions.

Until recently, only a few selected test systems were assessed by first principles methods including anharmonic atomic vibrations [1, 2]. For defects it was shown that anharmonic contributions can introduce not only qualitative but even quantitative changes to thermodynamic properties [3]. To investigate similar effects on bulk systems, we have performed a wide range study including, in particular, phonon-phonon interactions [4]. Fig. 1 compares different finite temperature contributions - such as quasi-harmonic, electronic and anharmonic - to the specific heat capacity of the investigated elements. In contrast to common belief we have found that anharmonic contributions show the same order of magnitude as the usually considered quasiharmonic contributions and that neglecting them can significantly alter the thermodynamic assessment. They can easily change phase transition temperatures by several hundred Kelvin and, as in the case of silver, significantly influence the thermodynamic stability at elevated temperatures [4].

To understand the origin of the unexpectedly large anharmonic contribution, we carefully analyzed our molecular dynamics data. Comparing the distribution of nearest neighbour vectors between two atoms for a quasiharmonic run to a fully DFT (density functional theory) based (anharmonic) molecular dynamics run we made a critical observation, which is shown in Fig. 2. While the quasiharmonic distribution (left) is seen to be fully symmetric, the DFT based run shows a distinctly non-symmetric (anharmonic) and Morse like distribution, which cannot be captured by the typically applied quasiharmonic approximation.

In a consecutive step we were able to extract the anharmonic potential from a few displacements directly at T=0K without the necessity to resort

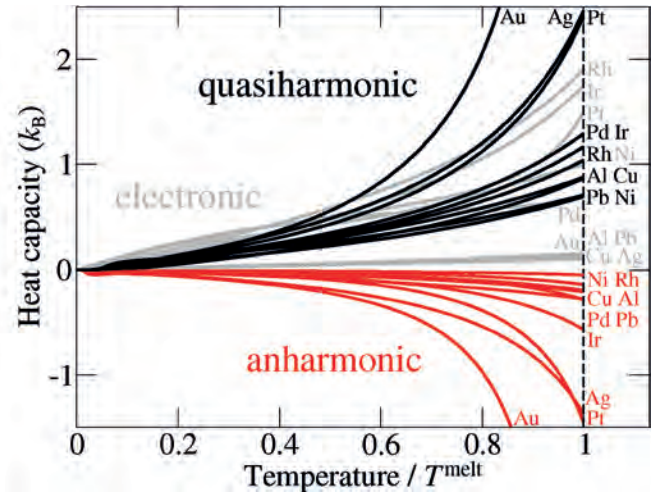

Fig. 1: *Quasiharmonic (qh), electronic (el) and anharmonic (ah) contribution to the specific heat capacity for the investigated elements as function of homologous temperature. Anharmonic contributions show the same order of magnitude as the generally considered contributions (qh and el) and their neglect can therefore significantly alter the thermodynamic assessment.*

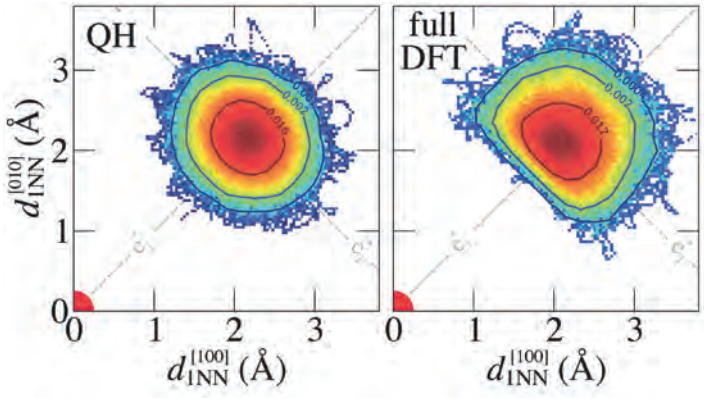

Fig. 2: *Results from a molecular dynamics (MD) run for silver at the melting temperature. For a quasiharmonic (QH, left) and a fully DFT-based potential (right), the vector between two neighbouring atoms is shown for every time step of the MD run. While the QH distribution is fully symmetric, the fully DFT based MD shows a pronounced anharmonic distribution due to Pauli repulsion. The true non-symmetric behaviour cannot be represented by a purely harmonic potential.*

to demanding molecular dynamic calculations. In particular, this was done by significantly extending the displacement range of the quasiharmonic approximation. With this we obtained a local anharmonic Hamiltonian that give rise to a new method referred to as the Local Anharmonic (LA) approximation.

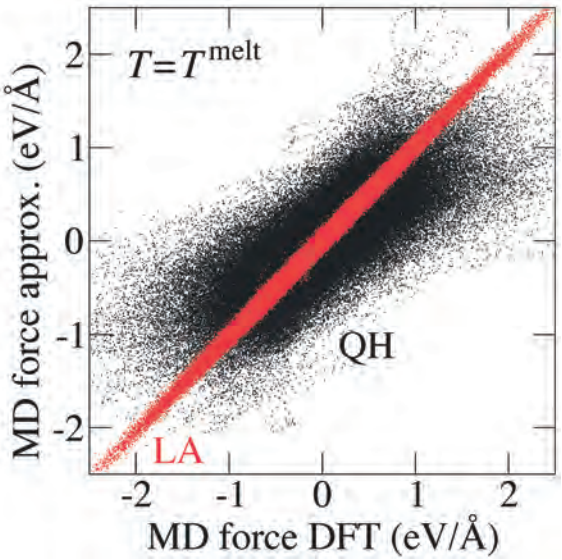

Fig. 3: *Comparison of QH (black) and LA (red) forces to fully DFT-based forces.*

Fig. 3 compares the forces of the LA (red) and the typically used QH approximation (black) to fully DFT based forces for a molecular dynamics run of Ag at the corresponding melting temperature. The LA forces are seen to significantly outperform the corresponding QH forces also for all other investigated elements (not shown). Moreover, we found that anharmonic free energies in the LA approximation deviate only by maximally 6 meV/atom at the melting point for the investigated elements in comparison to numerically exact DFT results (27 meV/atom for QH). Using the LA Hamiltonian as a reference potential for thermodynamic integration resulted in a typical speed up of two orders of magnitude in comparison to the QH reference. This opens the path towards routine, numerically exact *ab initio* free energies. First assessments of phonon line widths using the LA approach seem very promising and are currently investigated in detail.

References

1. Vacadlo, L.; Alfe, D.: Phys. Rev. B 65 (2002) 214105.
2. Grabowski, B.; Ismer, L.; Hickel, T.; Neugebauer, J.: Phys. Rev. B 79 (2009) 134106.
3. Glensk, A.; Grabowski, B.; Hickel, T.; Neugebauer, J.: Phys. Rev. X 4 (2014) 011018.
4. Glensk, A.; Grabowski, B.; Hickel, T.; Neugebauer, J.: Phys. Rev. Lett. 114 (2015) 195901.

Grain Boundary Embrittlement in Fe-Mn Alloys

M. Kuzmina [1], D. Ponge [1], I. Bleskov [2], T. Hickel [2], D. Raabe [1]

[1]Department of Microstructure Physics and Alloy Design (MA)
[2]Department of Computational Materials (CM)

Medium manganese steels are binary base model alloys for a third generation of high strength steels [1]. Excellent mechanical properties are mostly related to the TRIP effect, which arises due to the presence of reverted austenite in the microstructure. Unfortunately, these alloys are brittle in the compositional range of interest between 5 to 12 at% Mn [2 - 4]. This embrittlement becomes particularly pronounced in the impact toughness test even at room temperature. Fig. 1 shows that even a tempering treatment as short as 10 s is sufficient to embrittle prior austenite grain boundaries (PAGBs).

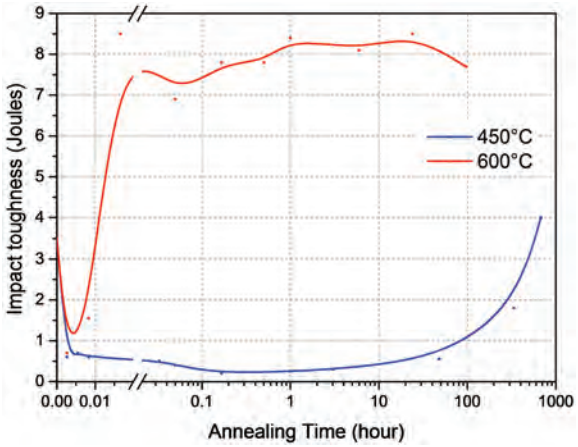

Fig. 1: *Fe-9wt%Mn, Impact toughness at room temperature after tempering at 450 °C and 600 °C and subsequent quenching.*

Segregation induced grain boundary (GB) embrittlement is a common reason for a decrease of grain boundary cohesion. To analyse the segregation on an atomic level atom probe tomography (APT) was applied on site specifically FIB (Focused Ion Beam) prepared PAGBs after different heat treatments. Atom distribution maps and corresponding concentration profile is plotted in Fig. 2 for an embrittled case after a short tempering at 450 °C. The increase of Mn concentration without a significant change in concentration of other elements indicates that Mn segregation can be associated with the temper embrittlement.

In order to get an unambiguous proof for the Mn effect on GB embrittlement, further APT measurements of GB chemistry in de-embrittled state after long tempering times were performed. For an evaluation of PAGB concentrations GB excess values were extracted and plotted in Fig. 3. A rapid increase in Mn excess value after tempering at 450 °C is followed by a decrease after prolonged tempering time. The Mn excess value curve has an excellent correlation to the impact toughness values: thus a GB embrittlement is caused by an increase of a Mn excess value and a further improvement of impact toughness corresponds with a decrease of the Mn excess values. This decrease of Mn excess value is attributed to a formation of Mn-rich austenite phase on GBs and consumption of Mn from the GBs, hence cleaning them from Mn segregation.

In order to understand the underlying mechanisms for Mn induced GB embrittlement, *ab initio*

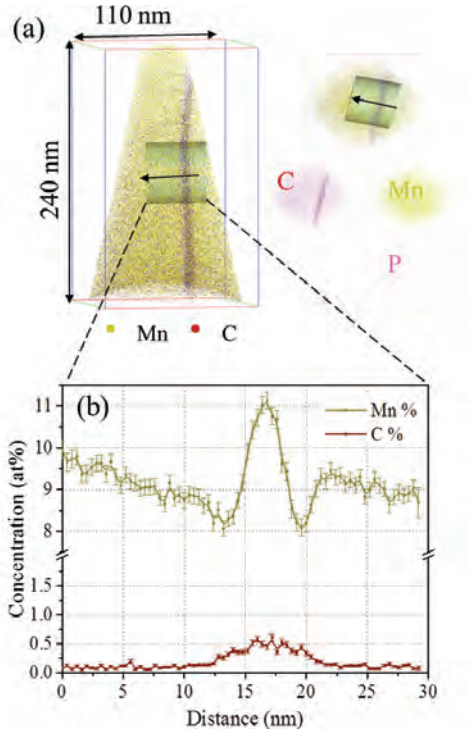

Fig. 2: *(a) APT results obtained on Fe-9wt% Mn tempered at 450 °C for 1 min. 3D side view and top view of the dataset of the same region, with the corresponding element distribution maps revealing the accumulation of C, Mn on the PAGB and a homogeneous distribution of P; a corresponding 1D concentration profile (b) shows enrichment of C and Mn atoms.*

calculations based on density functional theory as implemented in the Vienna *ab initio* simulation package (VASP) have been performed. In a two-step approach, we first analyzed the behaviour of Mn in bcc Fe, considering supercells of 54 atoms. To model in a second step the Mn segregation at grain boundaries, the ∑5(013) GB has been simulated in a 120 atoms supercell. This is a tilt GB constructed

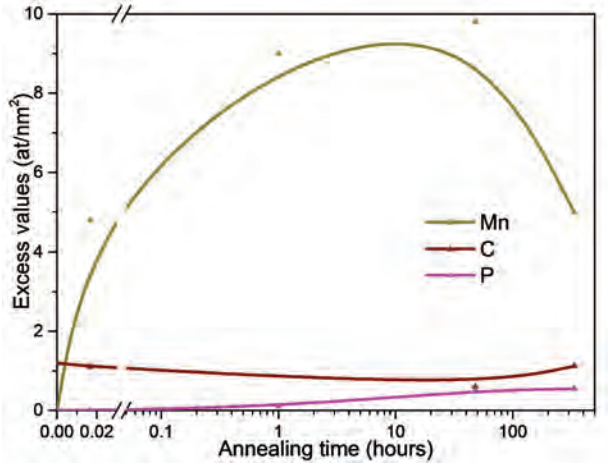

Fig. 3: *An evolution of manganese, carbon and phosphorous grain boundary excess values after tempering at 450 °C.*

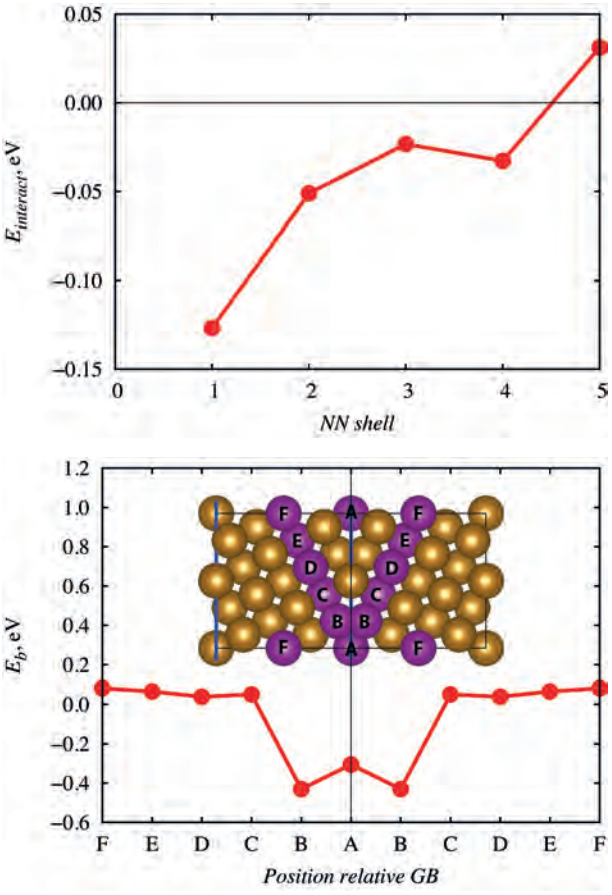

Fig. 4: *(a) Effective interaction energy between two Mn interstitials in bcc Fe as a function of their separation and (b) Segregation energy of Mn interstitial as a function of distance from the boundary plane (the insert shows the structure of the symmetrical ∑5(013) grain boundary).*

using the coincidence site lattice (CSL) approach by rotating two bcc lattices by 36.9° around the [100] direction, see Fig. 4.

The calculations with one Mn solute atom in bulk ferromagnetic (FM) bcc Fe revealed the preference for Mn to have a local magnetic moment antiparallel to those of the surrounding Fe atoms. A clustering of Mn atoms could therefore be stabilized by a change of the magnetic ordering to an antiferromagnetic (AFM) configuration. An effective interaction energy depending on the distance d between two Mn atoms, $E_{interact}(d) = (E_{Mn+Mn}(d) + E_{bcc}) - (E_{Mn} + E_{Mn})$, characterizes the solute-solute interaction in a bcc supercell. Here, the total energy of the cell containing two substitutional Mn atoms (E_{Mn+Mn}) is compared to those of supercells without Mn (E_{bcc}) and with one Mn atom (E_{Mn}). From Fig. 4a one can see that Mn has local clustering tendency in bcc Fe ($E_{interact} < 0$) at 0K (compare [5]).

The tendency for the individual Mn atoms to segregate at a grain boundary is described by the binding energy: $E_b = (E_{Mn+GB} + E_{bcc}) - (E_{GB} + E_{Mn})$, where E_{Mn+GB} and E_{GB} are the total energies of the supercells containing grain boundaries with and without a Mn atom, respectively. A negative value of E_b indicates an attraction of the solute atom to the GB. From Fig. 4b one can see that Mn atoms prefer position B (see insert in Fig. 4b) - not exactly at the GB but the atomic sites nearest to the boundary plane.

Thus, the observations obtained so far by our zero K calculations indicate that the following mechanisms could support the grain boundary embrittlement: Firstly, Mn has a tendency to segregate near the GB. Secondly, the attractive interaction between Mn atoms in bcc Fe supports the clustering of Mn atoms in this region. Thirdly, the antiferromagnetic interaction of the Mn atom will yield a change of the magnetic ordering where Mn clustering occurs. It is known also that AFM lattice constant differs from that of FM state. Therefore, Mn segregations on grain boundaries may serve as strain concentrators in medium-Mn steels.

References

1. Cao W., Wang C., Wang C., Shi J., Wang M., Dong H., Weng Y.: Sci China Technol Sci (2012) 55,1814.
2. Kuzmina M., Ponge D., Raabe D.: Acta Mater (2015) 86, 182.
3. Nasim M., Edwards B.C., Wilson E.A.: Mater Sci Eng A (2000) 281,56.
4. Heo N.H., Heo Y.-U., Kim S.-J., Nam J.W. : Acta Mater (2013) 61,4022.
5. Olsson P., Klaver T.P.C., Domain C., Physical Review B (2010) 81, 054102.

Impact of Anharmonicity and Nonlocal Many-Body Effects on the Thermodynamics of Au

B. Grabowski [1], S. Wippermann [2], A. Glensk [1], T. Hickel [1], J. Neugebauer [1]

[1]Department of Computational Materials Design (CM)
[2]Department of Interface Chemistry and Surface Engineering (GO)

Theoretical efforts at the MPIE over the past years have provided various techniques for computing thermodynamic properties from *ab initio*, thereby greatly contributing to our understanding of finite temperature materials properties. Mostly, these developments were based on standard approximations to the exchange-correlation functional within density-functional-theory (DFT). For a wide range of materials these approximations provide an excellent description of finite temperature properties up to the melting point as the CM has shown previously (see p. 46). However, standard functionals are known to have intrinsic deficiencies, e.g. for elements with nearly full electron shells such as Au. In fact, the heat capacity of Au computed within the generalized gradient approximation (GGA) shows even a diverging behaviour, well below the experimental melting temperature regardless of whether anharmonicity is included or not (orange solid and dashed grey line in Fig. 1).

In collaboration with Dr. Stefan Wippermann (GO), we have recently extended our previous thermodynamic approaches allowing now to compute finite temperature properties, in particular anharmonicity, at a level beyond the standard approximations [1]. For that purpose, we have coupled the upsampled thermodynamic integration using Langevin dynamics (UP-TILD) method [2] with the random phase approximation (RPA) employing the adiabatic-connection-fluctuation-dissipation theorem [3]. This new RPA UP-TILD technique allows to investigate the impact of nonlocal many-body effects on thermodynamic properties, and for Au we could show that the severe discrepancies introduced by the standard functionals disappear (green line in Fig. 1) and that an excellent agreement with experiment is obtained (black dots).

The crucial challenge in developing the RPA UP-TILD method was to overcome the prohibitive computational workload which would arise if the RPA technique was coupled directly to state-of-the-art molecular dynamics simulations. To this end, we followed a perturbative strategy as in the original UP-TILD method. In particular, within RPA UP-TILD, we utilize a molecular dynamics simulation performed within standard DFT, e.g. using GGA, to obtain a phase-space sampling at the desired volume and temperature. We then extract a few uncorrelated snapshots and calculate the RPA UP-TILD energy as

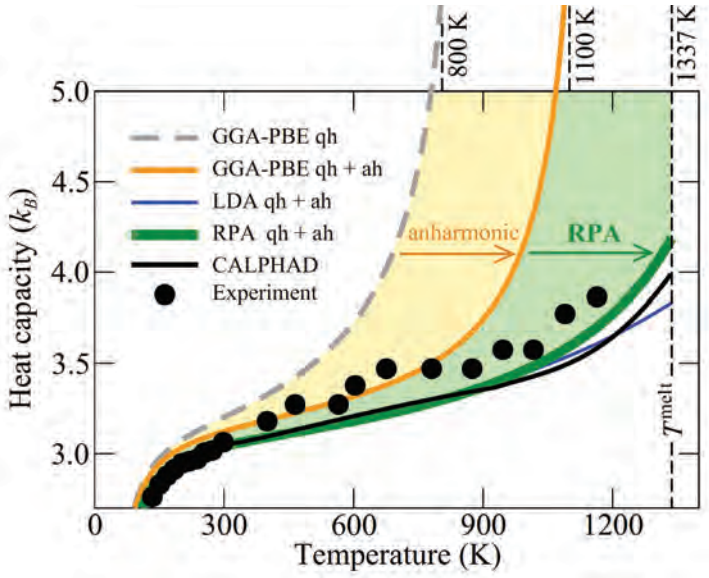

Fig. 1: *Application of the new RPA UP-TILD method to Au. Using the generalized-gradient-approximation (GGA) a diverging heat capacity is obtained, regardless of whether the standard quasiharmonic (qh) approach is used (grey dashed line) or the state-of-the-art extension to anharmonic (ah) contributions (orange solid line). It is only upon application of the newly developed RPA UP-TILD method (green solid line) that a good agreement with experiment (filled circles, Ref. [4]) is obtained. Figure adapted from Ref. [1].*

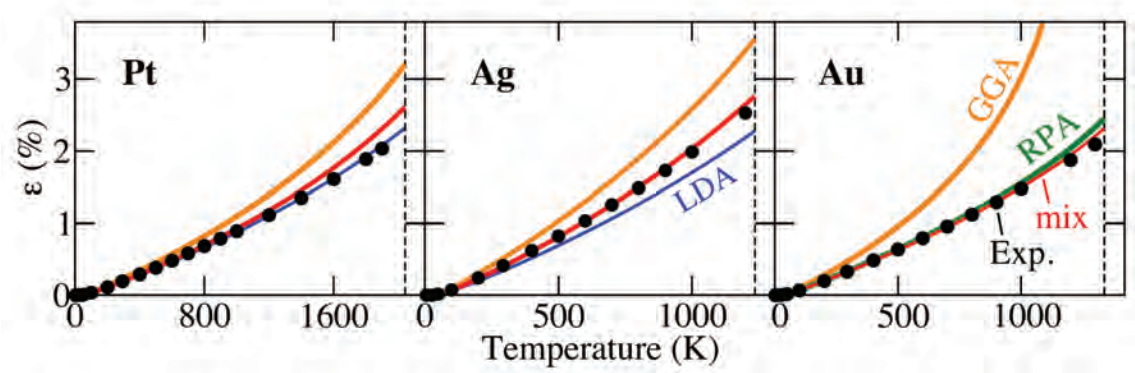

Fig. 2: *Linear thermal expansion calculated within GGA (orange lines; including anharmonicity), fully within RPA obtained with the here introduced RPA UP-TILD method (green line; Au only), and using a mixed approach (red lines) employing the T = 0 K RPA curve in conjunction with GGA-PBE finite temperature excitations. Experimental values (solid circles) are from Ref. [8].*

a difference between the GGA and RPA energies of the corresponding supercell. Adding this difference to the T=0 K RPA energy and to the GGA vibrational free energy, we obtain the total free energy with an accuracy of the RPA method.

A strength of the developed RPA UP-TILD methodology is that the different contributions can be investigated separately. Our analysis has shown that the strong impact of RPA (green shaded region in Fig. 1) originates mainly from differences in the T = 0 K energy-volume curves and corresponding values for the equilibrium lattice constant and bulk modulus. The GGA values (4.15 Angstrom and 140 GPa) are substantially modified by the RPA (4.10 Angstrom and 175 GPa) giving rise to a considerably stiffer bulk. This stiffness is the factor responsible for shifting the divergence in the thermodynamic quantities beyond the experimental melting point.

Utilizing this insight, we have proposed an efficient approach to compute accurate finite temperature properties beyond standard DFT. The approach combines T = 0 K RPA energies with entropic contributions from standard exchange-correlation functionals such as GGA. Applying this approach, we obtained, with little computational effort, RPA finite temperature results for Ag and Pt, the elements showing the largest discrepancies within GGA except for Au [5]. As shown by the red lines in Fig. 2, the mixed approach provides excellent agreement with experiment for all studied elements and with full RPA for Au. This indicates that nonlocal many-body effects as captured by RPA affect predominantly the absolute binding energies at T = 0 K, while thermal vibrations are unaffected to a good approximation.

The insensitivity of high-temperature vibrations to nonlocal many-body effects is remarkable since recent studies [6] showed that close to melting the displacement of atoms from their equilibrium positions is significant and that the first-neighbour distance distribution is strongly affected by anharmonicity. Knowing that the GGA deficiency is not related to thermal vibrations but rather to the T = 0 K energy surface indicates a possible route for the development of accurate *ab initio* databases. T = 0 K computations are generally efficient since small supercells for single (or at most a few) atomic configurations are sufficient. It becomes therefore possible to employ computationally elaborate alternatives, such as the RPA technique employed here, to supplement the databases.

The introduced technique is not restricted to a combination of standard DFT with RPA. Any other higher level approach (e.g., quantum Monte Carlo [7]) can be coupled to standard DFT and used to obtain the accurate energies for the UP-TILD instead of the RPA.

References

1. B. Grabowski, S. Wippermann, A. Glensk, T. Hickel and J. Neugebauer: Phys. Rev. B (2015) 91 (20), 201103.
2. B. Grabowski, L. Ismer, T. Hickel and J. Neugebauer: Phys. Rev. B (2009) 79 (13), 134106.
3. D. Langreth and J. Perdew: Phys. Rev. B (1977) 15, 2884.
4. Y. S. Touloukian and E. H. Buyco: TPRC Data Series Vol. 4 (IFI/Plenum, New York, 1970).
5. T. Hickel, B. Grabowski, F. Körmann, and J. Neugebauer: J. Phys. Condens. Matter (2012) 24, 053202.
6. A. Glensk, B. Grabowski, T. Hickel, and J. Neugebauer: Phys. Rev. Lett. (2015) 114, 195901.
7. R. Q. Hood, P. R. C. Kent, and F. A. Reboredo: Phys. Rev. B (2012) 85, 134109.
8. Y. S. Touloukian, R. K. Kirby, R. E. Taylor, and P. D. Desai: TPRC Data Series Vol. 12 (IFI/Plenum, New York, 1975).

Magnon-Phonon Coupling at Arbitrary Finite Temperatures

F. Körmann, B. Grabowski, B. Dutta, B. Alling, T. Hickel, J. Neugebauer

Department of Computational Materials Design (CM)

An understanding of the mutual interaction between different temperature-induced excitations in solids is a pivotal challenge for the simulation of thermodynamic properties of many materials [1-3]. A particularly important interaction is the interplay between magnetic and atomic degrees of freedom, building the basis for many methodological applications [1]. For Fe-based materials, it is well known that magneto-elastic effects are of tremendous importance for the interpretation of various phenomena such as the Invar effect, diffusion processes, dislocation dynamics, and phase stabilities [1-3].

Density functional theory in principle provides access to interatomic forces, spin-polarized energetics, and their interactions. Force-constant calculations and spin simulations have been performed for decades. However, most studies have been restricted to separate investigations of the two effects, whereas their mutual coupling could only be addressed in recent years [1-4]. The T=0 K limit of a ferromagnetic system like Fe is the most straightforward case since calculating force constants for a single magnetic configuration with all spins pointing in the same direction is sufficient ("FM limit" in Fig.1). The infinite-temperature limit of a paramagnetic system with fully disordered spins ("PM limit") is significantly more challenging due to the large magnetic phase space that needs to be sampled for an accurate prediction of the coupling. Significant progress has been made only very recently with techniques based on, e.g., the disordered local moment molecular dynamics (DLM-MD) or the spin-space averaging procedure (SSA) [3,4].

At high temperatures, the DLM-MD and the SSA have both been equally successfully applied to describe phase stabilities in complex alloys such as recently shown for instance on the industrially important CrN system [3,4]. However, given the complexity of the problem, current methods are accurate only at very low temperatures, where significant long-range order is present, and at very high temperatures, where the system has lost all order in the spin arrangement. Intermediate temperatures are not directly accessible by explicit DFT calculations as prohibitively many large supercells would be needed to properly capture the partially destroyed long-range order and the inhomogeneously scattered regions with short-range order.

We therefore developed and applied a method that employs a set of DFT calculations carried out for only the FM and PM limits in conjunction with quantum Monte Carlo sampling (see e.g. [1]) to obtain properties at intermediate temperatures. The method is capable of describing magnon-phonon coupling at arbitrary finite temperatures, closing the previous simulation gap between the T=0 K and high-temperature limits. The performance of the method is demonstrated in Fig. 2, wherethe calculated temperature dependence of the phonon frequencies in bcc Fe is compared with experimental measurements (filled black squares in Fig. 2). The approach has been further validated by a new set of phonon frequencies measured at 38 temperatures (open circles in Fig. 2) by our experimental collaborators at the Advanced Phonon Source in Argonne [5]. The excellent agreement

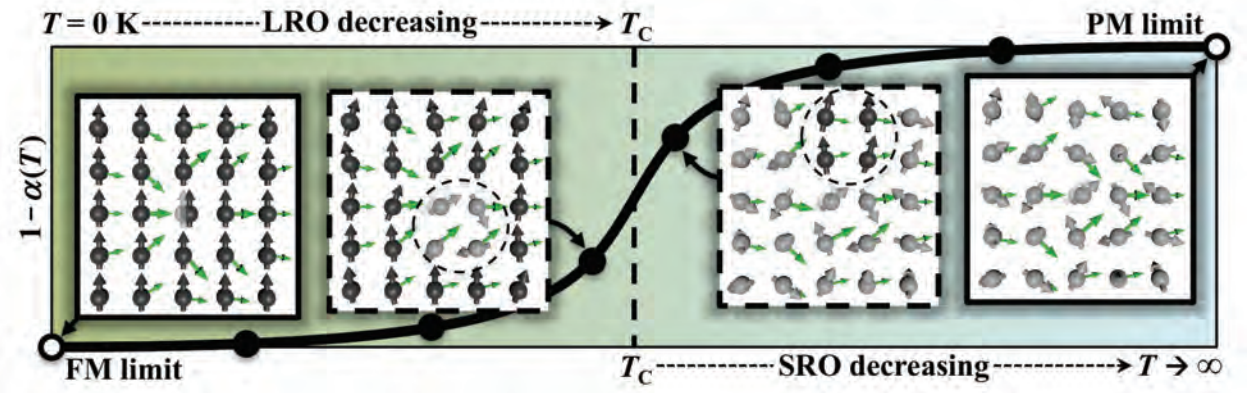

Fig. 1: *Sketch of the developed method coupling the energetics of the magnetic system with explicit DFT force constant calculations (displaced spin in the middle of each sketch). The gray and green arrows indicate the local magnetic spins for each atom and the interatomic forces (restoring forces when displacing the center atom) respectively. The explicit force constant calculations are carried out for the two limits of completely ordered (left side) and fully disordered spins (right side). The force constants for the intermediate temperature regime (dashed squares) are obtained by coupling the two limits with quantum Monte Carlo simulations for the magnetic subsystem which explicitly include long- and short-range-order effects.*

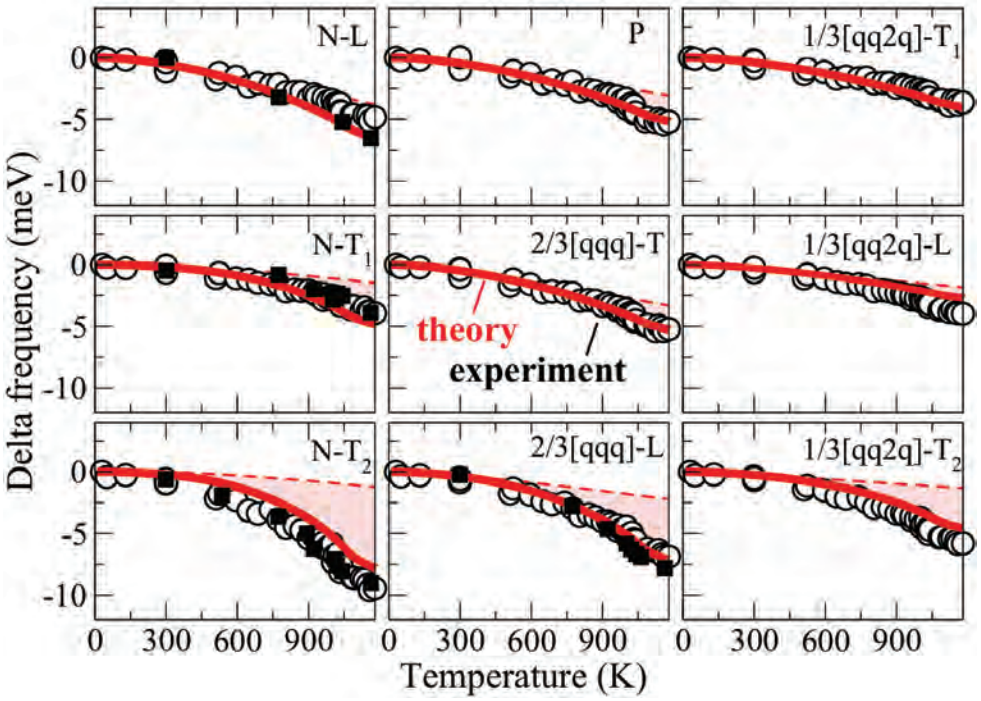

Fig. 2: *Temperature dependence of phonon frequencies for different modes comparing theoretical (solid red lines) with experimentally deduced frequencies (open circles). Dashed red lines show the ferromagnetic quasiharmonic results (no phonon-magnon coupling). Where available, previous neutron scattering data are included (filled black squares).*

between theory and experiments provided new insights into the role of magnon-phonon contributions for the thermodynamic stability of iron.

Going from elemental iron towards more complex Fe-based alloys, coupled chemical and magnetic order-disorder transitions need to be simultaneously taken into account. For this reason we have recently extended the SSA method by constructing chemical and magnetic random supercells, and performing complementary magnetic Quantum Monte Carlo simulations. The application to Fe-based Invar alloys shows indeed a similar agreement for temperature-dependent atomic excitations with experimental data as obtained for pure iron [6].

A present challenge for the DLM-MD and SSA techniques is still the inclusion of the so-called longitudinal magnetic degree of freedom (i.e. the variation of the magnitude of local magnetic moments) and particular its coupling to the atomic motion. On the one hand, for magnetic systems such as iron, which show rather "robust" local magnetic moments, atomic vibrations still impact the longitudinal spin degree of freedom by distorting local atomic geometries at high temperature. One effect is the induction of a spatial variation of local moments and a temperature dependence of their mean value. This is currently being investigated by employing the DLM-MD for paramagnetic gamma and delta iron [7]. On the other hand, for magnetic systems known for strong local moment fluctuations such as, e.g., Nickel, we have further extended the SSA by combining it with constrained spin DFT [8].

The complementary developed techniques allow us thus to investigate phonon-magnon contributions for a large class of magnetic systems, ranging from weak to strong ferromagnets as well as from elemental magnets to complex magnetic alloys. We anticipate that their future unification will allow quantitative modeling of the stability and properties of magnetic materials for temperatures ranging from 0 K up to the melting point.

References

1. Körmann, Hickel, Neugebauer: Curr. Opin. Solid. St. M. (2015), doi:10.1016/j.cossms.2015.06.001, *in press.*
2. Körmann, Breidi, Dudarev, Dupin, Ghosh, Hickel, Korzhavyi, Munoz, Ohnuma: Phys. Status Solidi B (2014) 251, 53.
3. Abrikosov, Ponomareva, Steneteg, Barannikova, Alling, Curr. Opin. Solid. St. M. (2015), doi:10.1016/j.cossms.2015.07.003, *in press.*
4. Zhou, Körmann, Holec, Bartosik, Grabowski, Neugebauer, Mayrhofer: Phys. Rev. B (2014) 90, 184102.
5. Körmann, Grabowski, Dutta, Hickel, Mauger, Fultz, Neugebauer, Phys. Rev. Lett. (2014) 113, 165503.
6. Ikeda, Körmann, Seko, Togo, Neugebauer, Tanaka: Phys. Rev. B, *in preparation*.
7. Alling, Grabowski, Körmann, Glensk, Abrikosov, Neugebauer: Physical Review B, *in preparation*.
8. Körmann, Ma, Dudarev, Neugebauer: J. Phys. Condens. Matter, *submitted*.

Tribology across the Length-Scales

S. Brinckmann [1], D. Mercier [2], F. Roters [2], R. Spatschek [3], M. Valtiner [4]

[1] Department of Structure and Micro-/Nanomechanics of Materials (SN)
[2] Department of Microstructure Physics and Alloy Design (MA)
[3] Department of Computational Materials Design (CM)
[4] Department of Interface Chemistry and Surface Engineering (GO)

Tribology occurs in almost all applications of metals when two surfaces get into contact. Friction and wear occur on multiple hierarchical length-scales, on each of which different mechanisms interact. On the macroscopic length-scale, the dynamics of elasticity and friction are investigated. We study plasticity, crack formation and surface roughness evolution on the micrometer length-scale. Friction and irreversible atomistic processes are researched on the nanometer scale.

On the atomistic length-scale at the surface, tribological processes in aqueous and corrosive environments are studied. The central crosslinking aim of this work is to understand the multiscale nature of wear and friction by upscaling from the nanometer to the micrometer length-scale. Therefore, friction experiments are performed with both atom force microscopy (AFM) and surface force apparatus (SFA) at the nanoscale. During single-stroke scratching in the nano-Newton regime, no irreversibility is visible at the given scale, as shown in Fig. 1.

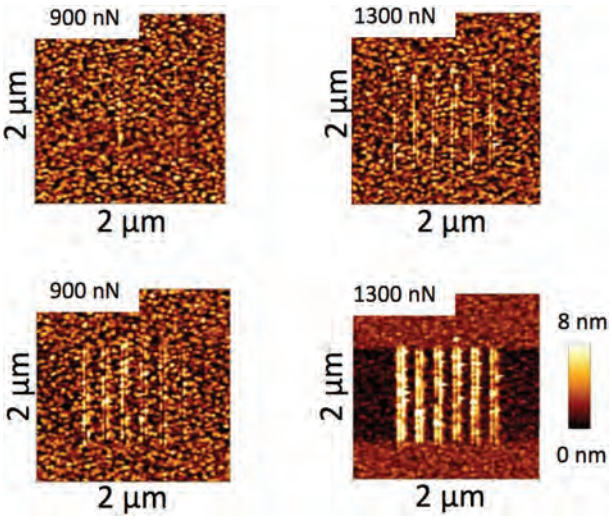

Fig. 1: *Top row: nanoscopic single stroke scratch tests with an atomic force microscope (AFM) at 900 nN and 1300 nN applied normal force. Bottom row: 10 stroke scratch tests reveal critical damage onset on the nanoscale. The vertical scale is identical in all images.*

However, when repeating the strokes, damage and the scratch tracks become visible. These dry friction and wear measurements are combined with studying the molecular structuring of lubricants in both aqueous and non-aqueous lubricants. In particular, on the material surface interfacial structuring of lubricant molecules (electric double layers, layering of lubricants are measured at the atomistic scale in order to correlate lubricant structuring and material properties with friction and wear performance. Combining these efforts with the complementary set of experiments in the other departments will pave the road for understanding friction and, in particular, wear and damage over all length scales.

Even polished surfaces have a microstructural roughness that leads to the microasperity contact when engineering surfaces get into contact. In the experiments, the nanoindenter with lateral force measurement is used to mimic friction and wear of a single microasperity. To this end, a hard spherical tip is scratched through the bulk metal and the plasticity on the track sides and in front of the scratch is investigated. The crystal orientation plays the dominant role in determining the slip pattern around the scratch track and the development of surface roughness. Grain boundaries act as partial obstacles to the transfer of plasticity: a subset of the plasticity causing dislocations is blocked at the grain boundary while the other dislocations penetrate the grain boundary. The massive dislocation plasticity at the surface ahead of the microasperity results in the formation of subsequent surface roughness and finally crack formation in the scratch track. The stress state in the scratch track is three-dimensional and results in mixed mode crack growth.

On the micrometer length-scale, crystal plasticity simulations with the DAMASK toolkit are used to further the understanding of plasticity around microasperities. The three dimensional stress state around the dynamic asperity is influenced by the crystal orientation and anisotropy of the material. Moreover, the proximity of grain boundaries restricts the plasticity. Hence, Finite Element Simulations of the crystal plasticity are warranted that take into account the contact of asperity and surface and evolve the contact as the asperity moves along the surface. To this end, the indentation and then horizontal movement of an infinitely hard sphere through an austenite counter material is simulated and the height-profile around the asperity is plotted. The severe plastic deformation around the asperity shows distinct differences when scratching in grains of different orientation and these slip surface patterns are similar to the experimental results: severe plasticity occurs around scratches in [111] oriented grains, as shown in Figs. 2 and 3.

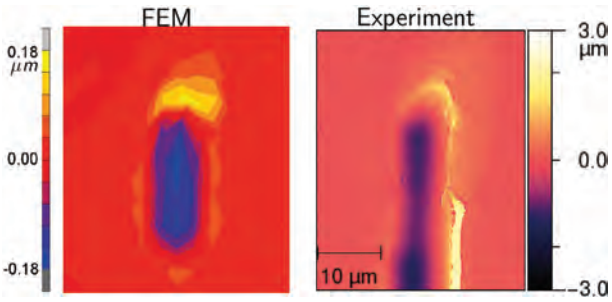

Fig. 2: *Qualitative comparison of crystal plasticity finite element (FEM) simulations and experiments on the microscale. The pile-ups ahead of the scratch are tilted slightly to the right-hand side. The height profile is shown in both images for an austenite grain with a surface normal close to the [111] orientation. Because of differences in length-scale, differences in the height occur.*

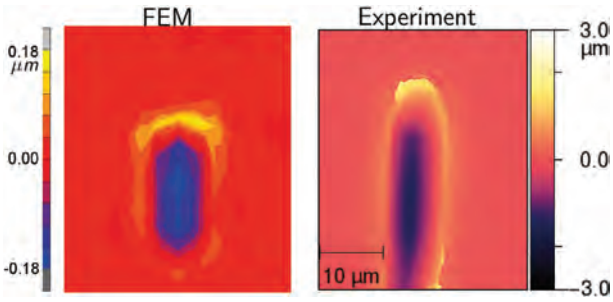

Fig. 3: *Qualitative comparison of FEM simulations and confocal measurements of a scratch in an austenite grain close to the [101] normal orientation. The pile-ups ahead of the scratch are almost straight and have a short extension. Differences in the height occur because of differences in length-scale and differences in scratch depth.*

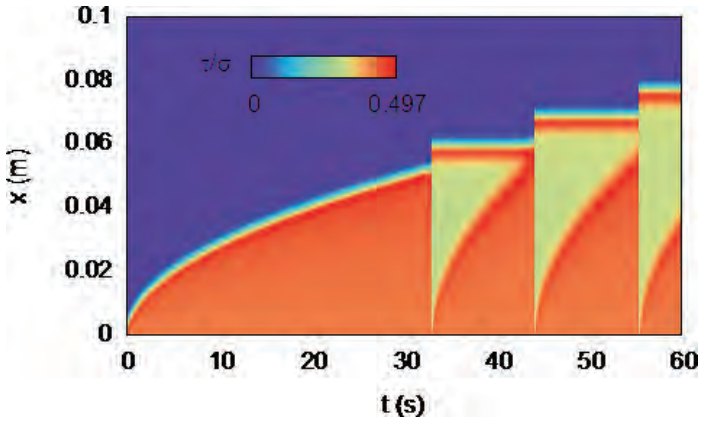

Fig. 4: *Space-time plot of the frictional stress at the contact surface between a rigid substrate and a slider. The red parabolic region corresponds to the slow propagation of a creep patch, which then repeatedly triggers "fast" events. The inset shows the slow-motion view with a detachment front velocity of only 3.3 m/s, which is much lower than the shear wave speed.*

Irreversible effects on the microcontact level during dry surface sliding contribute to the microasperity ageing. This aging microcontacts lead to velocity weakening of the macroscopic dynamic friction coefficient as function of sliding velocity. Rheological and chemical effects, in turn, favor the opposite effect of velocity strengthening [1]. The combination of velocity weakening and strengthening lead to minima of the frictional force as function of velocity, as we have shown recently in an extended survey of experimental data [2]. Near this minimum "stick-slip" pulses can propagate with velocities orders of magnitude lower than the speed of sound [3], which is a potential explanation for laboratory and geological observations of "slow earthquakes", as shown in Fig. 4. These slow propagation waves are emitted from creep patches, which are localized weakening precursors at the interface under shear, which become unstable after a certain propagation distance and trigger detachment front propagation [4].

References

1. Brener, E.A.; Weikamp, M.; Spatschek, R.; Bar-Sinai, Y.; Bouchbinder E.: "Dynamic instabilities of frictional sliding at a bimaterial interface", *submitted* for publication (arXiv: 1507.00156).
2. Bar-Sinai, Y.; Spatschek, R.; Brener, E.A.; Bouchbinder, E.: J. Geophys. Res.: Sol. Earth 119 (2014) 1738.
3. Bar-Sinai, Y.; Spatschek, R.; Brener, E.A.; Bouchbinder, E.: Sci. Rep. 5 (2015) 7841.
4. Bar-Sinai, Y.; Spatschek, R.; Brener, E.A.; Bouchbinder, E.: Phys. Rev. E 88 (2013) 060403.

Linear and Planar Complexions: Confined Chemical and Structural States in Steels

M. Kuzmina [1], M. Herbig [1], D. Ponge [1], S. Sandlöbes [1], D. Raabe [1], G. Leyson [2], B. Grabowski [2], J. Neugebauer [2]

[1]Department of Microstructure Physics and Alloy Design (MA)
[2]Department of Computational Materials Design (CM)

Medium manganese steels are of high scientific and commercial interest as they combine high strength and ductility with low material costs [1]. The mechanical properties are mostly related to the TRIP (Transformation Induced Plasticity) effect, which arises due to a presence of reverted austenite in the microstructure. Improving material properties requires a deep understanding of the underlying phase transformation and deformation mechanisms. In a binary martensitic Fe-9wt%Mn alloy with very low carbon content (75 wt. ppm) we observe a serrated appearance of the stress-strain curve at 450°C as well as a discontinuous yielding after tempering at 450 °C for 6 hours. These phenomena have so far mainly been observed in the Fe-C system, where they are referred to as dynamic and static strain ageing, respectively.

Here we investigate this effect using tensile tests, coupled to correlative transmission electron microscopy (TEM) and atom probe tomography (APT) characterization [2–4], performed exactly at the same location to gather direct evidence for the interaction of solute atoms with dislocations.

Fig. 1 depicts such a correlative TEM/APT analysis performed on the material that had been 50% cold-rolled and tempered at 450 °C for 6 hours. Two grain boundaries and a single dislocation line, highlighted by blue arrows, are visible in the TEM image through Bragg contrast and in the 3D atom map in the form of Mn-enriched regions. Not all dislocations visible in the STEM micrograph cause segregation that is sufficiently high to be detectable by APT (red arrow 1) and vice versa (red arrow 2). Calculation of the interaction energy between a Mn atom and both, an edge dislocation and a screw dislocation reveal that Mn has a strong tendency to segregate to edge dislocations. Atom probe crystallography methods confirmed that all the observed dislocation lines have edge character [5].

Strong segregation in conjunction with pronounced local elastic distortions may promote phase transformation [6]. The level of segregation on some dislocations in the tempered Fe-9wt%Mn alloy reaches 25 at% Mn, which is the equilibrium concentration of Mn in austenite at this tempering temperature [7]. TEM analysis, performed on a thin foil, provides direct evidence for the presence of a new structural state localized at an edge dislocation in a dark field view in Fig. 2.

If a new structural state with a 1-2 nm diameter is formed, its growth would be expected during longer tempering times. However, when the sample was tempered for 336 hours at 450°C and analysed, neither growth of the segregation zone nor changes in concentration were observed. This result indicates that in this special case of heterogeneous nucleation at dislocations the critical radius for a viable austenite nucleus is not yet reached.

The observed formation and confinement of austenite is determined by the dislocation stress field. Without dislocations, small size austenite nuclei are thermodynamically unfavourable due to the endothermic interface energy between austenite and the surrounding martensite. However, in the vicinity of the dislocation core, the volume change that is associated with the transformation of martensite into austenite partly compensates the strain energy induced by the dislocation and renders the transformation energetically more favourable. This effect is stronger

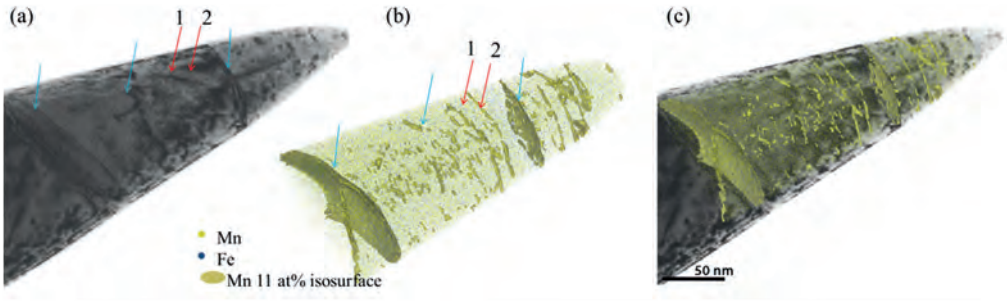

Fig. 1: *Fe-9wt%Mn, 50% cold-rolled and tempered at 450 °C for 6 hours to promote Mn segregation; (a) TEM image; (b) Atom probe tomography results; (c) Overlay of both, TEM and APT; Iso-concentration surfaces indicate areas with Mn concentrations above 11 at%. The blue arrows mark grain boundaries and dislocation lines that are visible in both, the TEM micrograph and the atom probe tomography map.*

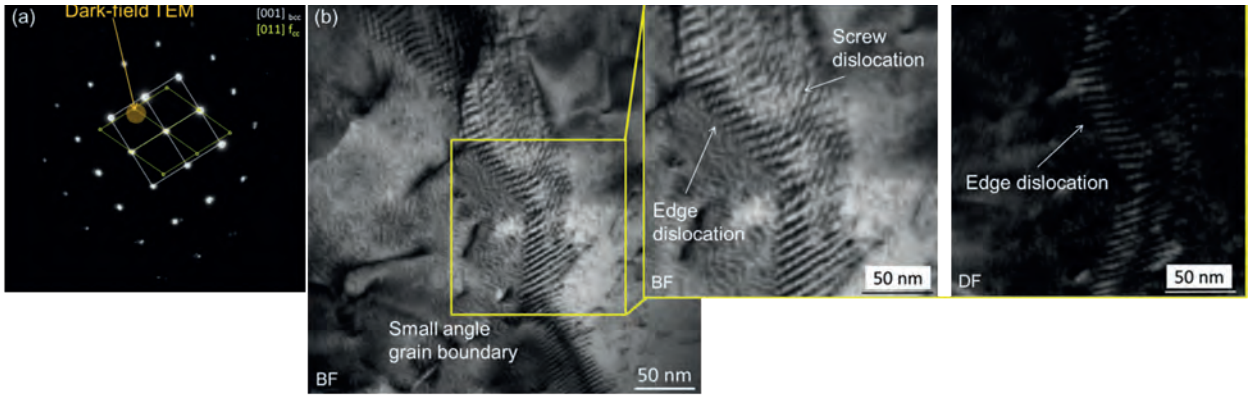

Fig. 2: *(a) Selected area diffraction pattern (SADP) from the enlarged region shown in Fig. 2(b), the diffraction pattern is indexed as $[001]_{bcc}$, the positions of the fcc diffraction spots for a N-W orientation relationship are drawn into the image. (b) Bright-field and dark-field TEM micrographs of a small angle grain boundary, the dark-field micrograph was taken from the region marked by the dark-yellow circle in Fig. 2(a).*

at small diameters and gradually decreases as the diameter increases. As a result, the local transformation is favourable at small diameters but its growth is arrested at some equilibrium diameter (Fig. 3).

A direct simulation of this phenomenon is computationally difficult due to the wide range of the length-scales (long-range dislocation stress field, short range solute-solute interaction) and time-scales

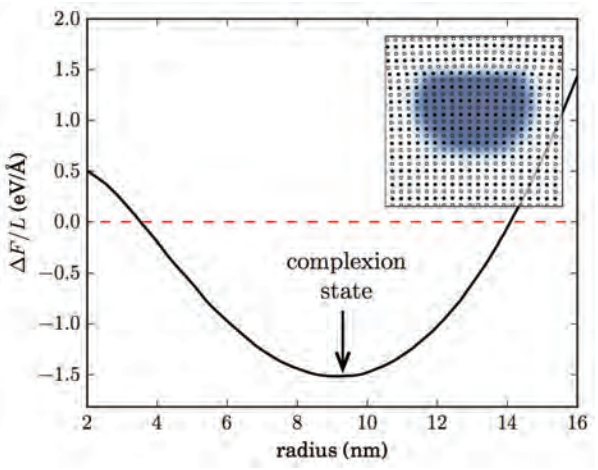

Fig. 3: *The Free energy change per unit ΔF/L of a cylindrical complexion with radius r around an edge dislocation. The examples shown here are for a NiH system at 300K and a bulk hydrogen concentration of 60ppm.*

(diffusion) involved. To address this, we have developed a multiscale modelling approach that couples an analytic model with atomistic calculations to eliminate arbitrary fitting parameters [8]. This approach has been successfully applied to predict and quantify the phase space where dislocation stabilized hydride complexions formed in the Ni-H system (e.g. Fig. 3). The formalism will be extended in a next step to the Fe-Mn system discussed here.

Such a confined structural and chemical state is phenomenologically similar to the term complexion used in the literature [9–11]. Up to now the term complexion has been used only for planar defects such as grain boundaries, where the driving force for complexion formation lies in the reduction of the interface energy. Using *ab initio* simulations, we have shown that these phenomena are also present at dislocation cores surrounded by a ferrite-austenite interface in Fe-based materials [12]. We thus extend this term to the linear case, which is driven by the high dislocation line energy reduction associated with the segregation and a subsequent formation of distinct confined structural states [13].

We have demonstrated for the first time the formation of linear complexions along dislocation lines in a model Fe-9wt% Mn steel. These observations extend the method of segregation engineering via complexions to the linear case, opening up new opportunities to control the microstructure on a nanoscale level.

References

1. Raabe D., Dmitrieva O., Sander B., Ponge D.: Scr Mater (2009) 60, 1141.
2. Herbig M., Raabe D., Li Y.J., Choi P., Zaefferer S., Goto S.: Phys Rev Lett (2014) 112,126103.
3. Toji Y., Matsuda H., Herbig M., Choi P.-P., Raabe D.: Acta Mater (2014) 65, 215.
4. Felfer P.J., Alam T., Ringer S.P., Cairney J.M.: Microsc Res Tech (2012) 75, 484.
5. Kuzmina M., Herbig M., Ponge D., Sandlöbes S., Gault B., Raabe D.: Acta Mater: *under preparation*
6. Raabe D., Sandlöbes S., Millán J., Ponge D., Assadi H., Herbig M., Choi P.-P.: Acta Mater (2013) 61,6132.
7. Dmitrieva O., Inden G., Millán J., Choi P., Sietsma J., Raabe D., Ponge D.: Acta Mater (2011) 59, 364.
8. Leyson G.P., Grabowski B., Neugebauer J.: Acta Mater (2015) 89, 50.
9. Cantwell P.R., Tang M., Dillon S.J., Luo J., Rohrer G.S., Harmer M.P.: Acta Mater (2014) 62, 1.
10. Dillon S.J., Tang M., Carter W.C., Harmer M.P.: Acta Mater (2007) 55, 6208.
11. Baram M., Chatain D., Kaplan W.D.: Science (2011) 332, 206.
12. Zhang X., Hickel T., Rogal J., Fähler S., Drautz R., Neugebauer J.: Acta Materialia (2015) 99, 281.
13. Kuzmina M., Herbig M., Ponge D., Sandlöbes S., Raabe D.: Science (2015) 349, 1080.

Deformation-Induced Martensite in Severely Cold-Drawn Pearlitic Steel: A New Mechanism at Play

S. Djaziri [1], Y.J. Li [2], A. Nematollahi [3], C. Kirchlechner [1], B. Grabowski [3], S. Goto [4], J. Neugebauer [3], D. Raabe [2], G. Dehm [1]

[1]Department of Structure and Nano-/ Micromechanics of Materials (SN)
[2]Department of Microstructure Physics and Alloy Design (MA)
[3]Department of Computational Materials Design (CM)
[4]Department of Materials Science and Engineering, Faculty of Engineering and Resource Science, Akita University, Japan

Cold-drawn pearlitic steel wires exhibit ultra-high tensile strengths of up to 7 GPa [1] being thereby the world's strongest bulk materials, used for a wide range of applications such as suspension bridge cables, springs and tire cords. The high strength of cold-drawn pearlitic steel wires has been associated with the refinement of the originally lamellar eutectoid iron-cementite structure of the pearlite during the wire drawing process, but also with other relevant mechanisms including cementite dissolution and the formation of nanoscale dislocation substructures [2-4]. Upon heavy cold drawing the carbon atoms are released from the dissolving cementite [1,2] and are mechanically alloyed into ferrite. The carbon concentration in the ferrite phase dramatically exceeds the equilibrium solubility limit. In this work, we show that carbon inside the ferrite grain interiors causes a lattice distortion indicating a deformation-driven phase transformation from BCC ferrite to BCT martensite. A new theory based on *ab initio* calculations confirms that such a structural transition takes place by Zener ordering.

Using atom probe tomography (APT) the accurate quantitative carbon concentration in solid solution was analysed at various drawing strains ε. Synchrotron X-ray diffraction was applied to characterize the evolution of lattice parameters, texture and strain in the ferrite phase with respect to the evolution of the carbon concentration. In parallel, we conducted density functional theory (DFT) calculations to elucidate the physical origin of the drawing strain effect on the structural transition of the ferrite phase.

Fig. 1a shows the measured carbon concentration versus the drawing strain for both nominal compositions studied. We find out that the drawing process induced a significant increase in the carbon content inside the originally near-carbon-free ferritic lattice until a steady state is reached at ε ≥ 4. The corresponding evolution of the lattice parameters of the initial ferrite phase with increasing drawing strain is shown in Fig. 1b.

Clearly, the initial bcc lattice of the ferrite unit cell becomes tetragonal distorted with increasing drawing strain (ε ≥ 2). The distortion increases with increasing drawing strain as shown in Fig. 1b. This observation holds true for both, initially eutectoid and hypereutectoid compositions. Fig. 1b reveals three

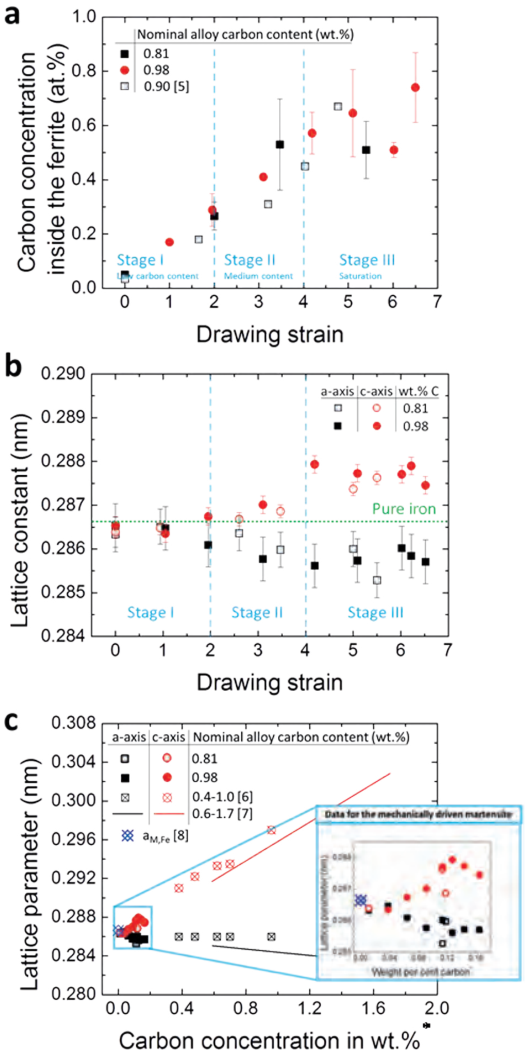

Fig. 1: *(a) Carbon concentration inside the ferrite grain interiors for pearlite wires with different nominal alloy carbon concentration. Literature data [5] for hypereutectoid (0.90 wt.% C) pearlitic steel are used for comparison. (b) Lattice parameters along a-axis and c-axis of α-ferrite lattice during the drawing process. The green line corresponds to pure iron. Blue lines highlight the different stages of structure evolution. (c) Lattice parameters a and c of conventional as-quenched martensite with different nominal (i.e. global) alloy carbon content (cross symbols and solid lines) taken from the literature [6] and [7], plotted together with our data (open and filled symbols, a zoom of them is shown in the inset). aM,Fe refers to the lattice parameter of martensite in carbon-free iron [8]. The asterisk * in the abscissa axis is added to underline the difference between the carbon content of the present study measured by APT in the ferrite grain interiors and those taken from literature referring to the nominal carbon content.*

stages in the evolution of the lattice parameter with drawing strain. In stage I ($\varepsilon < 2$), the ferrite unit cell has a bcc crystal structure where the lattice parameter remains unchanged and is equal to that of pure iron. In stage II ($2 \leq \varepsilon \leq 4$), the lattice parameter splits into two values corresponding to a tetragonal structure with two different axes a and c. Up to $\varepsilon = 4$, the a-axis shrinks by ~ 0.36% while the c-axis is expanding by ~ 0.45%. In stage III ($\varepsilon > 4$), the lattice parameter values a and c remain constant within the experimental error. Hence, the unit cell of the ferrite transforms from the bcc structure into the body centred tetragonal (bct) structure.

The change of the carbon concentration that is solved inside the ferrite grains during the drawing process is closely related to the tetragonal distortion of the ferrite unit cell. Indeed, the bct structure of ferrite is stabilized in the third stage ($\varepsilon > 4$) which may be coupled to the saturation of the solute carbon concentration in the ferrite. We note also that the c/a ratio reaches a steady state in the third stage where c/a = 1.007 ± 0.002. This is an unexpected observation since the tetragonal distortion of the ferrite due to solute carbon is usually known from as-quenched Fe-C martensite with high carbon concentration. Hence, the fundamental question arises whether severe plastic deformation can produce the same type of distorted phase, i.e. a deformation-driven Fe-C martensite.

Fig. 1c shows the lattice parameters of martensite from the different studies compared with our current data. Surprisingly, the measured lattice parameters for our current material fit well with lattice parameters of martensite determined by Kurdjumov et al. [6]. An even better agreement is obtained with an extrapolation of the data of Roberts [7]. Our data extend the as-quenched martensite data reported in [6] and [7] to lower C contents indicating that wire drawing induces a martensite-like tetragonal distortion of the initial bcc Fe phase. These observations exhibit a clear signature of the ordering of carbon atoms on the octahedral interstitial sites causing the ferrite unit cell to be distorted.

The thermodynamics behind the order-disorder transformation of the Fe-C system has been formulated long ago by Khachaturyan et al. [9] using microscopic elasticity theory. This theory, when coupled with DFT [10], provides a reasonable agreement with the experimental order-disorder transition of a 'usual' as-quenched Fe-C martensite. However, the mechanically driven bcc-bct transition observed in this work cannot be explained by this previous theory. Therefore, in this work, a new model has been developed that captures the strain induced interaction of C with the host matrix and which can be extended to wire drawing conditions. The new model provides not only an excellent agreement with experimental observation for the as-quenched martensite (red line and square in Fig. 2), but captures also the effect of the applied strain — exerted by the wire drawing process — within a renormalized C formation energy. As shown in Fig. 2 by the blue line, by considering 0.4 % uni-axial strain along [100], our new theory can explain the unusual tetragonal distortion measured in the present work for the low C concentrations (blue filled circles in Fig. 2).

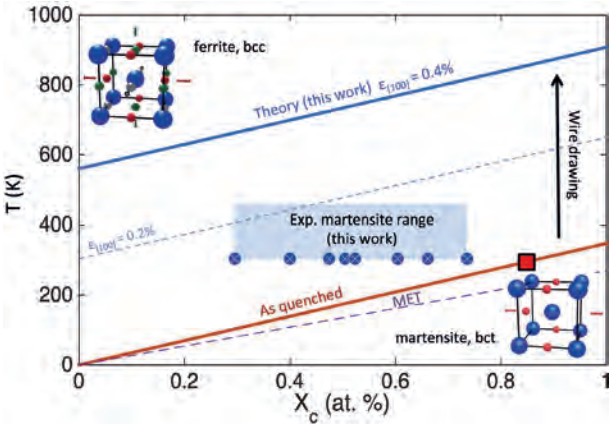

Fig. 2: *Predicted equilibrium phase diagram of Fe-C solid solutions calculated by means of DFT calculations. The order-disorder transformation temperatures are plotted as a function of carbon concentrations for the systems under an applied elastic strain of 0.4% (blue line) and also in the absence of any strain (red line). The red square corresponds to the only available experimental data point for an as-quenched martensitic transformation. The blue dots represent C concentrations of the tetragonally distorted martensite measured in this work. The dashed line represents the order-disorder transformation predicted by means of microscopy elasticity theory in Ref. [10].*

References

1. Li, Y.J.; Raabe, D.; Herbig, M., Choi, P.; Goto, S.; Kostka, A.; Yarita, H.; Borchers, C.; Kirchheim, R.: Phys. Rev. Lett. 113 (2014) 106104.
2. Li, Y.J.; Choi, P.; Borchers, C.; Westerkamp, S. ; Goto, S. ; Raabe, D. ; Kirchheim, R.: Acta Mater. 59 (2011) 3965.
3. Herbig, M.; Raabe, D.; Li, Y.J.; Choi, P.-P.; Zaefferer, S.; Goto, S.: Phys. Rev. Lett. 112 (2014) 126103.
4. Li, Y.J.; Kostka, A.; Choi, P.; Goto, S.; Ponge, D.; Kirchheim, R.; Raabe, D.: Acta Mater. 84 (2015) 110.
5. Maruyama, N.; Tarui, T.; Tashiro, H.: Scr. Mater. 46 (2002) 599.
6. Kurdjumov, G.V.; Khachaturyan, A.G.: Acta Metall. 23 (1975) 1077.
7. Roberts, C. S. : Trans. AIME 197 (1953) 203.
8. Lee, S.J.; Lee, S.; De Cooman, B.C.; Scr. Mater. 64 (2011) 649.
9. Khachaturyan A.G.; Shatalov G.A.; Acta Metall. Mater. 23 (1975) 1089.
10. Udyansky, A., von Pezold, J.; Dick, A.; Neugebauer, J.: Phys. Rev. B 83 (2011) 184112.

Investigation of Hydrogen Trapping, Activity and Exposure Time on Embrittlement of High Strength Steels under Load

W. Krieger [1], S. Merzlikin [1], E. McEniry [2], T. Hickel [2], H. Springer [3], M.Rohwerder [1]

[1]Department of Interface Chemistry and Surface Engineering (GO)
[2]Department of Computational Materials Design (CM)
[3]Department of Microstructure Physics and Alloy Design (MA)

Most advanced steel grades have strengths in the gigapascal range. At these strength levels, the susceptibility to hydrogen embrittlement (HE) is particularly acute. The main sources of hydrogen in steel components are the finishing or reconditioning steps used to clean or apply protective coatings, welding or annealing in hydrogen-bearing atmospheres. Another less obvious and controllable (but certainly over the life-time very important) mechanism responsible for H-uptake is atmospheric corrosion or galvanic coupling during service.

For assessment of HE usually short testing is performed by adjusting different levels of hydrogen and then performing a relatively fast mechanical test. Moreover, such tests are usually performed on some specific high alloyed steel of practical interest, while methodologically relevant screenings of a wide spectrum of materials are missing. For these selected materials, the risk of failure is typically correlated with the amount of diffusible hydrogen only. It remains an open question whether much smaller hydrogen activities, but over more extended times and with an application of permanent strain or stress, can add up to similar failure risks. Hence, the fundamental dependence of HE on the parameters time, hydrogen activity and load is not yet sufficiently investigated.

For a fundamental understanding of these parameters we follow a two-fold strategy. For the experimental approach a specially designed *in situ* setup is build. It allows us to charge the sample with hydrogen during a creep or tensile test. In parallel, *ab initio* and larger-scale tight binding calculations are performed to simulate the trapping mechanisms and kinetic processes. Systematic investigations of the above mentioned experimental parameters and their theoretical counterparts will provide a HE matrix (in particular for long times and low-H activities) and a correlation of embrittlement mechanisms with H-trap sites. We invested into design and production of *in situ* cells for long term (up to months) creep experiments, which allow us to test the matrix parameters in a methodical and statistical way.

To avoid a narrow focus on specific steel grades, we concentrate in theory and experiment on a model alloy system with a chemical composition and microstructure features that represent ferritic steels in general and give us a possibility to cover a wide range of grain sizes, dislocation densities and other H trap sites. For these purposes Fe-5%Ni model alloy is prepared in the MA. To characterize the degradation of the material creep, tensile tests and scanning electron microscopy (SEM) are used. Additionally, the trap structure before and after the *in situ* mechanical testing is analyzed with a thermal desorption spectroscopy (TDS) using a novel ultra high vacuum-based TDA-MS (thermal desorption mass spectroscopy) setup designed in the GO [1]. For a lateral resolution of H-trapping a wide spectrum of H-sensitive analytical techniques available at the GO will be used. In parallel, TDS is addressed with kinetic Monte-Carlo simulations based on the atomistic parameters determined in the CM. The challenges of the approach make this project an interdisciplinary one, where the expertise of different departments is combined to achieve an ambitious goal.

To get first experimental insights, we focus on two very different conditions of the Fe-5%Ni alloys – annealed (A) and cold rolled (CR). The samples are H-charged at different potentials *in situ* in a cell containing 0,1M NaOH while a load of 0,95 RM is

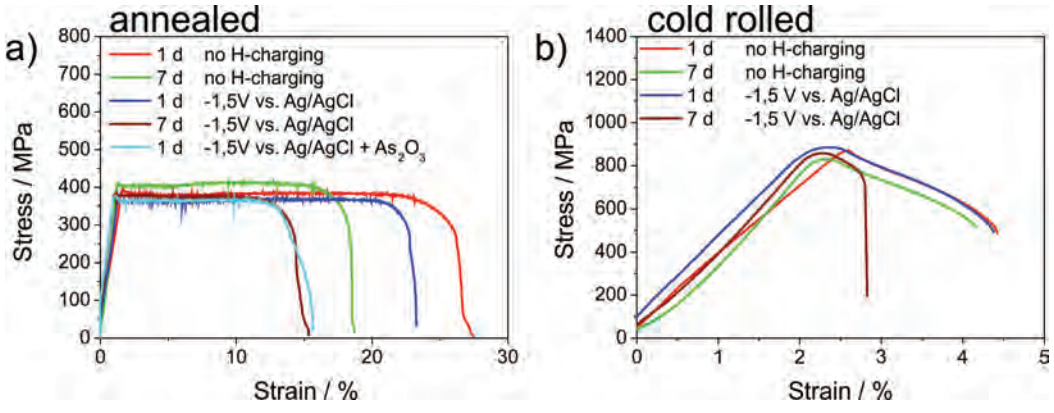

Fig. 1: *Tensile test curves for a) annealed A and b) cold rolled CR model alloy.*

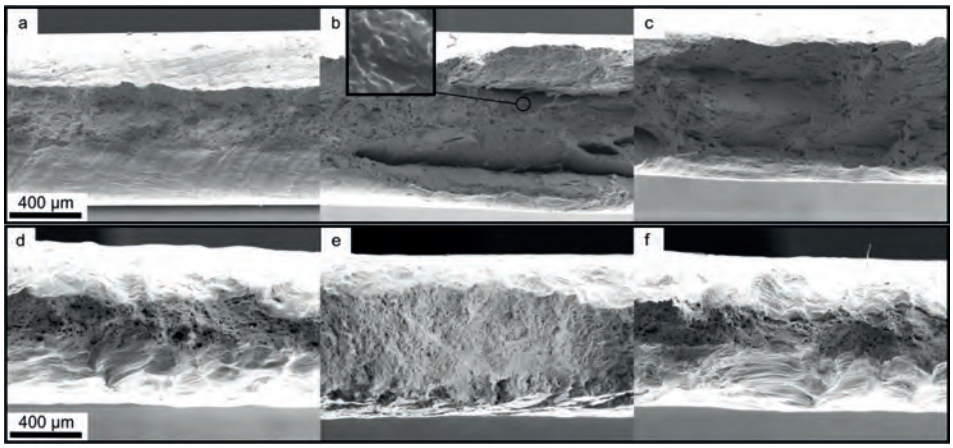

Fig. 2: *a,b,c) CR; d,e,f) A-sample. a,d) no H-charging; b,e) 24h charging + As_2O_3 and c,f) 7d charging.*

applied. During further experiments, the parameters load; potential, H-activity and time are varied to get a HE-matrix for each material state. After the creep test with varying exposure times, the sample is pulled in a tensile machine at a rate of 10^{-4} s^{-1} until fracture to get a stress-strain curve and to analyze the fracture surface. Pieces of a sample gauge length are cut and analyzed with TDS before and after the creep test.

The HE occurs in both cases after 24h during HE reference tests (with recombination inhibitor) (Fig. 1). As expected, the most drastic effect is seen in the case of CR samples, which failed completely during *in situ* creep. At the fracture surface (Fig. 2) cracks and blisters are seen in the bulk of the specimens parallel to the surface. Charging without inhibitor leads to only slight reduction in fracture deformation in A-samples after 24h, but after 7 days the degradation is clearly visible. TD- analysis of as-received A-samples showed no H-desorption peaks, for CR material 2 peaks with H-desorption activation energy of approx. 29 and 38 kJ/mol have been found (Fig. 3). After the creep under H-charging for 24h one H-desorption peak (29kJ/mol) was found also for A-material, thus this peak corresponds to hydrogen trapped at dislocations. The second peak is due to the hydrogen trapped in micro voids at inclusion-matrix interfaces inside CR material.

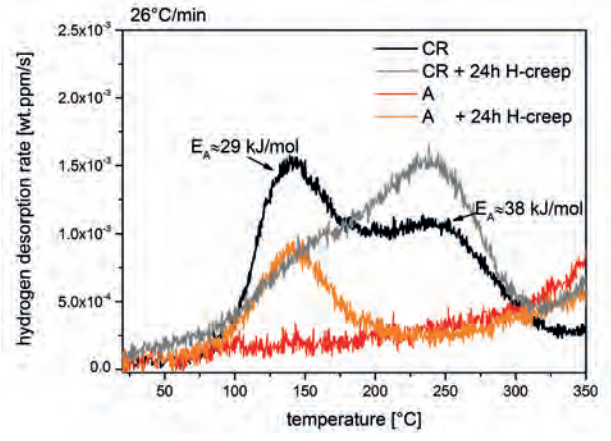

Fig. 3: *TD-spectra of A and CR model alloy before and after 24h in situ creep.*

The trapping behaviour of the most important microstructure features considered in experiment, namely grain boundaries, phase boundaries and dislocations, has been analyzed theoretically. The tendency of hydrogen to become trapped by grain boundaries in ferrite depends very sensitively on the local geometry. Parameters such as the grain boundary energy and the angle of misorientation do not appear to correlate well with the affinity of hydrogen to the boundary. However, we have found that a class of [110]-terminated twist grain boundaries is particularly attractive for hydrogen, due to substantial interstitial voids which are over-coordinated in comparison to bulk ferrite. The ferrite-cementite phase boundary is another efficient trapping site for hydrogen. The reasonably low diffusion barrier from the ferrite into the boundary layer further supports the trapping, while diffusion into or within cementite is characterized by very high barriers. The results of these simulations, such as the H-trapping energies and diffusivities in the vicinity of such features, as well as the density of H-traps within the microstructure, are used as input parameters for scale-bridging models of H-diffusion (such as kinetic Monte Carlo) currently performed in collaboration with colleagues at the Interdisciplinary Centre for Advanced Materials Simulation at the Ruhr-Universität Bochum, in order to simulate and interpret the experimentally determined TD-spectra.

The next steps will be to proceed with the experimental HE matrix. Precipitates will be introduced as further trap sites to the material. Ti and Cr carbides will be considered in experiments as well as in simulations. In order to directly link the hydrogen activity to simulations, permeation experiments [2] will be carried out, a gauge length of the tensile samples will be analyzed before and after *in situ* creeping, using techniques able to give a laterally resolved insight into a qualitative description of the H-trapping sites.

References

1. Merzlikin, SV.; Borodin, S.; Vogel, D.; Rohwerder, M.: Talanta 136 (2015) 108-113.
2. Grabke, H.J..; Riecke, E.: Mater. Technol. (2000) 34(6) 331.

Towards Self-Healing Metals

B. Grabowski [1], C.C. Tasan [2]

[1]Department of Computational Materials Design (CM)
[2]Department of Microstructure Physics and Alloy Design (MA)

The field of self-healing materials is dominated by polymers (Fig. 1) since chemical reactions in polymers are very efficient in producing a significant energy release compared to the typical bonding strength. In contrast, in ceramics and metals, diffusional processes that are needed to transport the self-healing agents to the damaged sites are slow at ambient temperatures. Despite this challenge there is an increasing interest to design self-healing metals (see black curve in the inset of Fig. 1) due to the potential economical impact. Dr. C. Tasan and Dr. B. Grabowski were recently awarded a grant within the DFG Priority Programme SPP1568 for their innovative idea of employing nano-shape memory alloy (SMA)-dispersoids as self-healing agents in metals. The joint experimental-theoretical work has recently been cumulated in a review article on self-healing metals [1].

The presently available/proposed concepts can be subdivided into two categories [1]: self-healing on the nano length scale and self-healing on the macro length scale (Fig. 2). The newly proposed concept of Tasan and Grabowski ("nanoSMA-dispersoids") falls into the first category. The aim of the concepts from the first category is to heal damage on the nanometer length scale, i.e., nano-cracks. The high-T precipitation concept (Fig. 2a) requires a microstructure with a supersaturated amount of solute atoms which exhibits precipitation in regions where nano-voids are present. The low-T precipitation concept (Fig. 2b) is closely related, but solute atoms need to segregate to dislocation cores. When localization leads to stress concentration and formation of nano-voids, the mobile solute atoms are attracted and diffuse through the dislocations towards the stress region. Precipitation within the nano-voids eventually leads to void closure and healing of the damaged region.

The second category of self-healing approaches in metals aims at healing macro-cracks. The SMA-clamp&melt concept (Fig. 2d) requires a composite microstructure with SMA reinforcement wires embedded in a solder matrix material. Under stress a crack is produced in the solder material, which triggers a transformation in the SMA phase. Self-healing is achieved by heating which leads to a contraction of the sample. Upon further heating the cracked surfaces melt and rejoin. The solder tubes/capsules concept (Fig. 2e) emulates the original self-healing concept employed in polymers: a solder material is encapsulated inside of ceramic capsules inside a host matrix of a higher melting point and ultimate tensile strength material. The solder is activated only, once a crack in the host matrix has formed, by increasing the temperature above the melting temperature of the solder. The solder then wets the crack surfaces, fills the crack, and solidifies closing the crack thereby. The coating agent concept (Fig. 2f) is a very similar approach, with the main difference being the utilization of a coating for the self-healing. The electro-healing (Fig. 2g) is achieved by immers-

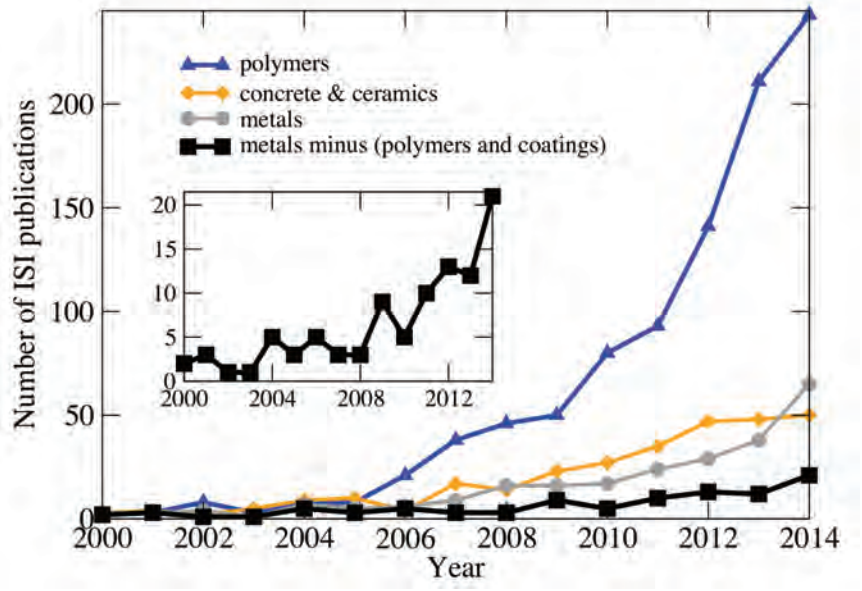

Fig. 1: *Publication numbers from ISI Web of Knowledge for the last 14 years in the field of self-healing polymers, concrete & ceramics, and metals. The inset shows a zoom-in for the black curve.*

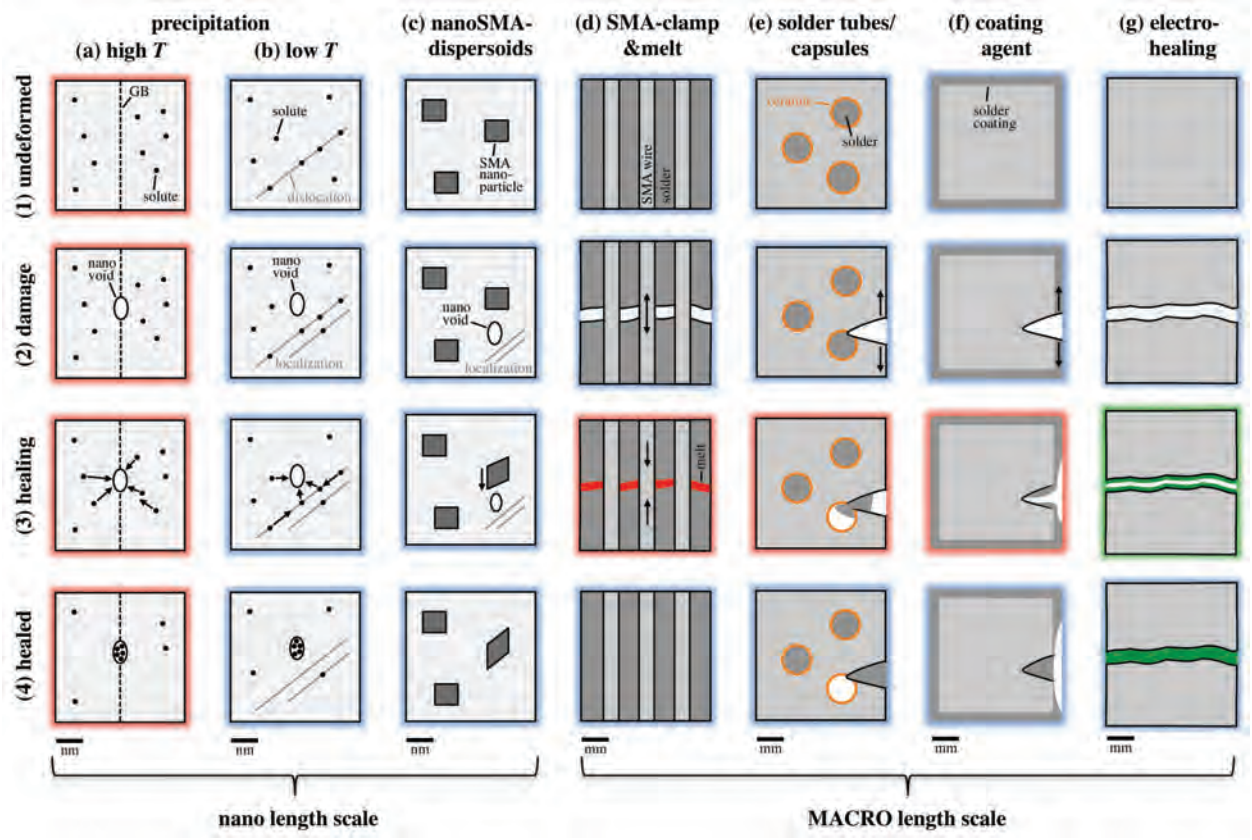

Fig. 2: *Schematic overview of the proposed/investigated self-healing concepts in metals. See main text for details.*

ing a damaged sample into an electrolyte solution and applying a voltage. The following electrochemical reaction leads to deposition of material inside the crack eventually closing it.

The nanoSMA-dispersoid concept (Fig. 2c) proposed and investigated by Tasan and Grabowski is motivated by recent atomistic simulations which clearly reveal that a stress-driven grain boundary was able to heal an approaching nano-crack. The main idea is to encapsulate the shape memory effect in nano-dispersive coherent particles which shall act as self-healing agents providing autonomous self-healing of metals. The coherent shape memory nano-particles will be introduced into and stabilized by a standard solid solution metallic matrix. The coherent host matrix will exhibit standard mechanical properties such as strength, ductility, and fracture toughness. The special and novel self-healing properties will arise by optimizing the size and distribution of the shape-memory nano-particles such as to guarantee an optimum long-term resistance to nano-cracks which - in normal circumstances -would trigger the onset of fracture. For the present purposes, nano-cracks and their stress/strain fields will act as local stress sources activating the transformation of the nanoparticles and thereby the self-healing process.

The highly challenging nature of the proposed goals calls for an integrated approach combining state of the art finite temperature *ab initio* simulations and *in situ* multiscale experimental characterization techniques in conjunction with long standing alloy design knowhow. Current focus is on a specific material system, Ti-Ni-V, with Ti-Ni as the shape memory alloy for the nano-particles. The mechanisms shall be investigated for this model system, however, the developed methodology and knowledge will apply to other materials given similar transformation properties.

References

1. B. Grabowski and C.C. Tasan: Review article on “Self-healing metals” in Advances in Polymer Science (2015) *in press*.

Investigations on the Local Bonding Strengths and Bonding Mechanism of Aluminium-Steel Joints Produced by Cold Forging

A. Altin [1], S. Wohletz [2], W. Krieger [1], A. Kostka [4], P. Groche [2], H. Springer [3], A. Erbe [1]

[1]Department of Interface Chemistry and Surface Engineering (GO)
[2]TU Darmstadt, Institute for Production Engineering and Forming Machines, Darmstadt, Germany
[3]Department of Microstructure Physics and Alloy Design (MA)
[4]Department of Structure and Nano-/Micromechanics of Materials (SN), now at: Ruhr-Universität Bochum, Faculty of Mechanical Engineering

Cold forging is a promising method to achieve dissimilar joining to facilitate the design of novel materials combinations. Combining materials with different physical and mechanical properties allows a large variety of applications in the manufacturing industry. For light weight construction, in particular the combination of steel and aluminium, has a significant importance, especially in automotive and aeronautics industries. Established fusion welding processes, where one or both of the materials are molten, typically lead to the often uncontrolled and rapid formation of Fe/Al intermetallic phases. Brittleness of extended Fe/Al phases results in weak bonds and poor weld quality [1, 2]. Therefore, cold welding by plastic deformation, e.g. cold forging, is an attractive manufacturing technology for future applications, with the potential to minimise or control the formation of intermetallic phases in the interfacial region [3].

Nevertheless, the mechanism of the bond formation in cold welding remains largely unexplored. According to the macroscopic model of Bay [4], breaking of cover layers, e.g. metal oxides, occurs after exceeding a critical formability. Juvenile metal extrudes between these cracks, which results in an adhesive joint formation. This macroscopic model does not consider details on an atomic scale around the interface between the partners. In addition, bond strength of joints depends on welding conditions, such as temperature, surface conditions and surface enlargement [5]. To control the formation of intermetallics, and to maximise adhesion, a more quantitative understanding of processes on an atomic scale is required.

One topic of recent investigations was to elucidate the role of primary heat treatment on the bond strength in cold forging of AA6082 aluminium alloy and C15 steel. A cross section of the resulting geometry is shown in Fig. 1. Steel itself is difficult to cold-weld, amongst other reasons because of its hardness [6]. Hardness can be modified by “soft annealing”, resulting in an alignment of the hardness of steel to the value of AA6082. This heat treatment results in the reduction of flow stress in the steel which means that soft annealed steel shows stronger bonds. According to finite element method (FEM) simulations of the cold forging process considering effects of the surface enlargement and normalized contact normal stress, the strongest bonds are expected in region (II) (Fig.1). The consequence is a stronger global bond of the joint. For determining the local bond strength, tensile specimens were cut by spark erosion from areas of interest along the joint interface (Fig. 1). A summary is shown of the resulting tensile strength of two different heating states of the C15 steel, soft annealed for 1 h (“sa”), and for 5 h (spheroidized, “s”) [6, 7].

Because of the small extrusion at position (III), this region is not contributing to the overall bond. Hence, the preparation of tensile specimens was not feasible as samples already disintegrated during the preparation. Experimental results show a weak bond in region (I), and the expected strongest bond in region (II). The softening of the C15 steel resulted in an increase of the bond strengths in regions (I) and (II). The resulting fracture after the tensile test can be divided into three major zones. In the first zone, ductile failure

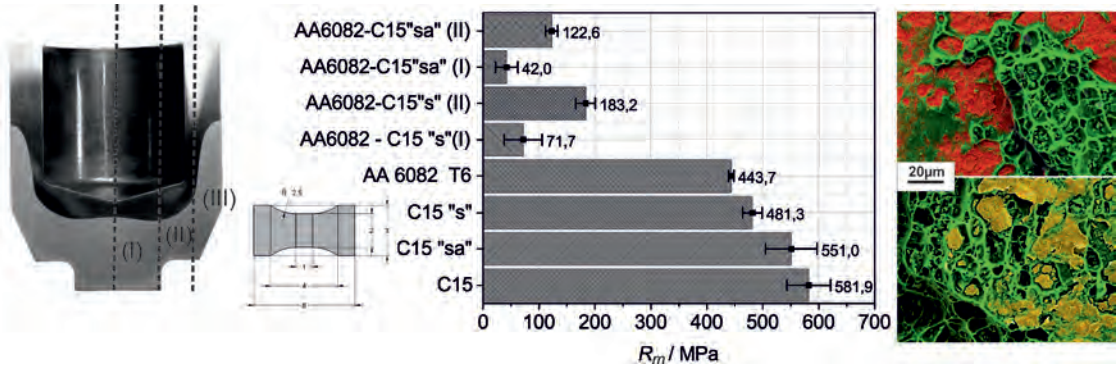

Fig. 1: *Tensile strengths of welds at different positions as indicated in the cross section through the weld geometry on the left, compared to the base materials. Right: EDX elemental maps showing Al (green) and Fe (red) of the fracture after tensile test (top=steel side, bottom=Al side).*

of the aluminium is clearly visible. In this zone, the bond between steel and aluminium is stronger than the base material. In the second zone, the aluminium parts remaining adhered to the steel side indicate brittle failure. Finally, in the third zone, brittle failure of iron is observed, whose residues remain on the aluminium side. All three zones are contributing to the bond between steel and aluminium. The resulting tensile strength of the welds is an average with different contributions [6, 7]. One particular issue which is yet unexplored is the presence of residual stresses in the resulting workpieces.

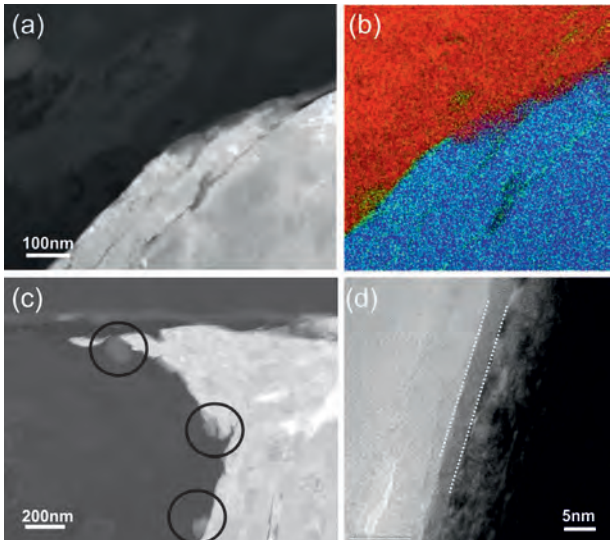

Fig. 2: *C15 steel and AA6082 welds. (a) STEM image along interface. (b) Corresponding EDX elemental map (Al – red, O – green, Fe – blue). (c) STEM image with intermetallics highlighted by black circles. (d) High resolution TEM showing a few nm thick reaction layer highlighted with white dashed lines.*

For in depth analysis of the interface after bond formation, transmission electron microscopy (TEM) was performed. A lamella for TEM experiments was extracted from region (II) via focused ion beam cutting along interface (Fig. 2). At first glance, no indication of the presence of continuous intermetallic phases is found, different from the situation during welding at high temperatures [1, 2]. However, at few spots, apparently randomly distributed along the steel/aluminium interface, intermetallics are observed (Fig. 2c). The nucleation of intermetallics may be the result of a locally increased temperature, induced by friction during plastic deformation of both partners. Whether the isolated intermetallic particles found here actually facilitate bond formation by helping to decrease interface energy and interface strain, or whether they decrease the finally observed tensile strength because they are intrinsically brittle, remains to be investigated. Crucial for the bond formation is most likely the detection of a few nm "reaction layer" along the entire interface (Fig. 2d), which consists of Fe and Al. This layer may reduce lattice strain at the interface, and its formation is most likely the key for the formation of a metallic bond between the two pieces. Further investigations are ongoing to obtain detailed information about the chemical composition and crystallography of this reaction layer.

A factor which is supposed to hinder the formation of metallic bonds is the presence of oxides at the interface [7]. In the energy-dispersive x-ray spectroscopy (EDX) elemental maps (Fig. 2b), the presence of oxygen in the interface region is obvious. Further, oxide-rich regions are found 10s of nm away from the interface. An important oxide source is the presence of oxide on the materials prior to welding. These oxides remain inside the final joint. The chemical or electrochemical removal of oxides is a promising line to increase the bond strength at the interface.

Summarising, soft annealing of steel increases the macroscopic bond strength in dissimlar welding steel and aluminium by cold forging. A maximum tensile strength of 183 MPa has been obtained for 5 h annealing (spheroidizing), still significantly below the corresponding values of the base materials. Investigations at the nanoscale showed the presence of a few nm thick reaction layer consisting of Fe and Al along the entire interface, which may be crucial for bond formation.

This work was conducted in the Priority Programmeme "Joining by Forming" (SPP1640) of the German Research Foundation (DFG).

References

1. Springer, H.; Kostka, A.; Payton, E.; Raabe, D.; Kaysser-Pyzalla, A.; Eggeler, G.: Acta Mater. 59 (2011) 1586.
2. Springer, H.; Kostka, A.; dos Santos, J.; Raabe, D.: Mater. Sci. Eng. A 528 (2011) 4630.
3. Groche, P.; Wohletz, S.; Brenneis, M.; Pabst, C.; Resch, F.: J. Mater. Process. Technol. 214 (2014) 1972.
4. Bay, N. Met. Constr. 18 (1986) 369
5. Zhang, W.; Bay, N.; Wanheim, T. CIRP Ann. 41 (1992) 293.
6. Groche, P.; Wohletz, S.; Erbe, A.; Altin, A.: J. Mater. Process. Technol. 214 (2014) 2040.
7. Altin, A.; Wohletz, S.; Krieger, W.; Kostka, A.; Groche, P.; Erbe A.: Adv. Mater. Res. 966-967 (2014) 445.

Structural Degradation of Fuel Cell and Electrolyzer Catalysts

K. Mayrhofer [1], C. Baldizzone [1], N. Hodnik [1], E. Pizzutilo [1], G. Polymeros [1], C. Scheu [2], K. Hengge[2]

[1]Department of Interface Chemistry and Surface Engineering (GO)
[2]Independent Research Group "Nanoanalytics and Interfaces" (NG)

The ever-improving synthesis techniques have propelled the field of material science towards the design of an increasingly broader variety of catalytic structures, spanning from elaborated support architectures to complex nano-engineered catalytic structures. Nonetheless, with the advances in activity performances the careful consideration of the durability of such structures has too often been overlooked. Paramount for the viability of an electrocatalyst for industrial application is its ability to conserve the initial performances during the operative life of the device. In several energy-conversion applications the conditions found at the electrode are fairly aggressive and often induce a complex interplay of different degradation pathways [1-5]. Thus, the catalyst is bound to undergo a series of morphological and compositional modifications necessarily affecting its electrochemical performances.

To effectively suppress, or at least thwart, the overall performance decay, it is crucial to first identify and understand the individual contributions, which together lead to the structural degradation of the electrode materials. Mirroring the complexity of such (electro-) chemical processes, a thorough investigation of this crucial issue requires the use of a variety of experimental tools [2, 6]. In our electrocatalysis research group (GO), the back-bone of general investigation strategy consists of the coupling of macroscopic electrochemical characterization techniques (e.g. Rotating Disk Electrode, Scanning Flow Cell) and microscopic transmission electron microscopy. Thus, the combination of these two different research backgrounds stemming from the active collaboration of the GO, and the NG is instrumental to understand the correlation between the decay in electrochemical performances and the structural modifications at the nanoscale.

To date, the implementation of this strategy has been proven highly successful in resolving the complex convolution of degradation pathways affecting both state-of-the-art Pt catalysts [1] and advances catalytic systems, e.g. porous nanostructures [2]. Furthermore, the deep fundamental understanding of the processes acting at the nanoscale allowed the development of durability-tailored nanocatalysts, introducing the concept of confined alloying and, de facto, opening the way for new-generation catalytic systems [6].

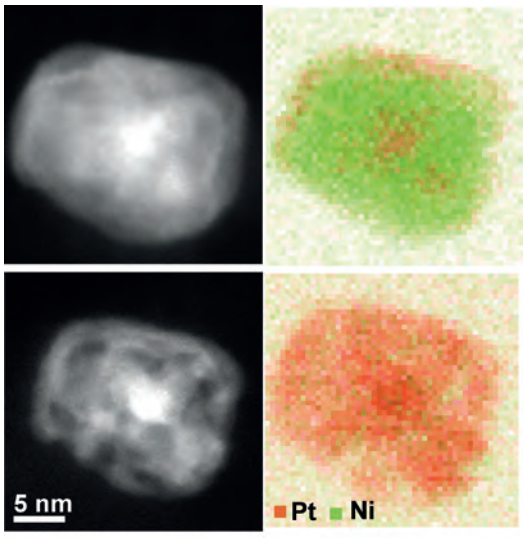

Fig. 1: *Comparison of High Angle Annular Dark Field images (HAADF) and Electron Energy Loss Spectroscopy scans (EELS) before and after electrochemical treatment. The direct observation of the catalyst allows following the compositional and morphological changes happening at the nanoscale.*

References

1. Meier, J. C.; Galeano, C.; Katsounaros, I.; Topalov, A.A.; Kostka, A.; Schuth, F.; Mayrhofer, K.J.J.: ACS Catalysis (2012) 2, (5), 832-843.
2. Baldizzone, C.; Gan, L.; Hodnik, N.; Keeley, G.P.; Kostka, A.; Heggen, M.; Strasser, P.; Mayrhofer, K.J.J.: ACS Catalysis (2015) 5000-5007.
3. Heinzl, C.; Hengge, K. A.; Perchthaler, M.; Hacker, V.; Scheu, C.: Journal of The Electrochemical Society (2015) 162, (3), F280-F290.
4. Schenk, A.; Grimmer, C.; Perchthaler, M.; Weinberger, S.; Pichler, B.; Heinzl, C.; Scheu, C.; Mautner, F.A.; Bitschnau, B.; Hacker, V.: Journal of Power Sources (2014) 266, 313-322.
5. Perchthaler, M.; Ossiander, T.; Juhart, V.; Mitzel, J.; Heinzl, C.; Scheu, C.; Hacker, V.: Journal of Power Sources (2013) 243, 472-480.
6. Baldizzone, C.; Mezzavilla, S.; Carvalho, H.W. P.; Meier, J.C.; Schuppert, A.K.; Heggen, M.; Galeano, C.; Grunwaldt, J.D.; Schuth, F.; Mayrhofer, K.J.J. Angew Chem Int Edit (2014) 53, (51), 14250-14254.